Ph.D. thesis prepared within the Warsaw-4-PhD School in Natural and BioMedical Sciences at the Institute of Physical Chemistry, Polish Academy of Sciences, ul. Kasprzaka 44/52, 01-224, Warsaw, Poland.

Titania-based photocatalysts prepared by sonication in understanding the selective oxidation of lignin-inspired molecules to phenolics

Ph.D. Candidate

Abdul Qayyum

Supervisor

Prof. Dr. hab. Eng. Juan Carlos Colmenares Quintero

Warsaw, November 2023

Dedicated to

Dearest Almighty Allah

&

Dearest Prophet Muhammad (Peace be upon him)

&

my beloved Parents

Acknowledgement

All the praises are credited to the sole creator of the entire universe, almighty ALLAH, the Most Beneficent, the Most Merciful and the Most Compassionate, Who granted me the power of vision and wisdom to unknot the mysteries of the universe in a more systematic manner what people call it SCIENCE. Only by the grace of ALLAH could I make this material contribution to the already existing ocean of knowledge. I invoke Allah's blessings and peace for my beloved Prophet HAZRAT MUHAMMAD (PBUH), who is the eternally present torch of direction and knowledge for humanity as a whole and whose honorable and spiritual teachings enlightened my heart, soul and mind.

I desire to extend my most sincere thanks and a deep sense of obligation to my supervisor, **Prof. Dr. hab. Eng. Juan Carlos Colmenares Quintero** for introducing me to sonochemistry, material science and catalysis, improvisation of scientific reports, and the scientific writing style. I am grateful for his ever-inspiring guidance, keen interest, scholarly comments and constructive suggestions throughout the journey of my doctoral studies. The impression of his kind personality will always remain engraved in my mind. Thank you for always keeping your office's door opened for me and allowing me to discuss any topic and your constructive discussion. Thank you for giving me this opportunity to gain experience and grow more as a scientist and an individual.

I would like to express my sincere gratitude to **Dr. Dimitrios A. Giannakoudakis** for always being ready to help design and discuss experiments, comments, valuable discussions and reviewing the scientific reports, research articles and thesis.

I would like to thank **Dr. Dariusz Łomot** for his guidance and support by his expertise in the laboratory instruments and technical skills, translation of abstract and assistance in preparing the schematic presentation and characterization, such as nitrogen sorption measurement and TPO-TPR measurements.

I thank **Prof. Dr. Ramón Fernando Colmenares-Quintero** from the Engineering Research Institute (In3), Universidad Cooperativa de Colombia, Medellín 50031, Colombia, for supporting my research as an external advisor.

I would also like to acknowledge the support from colleagues of the IPC-PAS, Dr. Dmytro Lisovytskiy for XRD and EDXRF measurements, Ms. Agnieszka Wiśniewska for TGA measurements, Dr. Kostiantyn Nikiforow for XPS measurements. I would like to thank Dr. Alec Lagrow and Dr. Oleksandr Bondarchuk from the International Iberian Nanotechnology

Laboratory, Braga, Portugal, for the transmission microscopy and for the XPS measurements, respectively.

I would like to thank all the current and former colleagues from the research group "Catalysis for Sustainable Energy Production and Environmental Protection" (Dr. Dimitrios Giannakoudakis, Dr. Jovana Prekodravac, Dr. Ayesha Khan, Swaraj Rashmi Pradhan, Dr. Rafael L. Oliveira, Laura Wrońska, Karolina Kawka, Agnieszka Dżugan, Dr. Marta Paszkiewicz-Gawron, Behdokht Hashemi Hosseini, Dr. Nilesh R. Manwar, Dr. Hanggara Sudrajat and Maya Nobatova). I would like to thank Dr. Eng. Wojciech Juszczyk for his support in dealing with the gases for gas chromatography.

I would also like to acknowledge the support of the administrative staff of the IPC-PAS, Warsaw, Poland.

I would like to acknowledge Prof. Dr. Enrique Castellon and Dr Juan Antonio Cecilia from the University of Malaga, Spain, for their kind support and cooperation during my research visit.

I would also like to thank Prof. Dr. Gonzalo Manuel Angulo Nunez and Dr. Eng. Justyna Mech-Piskorz from IPC-PAS, Warsaw, for teaching the photoluminescence techniques and Prof. Dr. Jaroslaw Grzegorz Sadlo from the Institute of Nuclear Chemistry and Technology, Warsaw for Electron paramagnetic resonance technique.

Most importantly, I would like to express my deep love and appreciation to my respectable beloved parents **Mr.** and **Mrs. Mehboob Hussain**. Their prayers, moral support, and love were more than I can express. I sincerely thank my dearest sisters and beloved brothers for the prayers, care and unwavering support. Thank you for always being there for me to lift me up in hard times. I am sincerely thankful for everything they have done for me. Thank you so much, my elder brother, **Mr Sadiq Hussain Fida**, who always encouraged me to pursue higher studies. Thank you so much, my elder brother, **Mr Abdur Rehman**, for keeping me away from my responsibilities and enabling me to pursue a PhD in foreign with more focus and a relaxed mind.

I would like to thank all my teachers at the school, college and university levels, whose teaching enabled me to do doctoral research and handle the challenges of personal and professional life.

I would acknowledge my friends for their continuous emotional and moral support, who are always be with me in difficult times.

Funding

I would like to acknowledge the financial support from the National Science Center, Poland, within OPUS-13 project nr 2017/25/B/ST8/01592, Warsaw PhD School in Natural and BioMedical Sciences (Warsaw-4-PhD), and the Institute of Physical Chemistry, PAS to carry out this doctoral research work. I would like to thanks the research group "Catalysis for Sustainable Energy and Environmental Protection, IPS-PAS" for funding to participate in the conferences. I would also like to thank the iWARSAW4PhD project within the STER programme by the Polish National Agency for Academic Exchange for funding the research visit to the University of Malaga, Spain.

Declaration of Originality

I Abdul Qayyum, declare that the research work included within this present doctoral thesis was performed by myself or in collaboration with or with support from others included in the acknowledgements.

I stated that I have practiced reasonable care to ensure that this research work is original and contains no previously published results from another researcher, except where citations have been mentioned in the text. The content provided in this doctoral thesis does not violate any copyright, Polish or international law to the best of my knowledge.

I also stated that no part of my thesis has been submitted to obtain a degree or diploma previously in the Institute of Physical Chemistry, Polish academy of Sciences or any other educational institution.

I accept that the Polish Academy of Sciences has the right to use the software to detect the plagiarism of the electronic version of this thesis.

The copy right of this doctoral thesis rests with the author, and no information can be derived from it, and may not be published without the author's prior written consent.

Signature

Date

List of Publications

- **Qayyum, A**., Giannakoudakis, D. A., Łomot, D., Colmenares-Quintero, R. F., LaGrow, A. P., Nikiforow, K., LaGrow, A. P., & Colmenares, J. C. Selective (sono)photocatalytic cleavage of lignin-inspired β–O–4 linkages to phenolics by ultrasound derived 1-D titania nanomaterials. ACS Sustainable Chemistry and Engineering (Submitted).

- **Qayyum, A**., Giannakoudakis, D. A., Łomot, D., Colmenares-Quintero, R. F., LaGrow, A. P., Nikiforow, K., Dmytro Lisovytskiy & Colmenares, J. C. (2023). Tuning the physicochemical features of titanium oxide nanomaterials by altering the ultrasound parameters during the synthesis: Elevating photocatalytic selective partial oxidation of aromatic alcohols. *Ultrasonics Sonochemistry*, 106306.

- Giannakoudakis, D. A., **Qayyum, A**., Barczak, M., Colmenares-Quintero, R. F., Borowski, P., Triantafyllidis, K., & Colmenares, J. C. (2023). Mechanistic and kinetic studies of benzyl alcohol photocatalytic oxidation by nanostructured titanium (hydro) oxides: Do we know the entire story?. *Applied Catalysis B: Environmental*, *320*, 121939.

- Giannakoudakis, D. A., Zormpa, F. F., Margellou, A. G., **Qayyum, A.,** Colmenares-Quintero, R. F., Len, C., Colmenares, J. C. & Triantafyllidis, K. S. (2022). Carbon-Based Nanocatalysts (CnCs) for Biomass Valorization and Hazardous Organics Remediation. *Nanomaterials*, *12*(10), 1679.

- **Qayyum, A**., Giannakoudakis, D. A., LaGrow, A. P., Bondarchuk, O., Łomot, D., & Colmenares, J. C. (2022). High-frequency sonication for the synthesis of nanocluster-decorated titania nanorods: Making a better photocatalyst for the selective oxidation of monoaromatic alcohol. *Catalysis Communications*, 106406.

- Giannakoudakis, D. A., **Qayyum, A.,** Nair, V., Khan, A., Pradhan, S. R., Prekodravac, J., Rekos, K., LaGrow, A. P., Bondarchuk, O., Łomot, D., Triantafyllidis, K., & Colmenares, J. C. (2021). Ultrasound-assisted decoration of CuOx nanoclusters on TiO_2 nanoparticles for additives free photocatalytic hydrogen production and biomass valorization by selective oxidation. *Molecular Catalysis*, *514*, 111664.

- Giannakoudakis, D. A., **Qayyum, A.,** Łomot, D., Besenhard, M. O., Lisovytskiy, D.,

Bandosz, T. J., & Colmenares, J. C. (2021). Boosting the Photoactivity of Grafted Titania: Ultrasound-Driven Synthesis of a Multi-Phase Heterogeneous Nano-Architected Photocatalyst. *Advanced Functional Materials*, *31*(1), 2007115.

Invited Chapter

A invited chapter entitled “Sonochemistry in Material Synthesis and Catalytic Process” is under preparation for the PR Nanoscience Volume 10, edited by Prof. Neerish Revaprasadu and Dr. Malik Dilshad.

Participation in Scientific Conferences

- Participation in the "**15th European Congress on catalysis**" with a **Poster presentation** entitled "Photocatalytic selective oxidative cleavage of β-O-4 linkages of a lignin-based model compounds by novel TiO_2 nanomaterials" held at Prague Congress Centre, Prague, Czech Republic, on 27th August – 1st September 1, 2023.
- Participation in the "T**he 9th IUPAC International Conference on Green Chemistry (9th ICGC)**" with an **Oral presentation** entitled "Key role of ultrasound on the synthesis of TiO_2 nanomaterials and catalytic performance" held at Zappeion Megaron, Athens, Greece on 5th – 9th September 2022.
- Participation in the "**11th European Conference on Solar Chemistry and Photocatalysis: Environmental Applications (SPEA)**" with a **Poster presentation** entitled "Photocatalytic selective oxidation of lignin-based molecule benzyl alcohol to benzyl aldehyde by different Nano-morphologies of TiO_2" held in Turin, Italy, on June 6-10, 2022.
- Participation in the "**54th National Catalytic Colloquium**" with an **Oral presentation** entitled "Titania-based photocatalytic selective cleavage of C–C bond of a lignin-based model compounds" held at the Institute of Catalysis and Surface Chemistry. Jerzy Haber PAS, Krakow, Poland on 1 – 3 June 2022.
- Participation in the "**6th Green & Sustainable Chemistry Conference**" with a **Poster presentation** entitled "Optimization of the ultrasonic power during synthesis of TiO_2 to elevate the photo(sono)catalytic activity for additive-free partial selective oxidation of benzyl alcohol to benzyl aldehyde" organized by Elsevier which held virtually on 16th – 18th November 202.
- Participation in the "**5th EuChemS Conference on Green and Sustainable Chemistry (5th EuGSC)**," with an O**ral presentation** entitled "Ultrasonic-assisted synthesis of nanostructured TiO_2: photocatalytic selective oxidation of benzyl alcohol to benzyl aldehyde" organized by the Association of Greek Chemists (AGC) and EuChemS /Division of Green and Sustainable Chemistry which held virtually on 26th – 29th September 2021.

List of Abbreviation

TiO_2	Titanium dioxide
UV	Ultraviolet
US	Ultrasound
Xe	Xenon
N_2	Nitrogen
BET	Brunauer Emmett Teller
BJH	Barret Joyner Halenda
UV–Vis DRS	Ultraviolet visible diffuse reflectance spectroscopy
XRD	X-ray diffraction
TEM	Transmission electron microscopy
HAADF-STEM	High angle annular dark field scanning transmission electron microscopy
TGA	Thermal gravimetric analysis
XPS	X-ray photoelectron spectroscopic
TPD	Temperature programmed desorption
TPO	Temperature programmed oxidation
He	Helium
O_2	Oxygen
Ph-CH_2OH	Benzyl alcohol
PP-ol	2-Phenoxy-1-phenylethanol
LEDs	Light emitting diodes
PP-one	2-phenoxy-1-phenylethanone
Ph-OCHO	Phenyl formate
Ph-OH	Phenol
Ti	Titanium
KI	Potassium iodide
h^+	Hole
BQ	1,4-benzoquinone

$O_2^{\bullet-}$	Super oxide anionic radical
t-BtOH	Tert-butanol
OH	Hydroxyl
$AgNO_3$	Silver nitrate
e^-	Electron
GC	Gas chromatograph
Ph-CHO	Benzyl aldehyde
DSC	Differential scanning calorimetry
HF	Heat flow
CO_2	Carbon dioxide
EDXRF	Energy dispersive X-ray fluorescence
•OOH	Hydrogen superoxide radical
Rh	Rhodium
FID	Flame ionization detector

List of Units

Å	Angstrom
eV	Electron volt
kHz	kilohertz
MHz	Megahertz
rpm	Rotation per minute
µm	Micro meter
mL	Milliliter
nm	Nanometer
hv	Energy of photon
m^2/g	Square meter per gram
cm^3/g	Cubic centimeter per gram
W	Watt
°C	Degree centigrade
%	Percentage
Pa	Pascal
mM	Milli molar
cm^{-1}	Per centimeter
kV	Kilovolt
sec	Second
h	Hour
µA	Microampere
V	Volt
mW	Milli watt
°C/min	Degree centigrade per minute
mA	Milli ampere
mg	Milli gram
mL/min	Milliliter per minute

μL	Microliter
m	Meter
min	Minute
m/z	Mass to charge ratio
°	Degree

Warsaw, November 2023

Author of the doctoral dissertation: **Abdul Qayyum**

Supervisor: **Prof. Dr. hab. Eng. Juan Carlos Colmenares**

Title of the doctoral dissertation: **Titania-based photocatalysts prepared by sonication in understanding the selective oxidation of lignin-inspired molecules to phenolics**

Abstract

Lignin is considered as a vast and abundantly available renewable resource for the production of various aromatic compounds. Green and economical approaches, such as catalytic selective transformation of lignin-based model compounds to high value products by avoiding the addition of oxidizing agent and the harsh experimental conditions, are still a challenging and highly interesting research tasks. In general, titania-based materials showcase great photocatalytic performances towards the decomposition of a plethora of emerging organic pollutant. However, some dominant drawbacks such as low porosity, fast recombination of photogenerated electron-hole pairs, and an unselective photoreactivity limit the potential application for selective catalytic conversions. This research work focused on the synthesizing the novel titania based photocatalysts with the assistance of ultrasound (US) to overcome the above mentioned drawbacks and the nanomaterials to be utilized for the catalytic selective transformation of lignin based model compounds. US irradiation during the synthesis can lead to various physical and chemical effects, such as the enhanced mass transfer, de-passivation, formation of free radicals like hydroxyl etc., due to the nano-jets, localized hotspots where the temperature and pressure can reach up to 5000 °C and 1000 bars, respectively, which in result can tune the physiochemical features of the synthesized nanomaterials on demand. The physical and chemical effects depend on the utilized US frequency. Therefore, US irradiations of different frequencies (22, 40, 80 and 500 kHz) and with different amplitudes were utilized during the synthesis of titania photocatalyst via a simple slow precipitation method under ambient conditions. For the sake of comparison and to shed light on which physicochemical features are affected upon US irradiation, a titania sample was also synthesized in “silent conditions”, using magnetic stirring instead of US, while keeping all other parameters same. The synthesized photocatalysts were characterized by various techniques such as X-ray diffraction (XRD), X-ray photoelectron spectroscopy (XPS), transmission electron microscopy (TEM), thermal gravimetric analysis (TGA), nitrogen sorption (for the porosity), and

diffused reflectance spectroscopy to estimate the optical band gap. The synthesized photocatalysts were tested for the additives-free photocatalytic selective conversion of lignin inspired model compounds such as the benzyl alcohol and 2-phenoxy-1-phenylethanol in the bath catalytic reactors. The photocatalysts synthesized by using the low amplitude (30 μm) of low frequency (22 kHz) (22kHz-3) showed the highest photocatalytic conversion of benzyl alcohol (75 %) to benzyl aldehyde (67 %) as compared to all other US assisted synthesized photocatalysts. This best performing US-assisted synthesized sample (22kHz-3) showed also the highest yield of the valuable products such as benzyl aldehyde, phenyl formate and 2-phenoxy-1-phenylethanone from the catalytic conversion of 2-phenoxy-1-phenylethanol as compared to the sample synthesized in silent conditions as well as benchmark commercial titania P25 sample. These photocatalytsts were reused for up to five runs of photocatalytic experiments with the similar photoreactivity being intact and without Ti leaching to be observed. The sonophotocatalytic studies revealed that 22kHz-3 sample showed higher selective sonophotocatalytic conversion of 2-phenoxy-1-phenylethanol than photocatalytic process, resulting in an elevated aromatic balance of the reaction. The photogenerated holes were identified as the most reactive species for this photocatalytic reaction revealed by the scavengers studied. This research work showed that utilization of US after optimizing the frequency and amplitude during the synthesis steps can lead to desired materials and specific physicochemical features in order to achieve elevated selective redox photocatalytic performance.

Streszczenie

Ligninę uważa się za bogate i powszechnie dostępne odnawialne źródło związków aromatycznych. Uwzględniając wymagania ekologiczne i ekonomiczne, katalityczna selektywna transformacja związków modelowych na bazie ligniny w produkty o wysokiej wartości nadal stanowi wyzwanie i cieszy się dużym zainteresowaniem. Ogólnie rzecz biorąc, materiały na bazie tlenku tytanu wykazują doskonałe właściwości fotokatalityczne w zakresie rozkładu zanieczyszczeń organicznych, bez dodawania środka utleniającego i trudnych warunków eksperymentalnych. Dominujące wady tych materiałów, takie jak niska porowatość, szybka rekombinacja fotogenerowanych par elektron-dziura i nieselektywna fotoreaktywność, ograniczają potencjalne zastosowanie w selektywnej konwersji katalitycznej. Prace badawcze skupiały się na syntezie nowych fotokatalizatorów na bazie tlenku tytanu z zastosowaniem ultradźwięków w celu przezwyciężenia wyżej wymienionych wad oraz na nanomateriałach, które można wykorzystać do katalitycznej selektywnej transformacji związków modelowych na bazie ligniny. Fale ultradźwiękowe podczas syntezy mogą prowadzić do różnych efektów fizycznych i chemicznych, takich jak zwiększone przenoszenie masy pod wpływem nanostrumieni, tworzenie zlokalizowanych gorących punktów (w których temperatura i ciśnienie mogą sięgać odpowiednio do 5000 °C i 1000 barów), co pozwala na kontrolę właściwości fizykochemicznych syntetyzowanych nanomateriałów. Efekty fizyczne i chemiczne zależą od zastosowanej częstotliwości ultradźwięków, dlatego podczas syntezy fotokatalizatora tytanowego metodą powolnego wytrącania, wykorzystano promieniowanie ultradźwiękowe o różnych częstotliwościach (22, 40, 80 i 500 kHz) i różnych amplitudach. W celu porównania i wyjaśnienia wpływu tego promieniowania na właściwości fizykochemiczne, materiał zsyntetyzowano także w „cichych warunkach", stosując mieszanie magnetyczne zamiast ultradźwięków, zachowując wszystkie pozostałe parametry bez zmian. Zsyntetyzowane fotokatalizatory scharakteryzowano przy użyciu różnych technik, takich jak dyfrakcja promieni rentgenowskich (XRD), rentgenowska spektroskopia fotoelektronów (XPS), transmisyjna mikroskopia elektronowa (TEM), analiza termograwimetryczna (TGA), sorpcja azotu (BET) i spektroskopia rozproszonego odbicia. Zsyntetyzowane fotokatalizatory przetestowano w selektywnej konwersji związków modelowych inspirowanych ligniną, takich jak alkohol benzylowy i 2-fenoksy-1-fenyloetanol, w reaktorach katalitycznych wsadowych. Fotokatalizatory zsyntetyzowane przy użyciu niskiej amplitudy (30 μm) i niskiej częstotliwości (22 kHz) (22 kHz-3) ultradźwięków wykazały najwyższą

fotokatalityczną konwersję alkoholu benzylowego (75 %) do aldehydu benzylowego (67 %) w porównaniu do wszystkich innych syntezowanych z pomocą ultradźwięków.

Najbardziej aktywna próbka zsyntetyzowana przy udziale ultradźwięków wykazała również najwyższą wydajność w katalitycznej konwersji 2-fenoksy-1-fenyloetanolu do cennych produktów, takich jak aldehyd benzylowy, mrówczan fenylu i 2-fenoksy-1-fenyloetanon, w porównaniu ze wszystkimi zsyntetyzowanymi z pomocą ultradźwięków lub bez, a także w porównaniu z wzorcowym komercyjnym fotokatalizatorem TiO2 P25. Powyższe fotokatalizatory wykorzystano ponownie w maksymalnie pięciu kolejnych eksperymentach fotokatalitycznych, w których utrzymały wysoką fotoreaktywność bez wymywania tlenku tytanu. Badania sonofokatalityczne wykazały, że próbka 22 kHz-3 cechowała się większą selektywną konwersją do 2-fenoksy-1-fenyloetanolu niż podczas fotokatalitycznej reakcji, ponadto z podwyższoną równowagą aromatyczną reakcji. Wyłapywanie wolnych rodników ujawniło najbardziej reaktywne kwazicząstki w tej reakcji fotokatalitycznej, fotogenerowane dziury. Ta praca badawcza wykazała, że wykorzystanie ultradźwięków do syntezy materiałów, po optymalizacji częstotliwości i amplitudy, może prowadzić do uzyskania pożądanych własności fizykochemicznych sprzyjających podwyższonej selektywności w fotokatalitycznych reakcjach redoks.

Table of Contents

1. Chapter 1: Introduction 1
1.1. Lignin composition 1
1.2. Conventional lignin valorization techniques 3
1.3. Heterogeneous catalysis 6
1.3.1. Semiconductor-based heterogeneous photocatalysis 7
1.3.2. Titania based nanomaterials 8
1.3.2. Different synthesis approaches of TiO_2-based photocatalysts 10
1.4. Sonochemistry 14
1.4.1. Different parameters affecting the acoustic cavitation phenomenon 15
1.4.2. Role of US in the synthesis of nanomaterials 18
1.4.3. Role of US in photocatalysis 20
1.5. Photocatalytic applications of TiO_2 nanomaterials and limitation for selective oxidation 22
2. Chapter 2: Research hypothesis and goals 24
2.1. Hypothesis 1 and goals 24
2.2. Hypothesis 2 and goals 25
2.3. Hypothesis 3 and goals 26
2.4. Hypothesis 4 and goals 26
3. Chapter 3: Methodology 28
3.1. Materials 28
3.2. Synthesis of the catalysts 28
3.3. Physicochemical characterizations 29
3.4. Photocatalytic activity tests 31
4. Chapter 4: Results and discussion 36
4.1. Synthesis of titania samples using ultrasonication at different amplitudes of 22 kHz 36
4.1.1. Characterization of 22 kHz US-assisted synthesized samples 36
4.1.2. Photocatalytic studies of 22 kHz of US-assisted synthesized samples for partial selective oxidation of Ph-CH_2OH to Ph-CHO 48
4.1.3. Conclusions of section 4.1 51
4.2. Synthesis of TiO_2 samples with the assistance of US of 22, 40 and 80 kHz 51
4.2.1. Characterization of TiO_2 samples synthesized with the assistance of US of 22, 40 and 80 kHz 52

4.2.2. Photocatalytic performance studies of 22, 40 and 80 kHz of US-assisted synthesized samples for partial selective oxidation of Ph-CH_2OH to Ph-CHO 63
4.2.3. Conclusions of section 4.2 65
4.3. Synthesis of TiO_2 samples by the US of 500 kHz 66
4.3.1. Characterization of TiO_2 samples by the US of 500 kHz 66
4.3.2. Photocatalytic performance studies of 500 kHz of US assisted synthesized samples for partial selective oxidation of Ph-CH_2OH to Ph-CHO 74
4.3.3. Conclusions of section 4.3 76
4.4. Catalytic selective cleavage of C_α-C_β bond of lignin-based β-O-4 model compound 77
4.4.1. Photocatalytic conversion of PP-ol 77
4.4.2. Effect of calcination on the crystallinity and photocatalytic performance 80
4.4.3. Reusability and stability studies 83
4.4.4. Sonophotocatalytic oxidation of PP-ol 85
4.4.5. Potential pathway studies 88
4.4.7. Conclusions of section 4.4 94
5. Chapter 5: Summary and future perspectives 95
5.1. Outcome of hypothesis 1 95
5.2. Outcome of hypothesis 2 96
5.3. Outcome of hypothesis 3 96
5.4. Outcome of hypothesis 4 97
5.5. Future perspectives 98
6. Bibliography 99

1. Chapter 1: Introduction

1.1. Lignin composition

Lignocellulosic biomasses are considered renewable sources for biorefinery, energy production and obtaining high-value chemicals/products and materials. Lignocellulose contains three major fractions: cellulose, hemicelluloses, and lignin. Cellulose is a major fraction of biomass, containing 30-55 % of the dry woody mass and glucosidic linkages. Cellulose is a potential source for the production of cellulose-based functional materials. Hemicellulose is the second major fraction (20-40 %) of the biomass containing sugar linkages. Whereas lignin is the third major fraction, which is 15-35 % of the dry woody mass. Lignin is the only fraction containing the aromatic units that form the three-dimensional network containing aromatic linkages, which are connected by the C-O-C and C-C bonds representing the formation of complex aromatic polymers. The most representative combinatorial coupled monolignols are sinapyl alcohol, confiryl alcohol and p-coumaryl alcohol (**Figure 1.1**), which further provide the different aromatic polymers by the substitution of different groups such as syringyl, guiacyl and hyroxyphenyl [1]. These monolignols contained a different degree of methoxylation, which indicate the number of attached methoxy group with the individual monolignol moiety, such as *p*-coumaryl alcohol, which did not have any methoxy group, while coniferyl has one followed by sinapyl alcohol which has two methoxy groups. In addition to methoxy group, the lignin structure also contained some other functional groups, such as carbonyl, carboxyl, hydroxyl (OH) or phenolic group. The methoxy and phenolic groups are attached to the individual lignin monomeric unit, whereas aliphatic hydroxyl, carbonyl, or carboxylic groups are linked as substituents within the lignin structure [2].

There are different types of bonding exist in the three-dimensional network such as α-O-4, β-O-4, β-β, β-1, β-5, 4-O-5 and 5-5′ (**Figure 1.2**). Among these bonding, β-O-4 is the major existing bonding in the range of 45-55 % [3], while the other linkages α-O-4 (4-8%), β-β (2-7 %), β-1 (3-7 %), β-5 (4-12 %), 4-O-5 (4-7 %) and 5-5 (4-10 %) are also present [4–6].

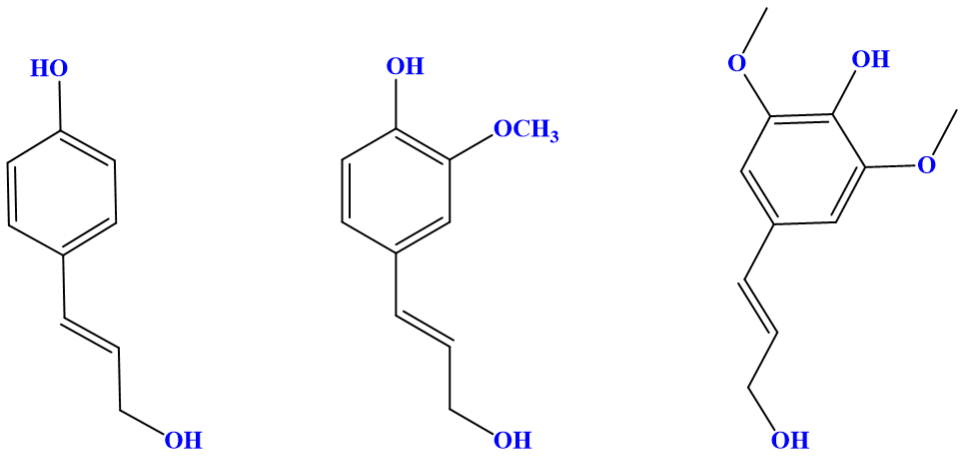

Figure 1.1. The representative lignin monomers.

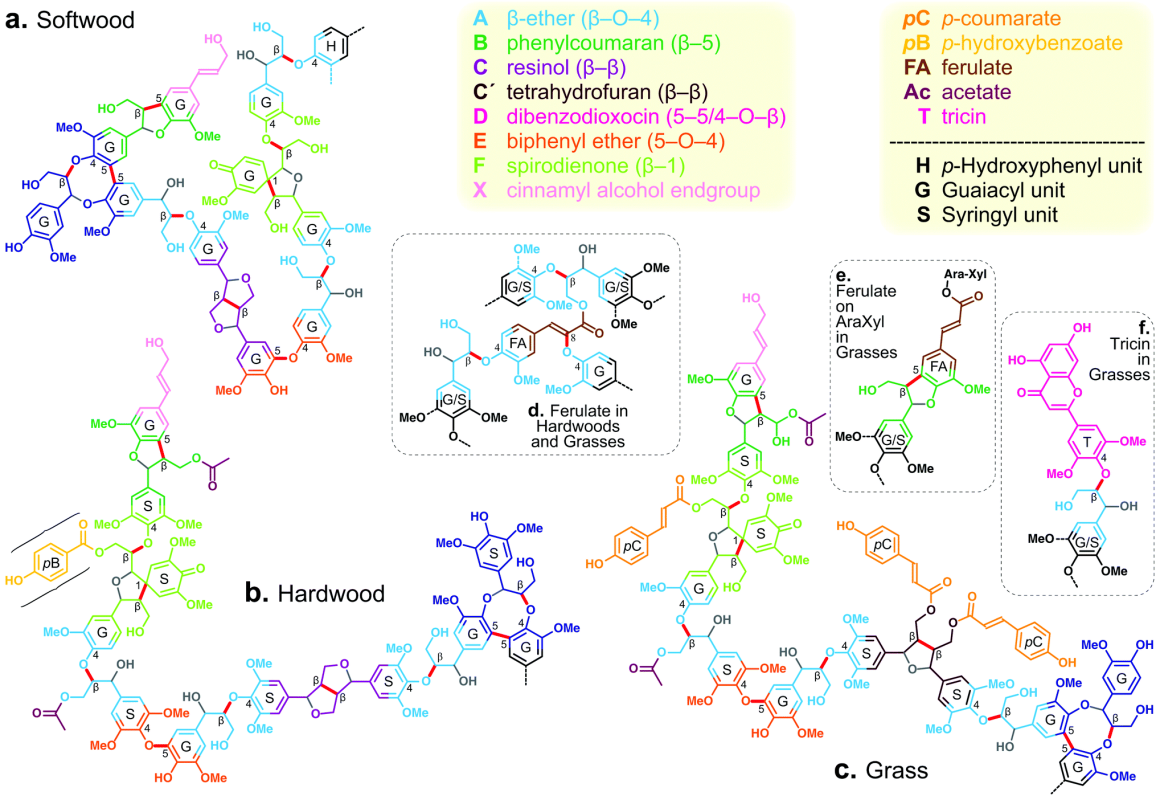

Figure 1.2. The different linkages in lignin units i.e. softwood lignin (a), hardwood (b) and grass (c). (Presented from an open access article [7], which was modified from [8] and adopted with the permission)

The lignin can be used to produce various high-value chemicals with potential applications in various industries. Around 98 % of the lignin-based waste evaluated from industries such as paper, pulp etc. are used as fuel in the burning process, whereas only less than 2 % of lignin waste is just used for the synthesis of chemical compounds such as surfactants, adhesives, dispersants and some other value compounds [9]. The demand for biomass refinery is getting increasing interest due to producing lignin residue at a larger scale. It is estimated that the production of lignin residue from biofuel production as a side product will increase by more than 200 million tons per year till 2030 [10,11]. Therefore, the lignin-based residue/waste can be converted to synthesize high-value compounds.

The reactivity of aromatic units of lignin is determined by the depolymerization reaction with the ability of the selective cleavage of C-O-C or C-C bond between these aromatic units. Various functional groups on the aromatic compounds or/and the connecting side chain, including the phenolic, aliphatic hydroxyl compound, benzyl alcohol (Ph-CH_2OH), methoxyl compounds, carbonyl and carboxyl compounds etc., which also influence the reactivity of lignin [4,12]. These compounds can be used to produce various high-value chemicals with potential applications in various industries.

1.2. Conventional lignin valorization techniques

The aromatic compositions of lignin can lead to a valuable source for producing various chemical compounds, particularly phenolics. The first step to convert the lignin to high values products is the cleavage of the existing primary linkage, resulting in the functional groups' mono-aromatic compound substitution. The oxidation of these functional groups led to the formation of the targeted compound, such as corresponding aldehydes and acids. The removal of these functional groups led to the formation of simple aromatic compounds such as phenol (Ph-OH), toluene or benzene. However, due to the complexity of the lignin structure, the selective cleavage of the lignin is a challenging task to produce the targeted products. Various valorization techniques such as hydrolysis, hydrogenolysis, gasifications, pyrolysis and chemical oxidation are used to convert the lignin to high-value compounds [13].

Lignin valorization can be performed by hydrolysis such as chemical hydrolysis (acid and alkaline) [14,15] and biological hydrolysis (enzymatic, bacterial and fungal) [16,17] etc. to enhance the

hydrolysis of lignin. This lignin valorization can be divided into different categories, such as depolymerization of the lignin, solubilization, and mineralization [18]. The lignin valorization by hydrolysis requires the pretreatment steps as well as the harsh conditions to be performed, which affect the lignin structure and ultimately lower the product's yield and increase the cost of this reaction [13].

Hydrogenolysis is also a thermal method, which is utilized for the lignin valorization by the addition of hydrogen for the cleavage of aromatic linkage. In hydrogenolysis, the solvent acts as a hydrogen donor, leading to the cleavage of C-C or C-O-C of lignin compounds and the formation of phenolic compounds [19]. Zhu et al. [20] investigated the hydrogenolysis of different aromatic compounds possessing β-O-4 linkages, which contained different functional groups such as phenolic OH groups, methoxyl and (Ph-CH_2OH) in the presence of chemical agents such as formic acid and methanol. These chemical agents act as hydrogen donors in the presence of catalysts. It was found that the β-O-4 linkage containing diaromatic compounds was directly converted to the two monoaromatic compounds. Whereas the β-O-4 linkage containing monoaromatic compounds showed a lower conversion to a complicated product distribution. The presence of methoxyl groups did not show such a hindering effect on the cleavage of β-O-4 linkages. Whereas phenolic OH groups showed a small negative impact on the cleavage of β-O-4 linkages. Lignin is depolymerized by converting into monomeric units, and the formed bond via a recondensation process is very difficult to break. Whereas the hydrogenolysis and recondensation processes are carried out simultaneously. The prevention of depolymerization of lignin is a key problem during hydrogenolysis, and the formed products are observed as complex compounds, leading to the lowering of the selectivity toward the targeted products. This less selectivity needs additional purification and separation process, which is another challenging task [21].

Pyrolysis is one the most promising techniques used to produce biofuel from lignin. Pyrolysis is the thermal process carried out at more than 450 °C in the absence of oxygen to produce a mixture of noncondensable gases, liquid and solid [22]. This is a straightforward approach for depolymerizing lignin in the small fragments representing the aromatic compounds [4,23]. Different products from the same lignin can be formed by tuning the pyrolysis process's time and temperature. Lower heating rate and temperature led to char production, while the higher heating rate and temperature, but for a short duration, led to obtaining the liquid products [9]. During the

high temperature used for pyrolysis, the breakage of different chemical linkages of lignin compounds results in the formation of volatile compounds, which can further be reduced to produce stable oligomers that can also lead to char formation by rearrangement reactions. The particle size of the raw lignin can also indirectly influence the rate of heating because of heat transfer within the different sizes of the lignin materials [22]. However, the final temperature of the pyrolysis is a crucial parameter, as it can affect the distribution of the product. Additionally, the higher oxygen contents on the obtained products, such as biofuel, lower heating rate, which is one of the key issues in this process. Thus, the use of acidic catalysts such as zeolite may help to reduce the oxygen contents and enriched in lignin base compounds such as xylenes, toluene and benzene among others. [24]. The selection of the proper acidic catalysts by considering porosity, size, shape and selectivity is a crucial aspect of the performance of the acidic catalysts as well as the physicochemical features of the obtained products [25]. Pyrolysis is the cost-effective method used for the lignin valorization. Still, the produced compounds, such as biofuel, may possess a highly reactive carbonyl or carboxylic group, which may lead to further undesirable polymerization. These obtained products by pyrolysis may also exhibit instability issues, which demand additional hydro-stabilization processes prior to further upgradation step [26].

The oxidative depolymerization of lignin can be performed by using various oxidizing agents, such as dioxygen, chlorine dioxide, peroxyacids or/and, hydrogen peroxide etc., in an alkaline medium or acidic medium or ionic liquids [27]. Oxidative depolymerization mostly leads to the more oxygen-containing functional groups such as carboxyl, aldehyde and ketone as the formed products [28]. However oxidative depolymerization can results in either the formation of aromatic compounds or aliphatic compounds. Moreover, it is also possible that the cleavage of the formed aromatic compounds is carried out, resulting in the formation of aliphatic compounds [27].

Most of these mentioned techniques used for depolymerizing the lignin were carried out in harsh experimental conditions, such as strong oxidizing agents or acidic or basic medium, which can facilitate the breakage of C-O-C linkage. However, the selective cleavage of C-C or C-O-C linkage is challenging using mild experimental conditions [29].

Catalysis is one of the key route approaches used for lignin valorization. Various research has been focused on lignin valorization using catalytic approaches such as biocatalysis, organometallic

catalysis and biomimetic catalysis [30]. Biocatalysts are considered an efficient approach for lignin valorization, but they need very specific experimental conditions due to the utilization of biological species such as enzymes, bacteria etc. [31]. Biomimetic catalysis is also utilized for the oxidation of lignin by taking advantage of metalloporphyrins in the presence of molecular oxygen or hydrogen peroxide. The electronic features of the catalysts used for biomimetic catalysis can be tuned by adding functional groups, which results in the solubility and stability of the catalysts, enhancing catalytic efficiency. The porphyrin complexes exhibited the bleaching effect, which resulted in decreasing the selectivity of the obtained products [30,32].

Organometallic catalysis involves the polyoxometalates, iron tetraamido macrocyclic complex, cobalt/manganese salen complexes and methyltrioxorhenium complexes utilized for the conversion of lignin to the high-value products. Various ligands can tune the steric and electronic properties of catalysts, which are connected to the activity, stability and solubility of the catalysts [32]. Most of the homogeneous catalytic approaches suffer from some issues, such as decomposition of the catalyst and less selectivity as well as lower separation efficiency and reusability of the catalyst, which limit these approaches for lignin valorization. Heterogeneous catalysis can overcome these mentioned disadvantages and can enhance the selective conversion of lignin to high-value products.

1.3. Heterogeneous catalysis

Heterogeneous catalysis is where the phase of the catalysts is different from the reaction medium. They include the reaction between the liquids or gases or both at the surface of the solid catalysts. The heterogeneous catalysis mostly contained the solid phase catalyst and liquid phase reaction medium. During heterogeneous catalysis, molecular adsorption, desorption or reactions occur at the catalyst's surface. Various factors such as heat transfer, pH, mass transfer and thermodynamics affect the kinetic of the reaction. Heterogeneous catalysis provides the faster and more selective formation of products and the easy recovery of the catalysts, which overcome the drawbacks provided by homogeneous catalysis [32].

1.3.1. Semiconductor-based heterogeneous photocatalysis

Photocatalysis is the rate of change of the chemical reaction by the interaction of light in the presence of a substance (photocatalyst). A photocatalyst is a substance that absorbs light and can transform the parameters in a chemical reaction. Heterogeneous photocatalysis is the acceleration of the photoreaction in the presence of a photocatalyst. Fujishima and Honda 1972 discovered the electrophotocatalytic splitting of water to hydrogen and oxygen by using titanium dioxide (TiO_2), which opened a new window for the potential research direction in the field of photocatalysis [33]. In heterogeneous photocatalysis, generally, the photocatalyst is used in the solid phase while the reaction phase is in the liquid or gas phase, and the interaction is carried out between the phases, such as solid-liquid or solid-gases. There are a few aspects which are concerned with photocatalysis, such as:

- Adsorption and desorption of reactant substrates and establishment of equilibration on the surface of photocatalyst.
- Interaction of light on the photocatalyst.
- Activation of the adsorbed reactant substrate.
- Interaction of the adsorbed reactant substrate on the surface of the photocatalyst.
- Diffusion of the products from the surface of the photocatalyst in the liquid or gas phase.

The main principles (**Figure 1.3**) of semiconductor base catalysis are as follows;

- By the irradiation of photons of the light on the surface of the semiconductor materials, if the energy of irradiated light is equivalent to or higher than the bandgap energy of the semiconductor materials, then the e^- in the valance band are excited toward the conduction band of the semiconductors.
- After the excitation of the electron, vacancies {such as holes (h^+)} are generated in the valence band of the semiconductor material, which can oxidize the donor molecules and may produce OH radicals. The OH radical possessed a higher oxidizing ability for the conversion of organic molecules.
- The e^- in the conduction band react with the dissolved molecular oxygen to form the superoxide ions, and these e^- can proceed with the reduction reaction.

The photogenerated electron-hole pairs can proceed with an oxidation or reduction process with the molecules that can be adsorbed on the semiconductor, leading to the corresponding products. The photocatalysis process mainly depends on the wavelength and the power of the utilized light source as well as the properties of the photocatalyst. Generally, semiconductor-based materials are considered good photocatalysts due to some key characteristics such as being photoactive, absorbing a range of ultraviolet (UV) and visible light, chemically and biologically inert materials, stable against light corrosion, cost-effective and least toxic. Semiconductor materials such as CeO_2, SnO_2, ZnO and TiO_2 are considered good heterogeneous photocatalysts due to compatible electronic structures with filled valance bands, empty conductance bands, and good light absorption features.

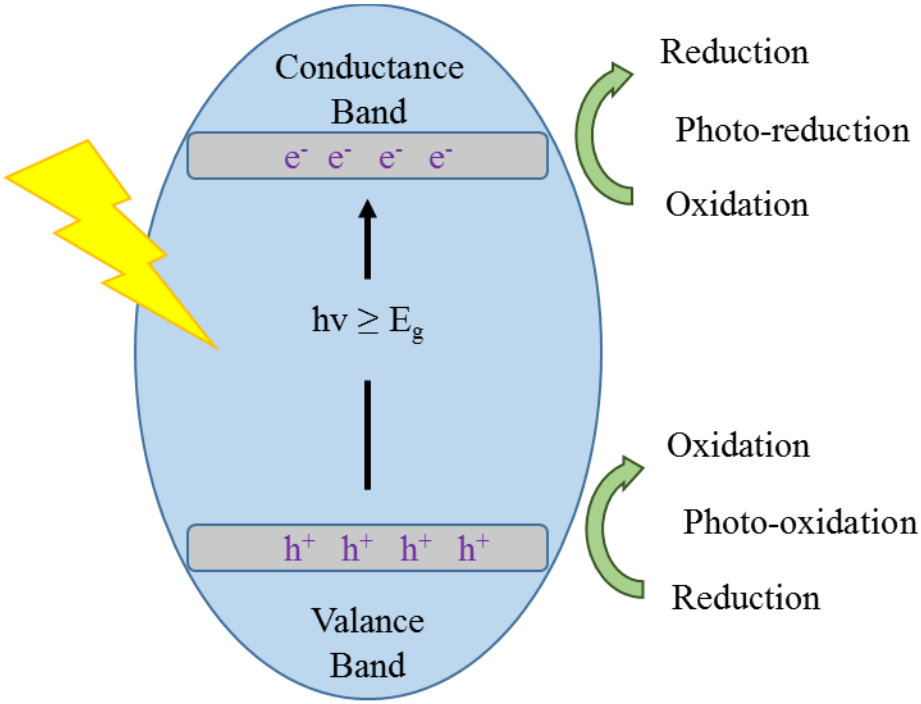

Figure 1.3. The key principle of photocatalysis.

1.3.2. Titania based nanomaterials

TiO_2-based nanomaterials are considered the best candidate for the heterogeneous catalytic process among the other semiconductor photocatalysts due to superior properties such as optical and electronic features, cost-effectiveness, eco-friendliness, and high chemical and biological stability. TiO_2 exists in three phases: anatase, rutile and brookite (**Figure 1.4)**. TiO_2 was found to be

metastable form in the anatase phase with the tetragonal crystal structure. The anatase phase of TiO_2 exists in the colourless or white colour, but it may also exist in black color due to impurities. The anatase phase of TiO_2 is usually formed at lower temperatures and is first observed in the look of TiO_2 anatase phase because of lower surface energy, while it can be transformed to a rutile phase by calcining at a higher temperature [34]. Whereas the rutile phase is the most stable phase of TiO_2, and once it is formed, it grows very fast [35,36], and has a higher refractive index at a higher wavelength of light compared to the UV region [37]. The rutile phase has a tetragonal structure [36]. The anatase photocatalysts were found better compared to the rutile phase [38]. Anatase phase of TiO_2 possesses a band gap of 3.2 eV, while the rutile phase of TiO_2 showed 3.0 eV bandgap [39]. The bandgap of the photocatalyst is inversely proportional to the absorption of light, suggesting that the rutile phase has higher light absorption than the anatase phase. This increased photocatalytic activity may be due to higher fermi levels, less ability toward oxygen adsorption and higher hydroxylation degree observed in the anatase phase [40]. Another possible reason is that the lifetime of photogenerated electron-hole pairs in anatase was found to be higher compared to the rutile phase, which results in the higher charge carrier can participate in the anatase phase [41].

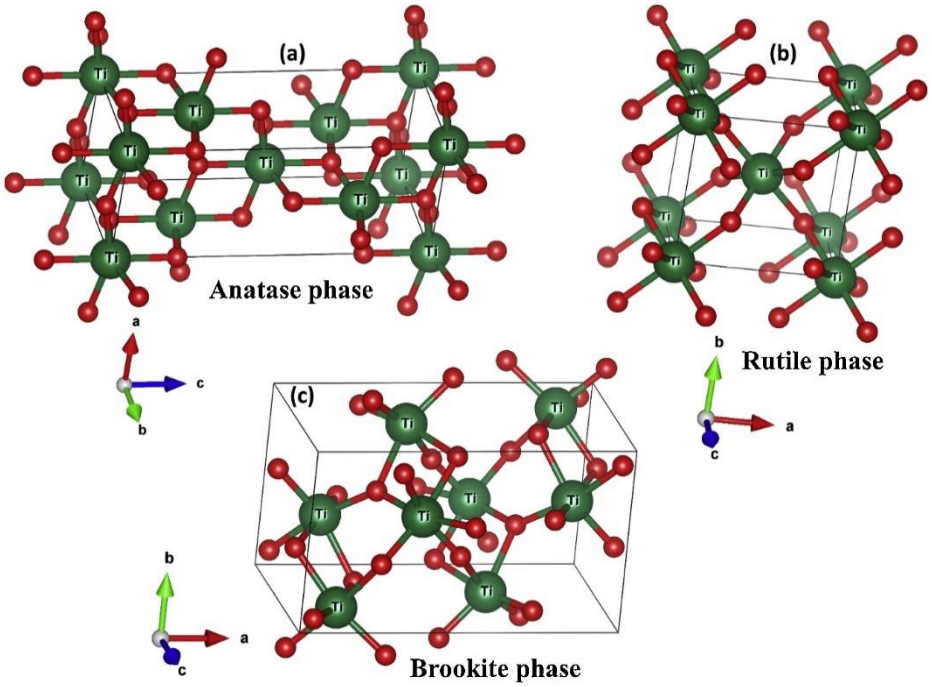

Figure 1.4. Different phases of TiO_2. (Presented with the permission of reference [37])

Brookite is the third phase of TiO_2, which is rare compared to its anatase and rutile phases. It possesses an orthorhombic structure [41,42]. The brookite phase is also metastable and shows a low symmetric and complicated structure, and its formation usually occurs as the secondary phase of the anatase or rutile phase [43]. The brookite phase TiO_2 photocatalyst showed a bandgap in the range of 3.1 to 3.4 eV, which contained a lower and higher bandgap than the anatase phase, and it depend on the utilized synthesis method [44].

The brookite phase TiO_2 showed higher photocatalytic activity compared to anatase and rutile TiO_2. Kandiel et al., [45] studied hydrogen production by the photocatalytic activity using different phases of TiO_2 photocatalysts. It was found that the anatase/brookite mixtures, as well as pure brookite TiO_2 photocatalyst showed higher photocatalytic hydrogen production under UV light irradiation. This is ascribed to the edge of the conduction band of brookite photocatalyst being more shifted toward the cathodically as compared to the anatase phase. However, the photocatalytic activity of brookite phase photocatalyst is not well explored due to the difficult and complex synthesis of the pure brookite phase [46].

1.3.2. Different synthesis approaches of TiO_2-based photocatalysts

Various synthesis methods, such as sol-gel, hydrothermal, oxidation, solvothermal, electro-deposition and chemical vapour deposition among others, are being used to prepare the TiO_2-based photocatalysts (**Figure 1.5**). Sol-gel is one of the most commonly used methods to synthesize nanomaterials, which can tune the surface characterization and the textural features of the synthesized materials [47]. The sol-gel is proceeded by a few steps, such as mixing, dehydration, ageing, densification and some other steps to synthesize the final materials. The sol-gel method starts with forming a stable colloidal solution or a sol by hydrolysis or/and polymerization of the precursor compounds, which can be metallic organic compounds or inorganic metallic salt in the form of chloride, nitrate or alkoxide etc. The complete polymerization and dehydration lead to the formation of a gel phase after the ageing and drying steps. The mechanism of the sol-gel method can be tuned by hydrolysis with the acidic or basic solvent in order to obtain the targeted features of the synthesized materials [48–50].

Various factors such as selection of solvent, temperature, ageing time and drying, pH and some others are the key parameters to alter the physicochemical properties of the synthesized materials

[51]. For example, the particle size of the synthesized materials by sol-gel can be controlled by the effect of the condensation reaction and the hydrolysis's rate [48]. The sol-gel presents various advantages such as mild synthesis parameters, low-temperature synthesis, high purity of synthesized materials and synthesis of homogeneous materials. However, some limitations, such as complex preparation protocol, low yield and scalability, moisture sensitivity, formation of possible byproducts etc., are also associated with the sol-gel method and can detract from the targeted application of the synthesized nanomaterials [49].

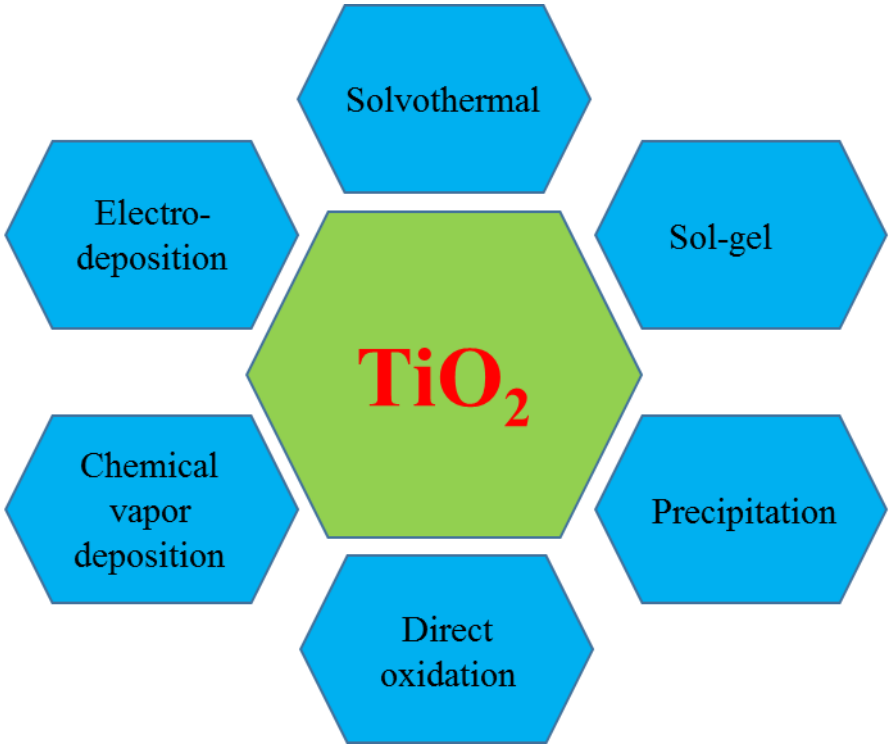

Figure 1.5. The most commonly used methods for the synthesis of TiO_2.

The solvothermal method is also one of the commonly used approaches for synthesizing TiO_2 materials. This method needs high pressure and temperature to carry out the chemical reaction or the transformation of the precursor solution to prepare the targeted materials. The solvothermal method can use different solvents, such as ammonia, water, hydrofluoric acid, hydrochloric acid, etc. When water is used, this method is termed as a hydrothermal method. The precursors of the desired materials are mixed in the solvent in an autoclave. The autoclave is used as a closed system to heat at a higher temperature than the boiling point of the solution; and high pressure can be maintained, and crystallization can be achieved. The high pure and homogeneous materials can be

synthesized using this method with the controlled size using the proper composition of the selected precursors and the experimental parameters. Various parameters such as pH, selection of temperature and pressure, and the composition of precursors lead to altering the synthesized materials' phase, morphology and size [52,53]. The solvothermal and hydrothermal methods have many advantages such as cost-effective, one-step synthesis, environmentally friendliness etc. [54]. However, these methods require expensive autoclaves, high temperatures and pressures, and the synthesis of pure crystal growth is difficult to control [55].

The electro-deposition is also a commonly used method to synthesize the TiO_2 catalysts. Electrochemical deposition is carried out at the interface of the electrolyte solution containing the targeted metal to be deposited and the electrically conductive metallic substrate [56]. Different studies are also reported for two steps electrochemical deposition synthesis of TiO_2 catalysts. For example, in the first step, the TiO_2 or hydroxide, is formed at the surface of the electrode either by the hydrolysis of titanium (Ti) precursor or the electrochemical oxidation process [57]. Another step is the TiO_2 or hydroxide is formed by the electrochemical hydrolysis of Ti (IV) precursor [58]. Further thermal calcination steps lead to the synthesis of crystalline TiO_2. The electrochemical synthesis presents some advantages, such as controlled formation of the formed layer, homogeneous coating, direct development of metal on the conductive materials and well-established connection between the supporting electrodes and the deposited materials [59]. However, there are some disadvantages, such as a supporting electrode is also required to avoid the combination of the utilized electrolyte, which can be expensive. Another non-homogeneous electric field in the reactor creates the hot spots, which can hinder the current flow through the reaction [57].

Chemical vapour deposition is one of the old synthesis approaches used to synthesize semiconductor-based materials [60]. This method describes the condensation of the substances in the vapour form or the gaseous compounds to form the solid form materials by the chemical reaction of these vapour compound and the surface of the material which need to be coated. During the chemical vapour deposition synthesis of TiO_2, the volatile substances pass through the surface of the material to be coated, which results in the formation of the solid phase, leading to the deposition on the surface. The temperature of the substrate is a crucial aspect as it influences the way of the chemical reactions occur at the surface of the substrate [61]. The chemical vapour

deposition method leads to the formation of a uniform film of low porosity with high stability and purity, whereas it needs highly expensive instrumentation and the additional cost of protective and safety from the used chemical agents for this method [62].

TiO_2-based nanomaterials can be synthesized via the oxidation of Ti metal by using an oxidizing agent or through the anodization process. The direct oxidation of the Ti metal using oxidizing agents such as hydrogen peroxide results in high crystalline TiO_2 materials [63]. Whereas the direct oxidation of the Ti metal by using different inorganic salts leads to the different crystalline phases of the synthesized TiO_2. For example, by using sodium fluoride or sodium sulfate as an oxidizing agent, the synthesized TiO_2 will have an anatase phase, while using sodium chloride leads to rutile phase TiO_2 materials [64]. The use of these chemical oxidizing agents is mostly costly, and the toxic lead to hazardous material [65].

The chemical precipitation approach is one of the most common methods used to synthesize TiO_2. The chemical precipitation method is the complete precipitation of the metallic solution in the insoluble form of materials. The precipitation method can lead to synthesizing materials of high surface area. In this process, a solution of the precipitation agent, such as hydroxide, oxalate carbonate etc., is added to the cationic solution of targeted oxides. The chemical precipitation method can proceed through homogeneous precipitation, co-precipitation and direct precipitation [66]. The insoluble form of the materials is obtained by settling down this mixture or filtration. The key steps involved in this process are precipitation, neutralization, coagulation, and solvent removal. Various factors, such as the selection of the type of metal and its concentration in the solution, selection of precipitating agent and condition of the parameters among others, may affect the precipitation synthesis of the materials [67]. pH value of the solution is the key parameter in the precipitation method, which can be used by using the proper metallic hydroxide. Hydroxide precipitation is most commonly used for chemical precipitation methods by using sodium hydroxide, ammonium hydroxide or calcium hydroxide as a precipitating agent [68]. The key advantage of the precipitation method is the high yield of the materials that can be obtained, high purity, cost-effective and more reproducibility with homogeneous precipitation reaction [69].

The sonochemical synthesis method is also beneficial to synthesize TiO_2 catalysts with elevated textural, surface and morphological properties [70]. The use of US leads to the acoustic cavitation

phenomenon, which impacts the different physical and chemical effects depending on the utilized frequency of the US during the synthesis. Various aspects of US play a key role in altering the physicochemical features of the synthesized materials, which should be discussed in detail.

1.4. Sonochemistry

The chemical reactions are usually carried out by traditional energy sources such as heating, sand bath, light, among others, but these energy sources are generally established by temperature gradients leading to the other side effects. So, alternative sources such as US, microwave, electrical energy, etc. should replace these traditional sources, which facilitate restricting these temperature gradients to avoid side effects [71]. Sonochemistry describes the effect of energy produced by US leading to the physical and chemical processes in the liquid phase [72].

The US is the most promising technique, which can produce high energy that can be localized to US wave-carrying medium, leading to the potential to initiate the chemical reaction [73]. Sonochemistry is the use of US energy in various fields. The frequency of the US is divided into three different regions. The US of less than 20 kHz the frequency which is audible by normal humans. The US in the range of frequency 20 kHz to 2 MHz is related to the sonochemistry and has a different effect on a different frequency in this range. Whereas, the US of frequency higher than 2 MHz is mostly used for diagnostic purposes [74]. The US is causing the sono-chemical effects by taking advantage of the cavitation phenomenon. The propagation of US waves in the liquid medium leads to the compression and rarefactions patterns resulting in the creation of positive and negative pressure, which can have the push or pull behaviour for the liquid molecule to move either toward or away from each other. (**Figure 1.6**). This process generates energy for the liquid phase, forming cavitation [75]. The formation of the cavitation describes how the gaseous bubbles form, grow and collapse. When a liquid is subjected to US irradiation, the vapour pressure of this liquid becomes higher than the pressure of the liquid, which creates a cavitation bubble containing liquid vapour and gasses [76].

After forming these cavitation bubbles, the bubbles absorbed energy from the further US irradiation and grew, followed by the bubble's collision. The collision of the cavitation bubbles leads to the formation of the localized hotspot, and the temperature and pressure increase up to 5000 °C and 1000 bars, respectively [77], which can significantly accelerate the chemical

reactivity of the medium and can be utilized for various purposes. This acoustic cavitation bubble formation can have different intensities, which determine the rate or the productivity of the sonolysis [78].

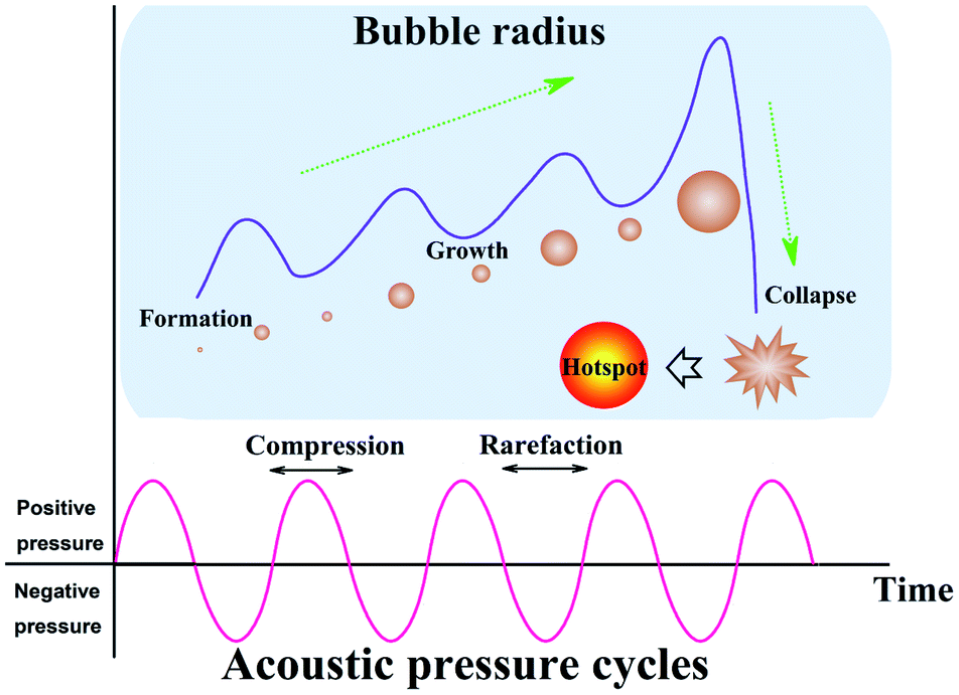

Figure 1.6. Schematic presentation of the formation of hot spots by the US. (Presented with the permission of reference [78])

1.4.1. Different parameters affecting the acoustic cavitation phenomenon

Various parameters of the US play key roles in significantly different effects of the US, which can be utilized for the other targeted applications. The details of these parameters are discussed as follows:

1.4.1.1. Effect of frequencies

The frequency in the sonochemistry range is divided into two different regions based on their produced effects. The first range of the frequency lies in the range of 20-100 kHz, followed by the range of 100 kHz - 2 MHz [73]. The utilized frequency of the US affects on the produced cavitation bubbles. For example, the frequency in the range of 20 - 100 kHz leads to the formation of large-size cavitation bubbles and their collapsing lead to the physical effect of US such as high-speed jets, shock jets, mass transfer etc. (**Figure 1.7**) [79]. The physical effect of the US is mostly used

for the synthesis of materials, crystallization, emulsification etc. [80]. Whereas the increase of the frequency above 300 kHz, the size of the produced cavitation bubbles was observed in the decreasing trend but the gradually increasing number of the cavitation bubbles. These low-size cavitation bubbles form free radicals, which produce the chemical effect of US that can be potentially used for various chemical reactions and other scientific purposes [79,81].

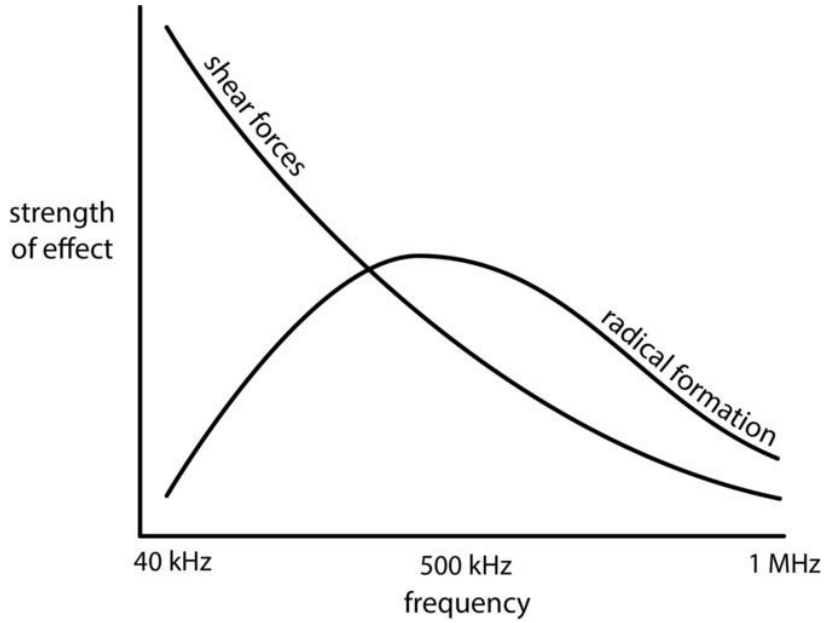

Figure 1.7. Effect of different frequencies of US. (Presented with the permission of reference [79])

1.4.1.2. Effect of intensity

The intensity of the US is a determining parameter for the formation of the cavitation bubbles. Each frequency's threshold intensity can facilitate sufficient energy to produce cavitation bubbles [74]. Brotchie et al. [82] measured the sizes of cavitation bubbles by using different frequencies with different intensities. They found that the mean size of the cavitation bubbles increased with the increased intensity of the studied frequency. In the case of increasing the frequency, this observation was found in reverse trend, as the mean size of the cavitation bubbles was found in decreasing trend with the increase in the frequencies.

The intensity of US is proportional to the amplitude of the US waves. As the intensity of US increases, the sonochemical effect also increases due to an increase in the amplitude of the US waves, which results in a higher number of cavitation bubbles. Nevertheless, some of the formed

bubbles may combine to form bigger and enlarged bubbles, which can be a barrier to the movement of US energy through the liquid medium [73]. High intensity of the US led to some other factors like damaging the US transducer and lack of movement of the US power to the liquid medium due to the formation of more bubbles, and their collapses did not increase the US energy in the sonicated system [71]. The dynamic of the cavitation bubbles can be co-related with the usage of high intensity of US [83]. The use of the optimum intensity of the frequency may lead to better utilization of US.

1.4.1.3. Effect of geometry and distance of US transducer

The geometry and the distance of the US transducer to the liquid medium lead to the formation of different acoustic fields in the US reactor, which also affects the formation of cavitation bubbles. A slight modification in the geometry of the US transducer may change the sonochemical reaction. Santos-Zea et al. [84] studied four different geometries of US transducer, such as base model, cylindrical hreadmass, circular section sonotrode and multiplate configuration of 30 kHz sonicator using similar power for the extraction of the antioxidant compound from oregano source. It was found that all these geometries did not produce the same sonochemical effect. The multiple configuration transducer showed higher sonochemical activity by increasing the irradiation surface and also improved the US energy's distribution in the whole treated area. Whereas circular section sonotrode showed the least sonochemical activity as it distributed the US energy in the smaller area. Moreover, the distance of the US transducer from the sonicated liquid also affects the sonochemical activity. Recently, Son et al. [85] studied the effect of different distances (in the range of 80-340 mm) of US transducers of 36 and 108 kHz of cylindrical shape sonicators. It was found that the cavitation yield was observed in an increasing trend with the increased liquid height or irradiation distance. Moreover, the stable and stronger standing field was observed with greater sonoluminescence activity at the higher liquid height or irradiation distance.

1.4.1.4. Factors affecting the acoustic cavitation phenomenon

Various factors, such as vapour pressure, dissolved gasses, solvent, reaction temperature and some others, can affect acoustic cavitation's intensity. Utilizing a proper solvent for sonication is one of the key factors, which possess some physical aspects such as vapour pressure, surface tension, viscosity and some other factors that can affect the formation of acoustic cavitation [86]. The

cavitation phenomenon needs pressure to be initiated during the rarefaction cycles to disrupt the cohesive forces of the used solvent, resulting in a vacuum's creation. The viscosity of the used solvent is another aspect, as the higher viscosity or higher surface tension impacts the higher molecular interactions, significantly increasing the cavitation threshold [87]. The solvent's vapour pressure also affects the cavitation bubbles' collapse. The lower vapour pressure leads to more intense collapsing than the high vapour pressure [88]. Also, the higher vapour pressure with low surface tension and the viscosity of the used solvent improves the formation of the cavities [89]. The higher temperature can also improve the formation of cavitation bubbles. However, it may give the reverse effect, such as a higher temperature leading to the easier formation of bubbles, but it may contain higher vapours, which can lead to a decrement in the overall formation of the cavitation bubbles [90]. These effects suggested that the consideration of these factors can perform the selection of solvent for the sonication.

The dissolved gasses in the sonicated liquid also tune the formation of cavitation bubbles. The dissolved gasses act like a small spot in the liquid and can form a higher number of cavitation bubbles. The other factors of the dissolved gas, such as a higher heat ratio, provide more giant cavitation bubbles and high solubility facilitation with a higher nucleation effect of cavitation [91]. Moreover, during the compression of the bubbles, the interfacial area shrinks. At a similar time, the dissolved gasses also diffuse toward the outer side. More diffusion of the dissolved gasses inside the cavitation bubbles leads to an increment in the area of the bubbles [92].

1.4.2. Role of US in the synthesis of nanomaterials

The US-assisted chemical reactions for synthesizing the nanomaterials are termed as sonochemical synthesis and are most widely explored. The US energy coming from acoustic cavitation is the main driving attribution to the sonochemical synthesis [93]. The most prominent phenomena involved in the sonochemical synthesis of nanomaterials are shock waves and microjets (**Figure 1.8**) [94]. The shock waves are produced by the spherical collapsing of the bubbles, which results in the yield of high ($\geq$ 10 kbar) pressure [95]. Whereas, a hetero-phase surface causes cavitation bubbles to form, leading to high-speed microjet development [96]. Most acoustic cavitation bubble energy is transported to accelerate the microjet phenomenon, increasing the microjet velocities [95].

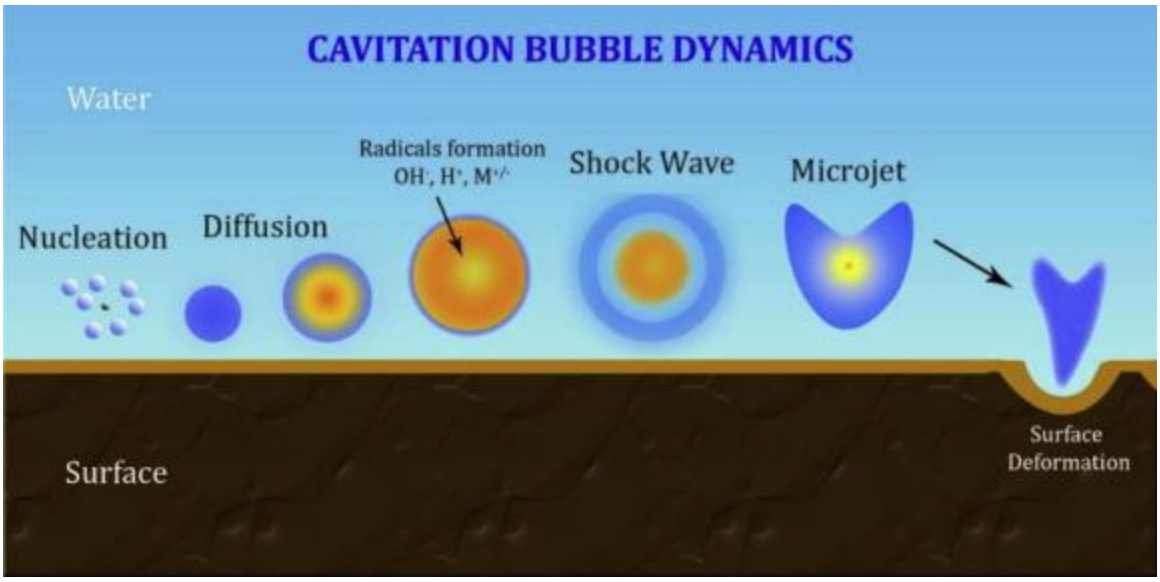

Figure. 1.8. The systematic presentation of the acoustic cavitation phenomenon. (Presented with the permission of reference [94])

The formation of microjets distorts the collapsing of the cavitation bubbles, which results in the surface deformation of the synthesized materials [94]. Sonochemical synthesis consists of two types such as homogeneous and heterogeneous chemical synthesis, based on the nature of the acoustic cavitation [97]. Homogeneous chemical synthesis takes advantage of the applied US as physical and chemical effects on the synthesis of the nanomaterials. In the case of heterogeneous chemical synthesis, the physical effect plays a major role, as the shock waves provide the drastic transformation of smaller particles to impose the collision and then enhance the microjet phenomenon due to the boundary effect. The nucleation and the cavitation bubbles lead to the fracture-forming particles to synthesize the fine nanomaterials [98].

The physical effect of US can enhance the rate of a chemical reaction during the synthesis by better mass mixing effect heat transferring phenomenon, which results in the tuned structures of the synthesized materials such as deformation, fragmentation, exfoliation and erosion etc. [99]. The important driving force to form the crystalline lattices is the generation and relaxation of the mechanical forces [100]. The US provides sonicated energy, which results in a diverse consequence of the lattice formation, which cannot be facilitated by the other synthesis techniques [101]. The key benefit of using the US to synthesize the nanomaterials over the other conventional techniques is obtaining the tuned properties such as higher porosity, high purity, and more uniform

distribution of particle size [102]. Yu et al. [103] synthesized the TiO_2 nanoparticles leads by using the mixture of water and ethanol containing titanium tetra isopropoxide which was irradiated with the assistance of 20 kHz of US for 3 h. US lead accomplished three steps such as hydrolysis of titanium tetra isopropoxide, crystallization and extraction of surfactant in one step. The US assisted synthesized TiO_2 samples showed more than two times higher photocatalytic oxidation of n-pentane as compared to commercial TiO_2 sample P25.

Compression and rarefactions cycles of the sound waves were observed for a shorter time by using the high-frequency of US. The generation of the acoustic cavities needs time to pull out the molecule, but this cycle for a short time makes it problematic to form the cavitation [104]. However, in the lower range of high-frequency US, the cavitation bubbles are produced but are less violent. But in the case of a high range of frequency, cavitation events happen so quickly that the lifetime of these events is very short, resulting in the production of free radicals, which result in the chemical effect of US [105]. Ghows et al. [106] prepared the TiO_2 nanomaterials by the hydrolysis of the precursor of the TiO_2 under the low intensity of high-frequency US (500 kHz). The obtained TiO_2 nanomaterials showed the formation of nanoparticles of less than 10 nm and a single anatase crystalline phase. However, these authors did not study any photocatalytic activity.

1.4.3. Role of US in photocatalysis

US is a versatile approach used for various purposes. When the US waves pass through the aqueous liquid, they produce sonolysis, which may lead to the splitting of water and generate free radicals. This sonolysis phenomenon may proceed via acoustic cavitation, nucleation, the dynamic of the cavitation bubbles and chemical process [107]. There are some key advantages which are associated with the sonophoto-catalysis. For example, increased formation of free radicals depending on the used frequency also facilitates the chemical reaction. The enhanced mass transfer between the liquid phase and catalyst leads to improved light-harvesting for this process. Moreover, the US waves improve the mass transfer leading to the whole volume of the catalyst, including the shield part of the catalyst, high concentration or slurry concentration of the catalysts can participate in the catalytic process [108]. Coupling various US effects, such as de-aggregation, de-passivating effect among others, improves the provided surface area of the catalyst, enhancing the catalytic performance [109].

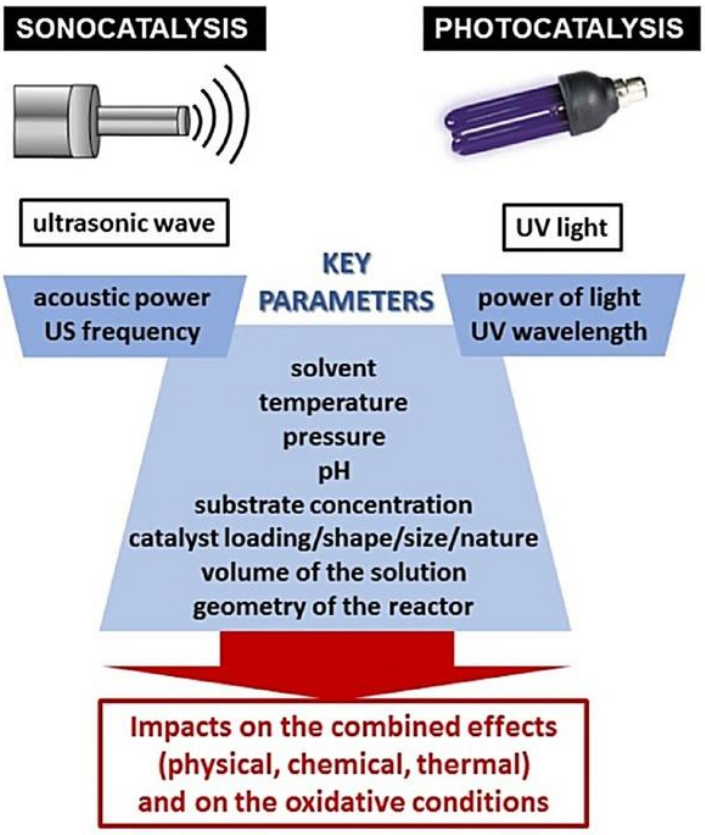

Figure. 1.9. The factors affecting sonophotocatalysis. (Presented with the permission of reference [110])

There are various factors, such as the frequency and intensity of US, solvent, the operating temperature of the reaction, pressure, pH, initial concentration of the substrate and catalysts, the volume of the solution, the geometry of the reactor, etc., which affect the sonophotocatalysis (**Figure 1.9**) [110]. The mechanism of sonophotocatalysis leads to the same effect that governs photocatalysis. The photocatalytic conversion of the organic compounds in an aqueous medium is carried out by the OH radicals formed during the photolysis. The combination of the US irradiation with the photocatalysis enhanced the rate of the conversion of the organic compounds via the additional production of free radicals. The presence of the solid catalysts also enhances the generation of the cavitation bubbles via facilitating the additional nuclei, which results in the cleavage of water and the generation of OH radicals. This phenomenon proposes that the US irradiation on the semiconductors may also facilitate the generation of OH radicals [111]. The sonophotocatalytic activity of the heterogeneous catalyst enhanced the conversion of the organic

compound as compared to photocatalytic and sonocatalytic activity [112].

1.5. Photocatalytic applications of TiO_2 nanomaterials and limitation for selective oxidation

The TiO_2-based photocatalysts are widely used for the conversion of organic pollutant compounds, and they showed complete conversion of the organic compounds under UV light irradiation. Nevertheless, this conversion of the organic compounds is unselective to the targeted products. Various factors can be potentially responsible for this non-selective photocatalytic activity of TiO_2-based photocatalysts. For example, Marotta et al. [113] studied the photocatalytic activity of pure anatase TiO_2 photocatalyst for selective oxidation of Ph-CH_2OH under the UV light irradiation, 72 % conversion of Ph-CH_2OH to 35 % and 8 % selectivity toward the benzyl aldehyde (Ph-CHO) and benzoic acid, respectively. Another researcher, Augugliaro et al. [114] investigated the photocatalytic activity of the TiO_2 catalyst for the conversion of aromatic alcohol to the aldehyde. This investigation showed the 50 % conversion of Ph-CH_2OH with 28 % selectivity and 65 % methoxybenzyl alcohol with 41 % selectivity toward the corresponding aldehydes.

There are various factors associated with TiO_2 catalysts, which lead to lower selectivity of the targeted products. One of these factors is the free radical intermediates participation in chemical reactions carried out under UV light irradiation. Especially when these photocatalytic selective oxidations of aromatic compounds are performed by the addition of molecular oxygen as an oxidizing agent. The attachment of molecular oxygen may easily lead to the formation of free radical intermediates, which can result in different uncontrollable products [115]. Another, UV light irradiation may lead to the production of different oxygen species, which can also lead to the formation of non-targeted products [116].

Some prominent drawbacks such as low specific surface area, low pore volume, and fast recombination of photo-generated electron-hole pairs, which are associated with the characteristic properties of TiO_2, may also lead to unselective photocatalytic activity [117,118]. Moreover, the use of reagents, such as bromine and chlorine, among others for the photocatalytic selective oxidation of aromatic alcohol by using TiO_2 is corrosive, and this leads to the unselective transformation of this aromatic alcohol [119]. The surface features of the TiO_2 nanomaterials possessed less adsorption of the targeted substrate, such as Ph-CH_2OH, and it leads to limited adsorption phenomena. Moreover, the agglomeration and aggregation of TiO_2 nanomaterials also

restrict light penetration, resulting in lower selective conversion of Ph-CH_2OH [120]. The excess photocatalytic oxidation of Ph-CH_2OH leads to the generation of undesired products, such as aliphatic compounds, which also lowers the selectivity toward the Ph-CH_2OH [121]. The synthesis of novel TiO_2-based photocatalysts which can overcome the above-mentioned characteristic features and the mild reaction parameters even without the addition of an oxidizing agent, which leads to the selective performance of the catalytic oxidation of various aromatic compounds to the corresponding products, is a challenging task.

2. Chapter 2: Research hypothesis and goals

Selective conversion of lignin-based aromatic molecules to the corresponding products is highly desirable for industries and bio-refineries, as these feedstocks are of low cost, renewable and abundantly available, one of the most abundant sources of various aromatic compounds. Due to the complexity of lignin structure, the conversion of lignin-based model molecules is a challenging task. Developing a green and more sustainable approach is highly desirable for converting lignin-inspired model molecules. Semiconductor-based heterogeneous catalysis is considered among the most promising materials for this purpose. As mentioned previously, TiO_2-based nanomaterials are considered the most active photocatalyst for the degradation of organic compounds, but they possess unselective transformation, which limits their applications for synthetic applications where the yield and selectivity towards the targeted products are the ultimately important goal. Therefore, the designing and synthesis of novel TiO_2-based photocatalysts is a very prosperous part of determining the feasibility of utilization for selective transformation. Sonochemistry is one of the key driving attribution used for synthesizing nanomaterials. The optimization of the frequency and amplitude of US for synthesizing nanomaterials can lead to tuned on-demand physiochemical properties and catalytic performance owing to the advantages of the cavitation phenomenon. In this doctoral research, the key established objective was to convert the lignin-based model molecules via heterogeneous catalysis using TiO_2-based photo-catalysts prepared by US assistance.

The proposed hypotheses of this doctoral research work are as follows:

2.1. Hypothesis 1 and goals

US irradiation can have chemical and physical effects, depending on the frequency, which can vary in the range of 20 kHz to 2 MHz. The frequency and amplitude both significantly affect the cavitation phenomenon, such as the size of the formed bubbles and size distribution. The frequency in the range of 22 kHz to 100 kHz results in large-size cavitation bubbles forming, which predominately leads to physical effects such as microjets, turbulence, better mass transfer and shock waves. While the intensity of the chemical effects is more pronounced as the frequency rises from 100 kHz and above. The amplitude of the applied frequency determined the sufficient energy supplies to induce the cavitation. The frequency and the amplitude are the key parameters to utilize

the sonochemistry to achieve the targeted goal. Therefore, the first hypothesis is to design and synthesize TiO_2-based nanomaterials by using low frequency (22 kHz) may take advantage of the derived physical effects during the synthesis that can affect/control the growth of the crystals. Furthermore, it is also hypothesized that different powers/amplitudes of the same US frequency (22 kHz) may impact differently the material's crystallization and, as a result, the photocatalytic performance of the synthesized nanomaterials can be tuned accordingly.

The key objectives coming from the hypothesis 1 are as follows;

- To study the effect of US on the physiochemical features of the US-assisted synthesized TiO_2-based nanomaterials as compared to the nanomaterials synthesized without US irradiation.
- To understand the role of the different amplitudes of US (22 kHz) on the synthesized nanomaterials.
- To explore the photocatalytic performance of 22 kHz assisted synthesized nanomaterials for the selective partial oxidation of Ph-CH_2OH to Ph-CHO.

2.2. Hypothesis 2 and goals

The dynamics of the cavitation bubbles, such as the size of cavitation bubbles and size distribution, are significantly different at different operating frequencies. In the case of low frequencies, the size of cavitation bubbles decreases by increasing the frequency from 20 kHz-100 kHz, results in lowering the physical effect of US. It is hypothesized that utilization of the different frequencies in this range during the synthesis of nanomaterials results in the altering the physiochemical features as well as the photocatalytic efficiency of these synthesized nanomaterials due to a decrease in the physical effects of the US. The key goal is to synthesize the catalysts with the assistance of 40 and 80 kHz US by using the optimized amplitude of 22 kHz and compare the nanomaterials in terms of characterization and photocatalytic performance.

The key objectives coming from hypothesis 2 are as follows;

- To understand the effect of different frequencies of US on the porosity, morphology, surface heterogeneity, and size of the US-assisted synthesized nanomaterials.

- To investigate the additive-free photocatalytic activity of nanomaterials synthesized by different frequencies of US for the partial selective oxidation of Ph-CH_2OH to Ph-CHO.

2.3. Hypothesis 3 and goals

The increase in the frequency from mid to high in the range of 300-800 kHz of US irradiation, high numbers of small-size cavitation bubbles are produced, and the collapsing of these small-size cavitation bubbles can impact the chemical effects such as radical polymerization and increase in the rate of sonochemical radical formation. It is hypothesized that the utilization of high-frequency US during the synthesis step of TiO_2-based nanomaterials can influence the synthesis due to the potential chemical effect of US, resulting in the tunable physiochemical properties of the synthesized nanomaterials compared to the physical effect of US. Therefore, by taking advantage of this knowledge, the synthesis of TiO_2-based nanomaterials is designed using the different amplitudes such as 30 and 70 μm of 500 kHz of US.

The key objectives coming from hypothesis 3 are as follows;

- To understand the effect of high-frequency US on the synthesis of nanomaterials.
- To explore the altered physicochemical features of the 500 kHz US-assisted synthesized nanomaterials.
- To study the photocatalytic partial selective oxidation of Ph-CH_2OH to Ph-CHO without the addition of oxidizing agents.

2.4. Hypothesis 4 and goals

Lignin contains β-O-4 linkage between the aromatic structures, which is considered the richest unit of lignin. It is presumed that the selective catalytic cleavage of this β-O-4 linkage may lead to the formation of various valuable phenolic compounds. So, it is hypothesized that the US-assisted synthesized photocatalyst, which showed the highest yield of Ph-CHO from the conversion of the monoaromatic compound such as Ph-CH_2OH can also have the ability to form the higher selective cleavage of C_α-C_β bond of the β-O-4 linkage containing lignin inspired diaromatic compound to high-value phenolic compounds. Furthermore, coupling sonication to photocatalysis can also improve the selective catalytic activity due to the cavitation phenomenon and better mass transfer.

The key objectives coming from hypothesis 4 are as follows:

- To study the photocatalytic selective conversion of β-O-4 linkage containing lignin-based diaromatic compound to the corresponding high value phenolic compounds.
- To investigate the potential pathway of the formation of the different products from the catalytic cleavage of lignin-based di-aromatic compound without the addition of any oxidizing agent.
- To study the effect of calcination on the crystallinity and photocatalytic performance in order to explore the green synthesis approach.
- To study the reusability and stability of the US-assisted synthesized photocatalyst up to various runs of photocatalytic experiments.
- To study the sonophotocatalytic conversion of lignin-based diaromatic compound.
- To understand the potential mechanism of photocatalytic activity of best performing US-assisted synthesized photocatalyst by identification of the active species.

3. Chapter 3: Methodology

3.1. Materials

The chemicals and materials used were isopropanol (99.7 %, POCH), titanium isopropoxide (98 %, Acros Organics), sodium hydroxide (Chempure), acetonitrile (HPLC grade, POCH), benzyl alcohol (Ph-CH_2OH, 99.5 %, Chempure), 2-phenoxy-1-phenylethanol (PP-ol, 95 %, abcr), benzyl aldehyde (Ph-CHO, 99 %, Chempure), 2-phenoxy-1-phenylethanone (PP-one, 97 %, Sigma Aldrich), phenyl formate (Ph-OCHO, ≥98 %, Sigma Aldrich), phenol (PP-OH) 99 %, Alfa Aesar), 1,4-benzoquinone (BQ, ≥98 %, Sigma Aldrich), potassium iodide (KI, 99 %, Chempur), silver nitrate ($AgNO_3$, 99.8 %, Stanlab), tert-butanol (t-BtOH, ≥98 %, TCI) and commercial TiO_2 (P25, Evonik Degussa). All the chemicals were used as received.

3.2. Synthesis of the catalysts

TiO_2-based samples were synthesized using 20 mL solution of titanium isopropoxide in isopropanol (ratio of 1:3) in a reactor (glass beaker, 250 mL). This solution-containing reactor was irradiated by the US using the cuphorn sonicator of 22 or 40 or 80 kHz (Sinaptec, NexTgen Lab500 generator) or 500 kHz (Sinaptec, NexTgen Lab1000 generator). 100 mL of aqueous solution of sodium hydroxide of 2 M concentration was added to this solution with the flow rate of 1 mL/min under the stabilized temperature at 60 °C using the water-bath and circulating water (ultrabath Julabo DB-5 (Corio CD-B5)). After the complete addition of 100 mL of aqueous solution of sodium hydroxide, the obtained white dispersion was filtered using pre-acidified Whatman filter paper (Carl Roth Gmbh & Co). The obtained residue was washed with dilute hydrochloric acid and milli Q. water until the neutral pH of the filtrate, followed by drying the residue at 90 °C for 16 h in an oven under static air to obtain the solid white powder.

A series of samples were synthesized using different amplitudes of different frequencies of US. The amplitudes such as 10, 30, 50, 70 and 90 µm of 22 kHz, and 30 and 70 µm amplitudes of 40, 80 and 500 kHz sonicators were utilized. The synthesized nanomaterials, referred to as US (frequency in kHz)-(amplitude in µm) representation depending on the used amplitude and frequency, are represented in **Table 3.1**. In order to study the effect of US during the synthesis of

these samples, a sample of TiO_2 was also synthesized using the same method but just replacing the US irradiation with magnetic stirring (200 rpm).

Table 3.1. The detailed of the utilized US and labelling of the synthesized sample

Serial No.	Ultrasonic frequency (kHz)	Amplitude (μm)	Samples labelling
1		10	22kHz-1
2		30	22kHz-3
3	22	50	22kHz-5
4		70	22kHz-7
5		90	22kHz-9
6	40	30	40kHz-3
7		70	40kHz-7
8	80	30	80kHz-3
9		70	80kHz-7
10	500	30	500kHz-3
11		70	500kHz-7
12	Magnetic stirring	200 rpm	MgSt

3.3. Physicochemical characterizations

The synthesized samples were characterized using different techniques. Nitrogen (N_2) adsorption/desorption measurements of all the synthesized samples were performed using Micromeritics instrument (ASAP 2020) at -196 °C in order to study the textural features. Before this measurement, the samples were degassed at 90 °C for 6 h under the vacuum. Brunauer Emmett Teller (BET) approach was used to estimate the specific surface area, while Barret Joyner Halenda (BJH) approach was used to estimate the pore volume [118].

The optical properties of all the synthesized samples and P25 sample were studied by using ultraviolet-visible diffuse reflectance spectroscopy (UV–Vis DRS) using the Jasco V-570 spectrophotometer in the wavelength range of 250-900 nm. The poly(tetra- fluoroethylene) was used to obtain the baseline.

The XRD method by using Siemens D5000 diffractometer equipped with a horizontal goniometer operating at 40 kV and 40 mA was utilized to study the crystallinity of all these samples.

Transmission Electron Microscopy (TEM) (JEOL JEM 2100) of the US assisted synthesized samples by 22, 40 and 80 kHz and MgSt samples were used to study the morphology of these samples. The microscope was operated at 200 kV using the lanthanum hexaboride filament. Whereas the morphological features of samples, which were synthesized with the assistance of different amplitudes of 500 kHz US, the TEM and high angle annular dark field scanning transmission electron microscopy (HAADF-STEM) was carried out using Model Titan Themis 60–300 instrument, which was equipped with a Cs image and probe corrector. Before this measurement, the samples were dispersed in the ethanol by US and then deposited on a 200 mesh carbon grid (Ted Pella Inc.).

Thermal gravimetric analysis (TGA) of all the synthesized samples and P25 sample were performed to study the weight loss by Mettler Toledo TGA/DSC3+ using a thermo-balance.

The surface pH of the synthesized samples and P25 sample was measured by using the using a pH meter (Sevencompact). Before this measurement, 100 mg of the sample was dispersed in 50 mL of Mili Q. water and suspension for 16 h to establish an equilibration under dark conditions [122].

X-ray photoelectron spectroscopic (XPS) analysis of the US-assisted synthesized samples by 22, 40 and 80 kHz, MgSt and P25 samples was performed using PHl 5000 VersaProbe™ Scanning ESCA Microprobe. The XPS spectra for the studied samples were obtained using X-ray source (Al-Kα radiation; hν = 1486.6 eV), which operated at 15 kV, 25 W and 100 μm spot size. Whereas, high resolution XPS spectra were obtained by an analyzer pass energy of 23.5 eV and an energy step size of 0.1 eV. Survey spectra were analyzed using Multipak PHI software, while deconvolution and quantification of the obtained spectra were performed using Casa XPS software (v.2.3, Casa Software Ltd, United Kingdom).

In addition, the surface chemistry of samples synthesized by the assistance of different amplitudes of 500 kHz US, MgSt and P25 samples (for the sake of comparison) was studied by XPS measurements using ESCALAB 50Xi instrument equipped with a monochromatic Al Kα X-ray source. Spectra was obtained using a high-resolution hemispherical analyzer (hν =20 eV) and 200 eV for survey spectra. Avantage (Thermo Fisher Scientific) data processing software was used for the peak fitting, while quantification was performed by sensitivity factors in the avantage library.

Temperature Programmed Desorption (TPD) And Temperature Programmed Oxidation (TPO) of 22kHz-3, MgSt and P25 samples were studied in a tabular quartz flow reactor. The evolved gas was analysed using a mass spectrometer (Dycor Dymaxion) in the range 1-200 m/z. The calcination of these samples (around 20 mg) was performed under the helium (He) (99.9999 %) flow at 100 °C/min for 1 h before the TPD study. However, during the TPD measurement, the samples were heated to 700 °C with a ramp of 10 °C/min under the He flow (flow rate was 25 mL/min). After the TPD measurement, the samples were cooled down to room temperature. Then, these samples were studied for the TPO measurement. The samples were heated up to 700 °C with the ramp of 10 °C/min under the mixed flow of He and the synthetic oxygen (O_2) for Flame Ionization Detector (FID) 2% O_2/(He + N_2) with the controlled flow rate of 25 mL/min.

Energy dispersive X-ray fluorescence analysis (EDXRF) was carried out using MiniPal 4 equipment from PANalytical Co, with a rhodium (Rh) tube and silicon drift detector (resolution 145 eV). EDXRF method was used to gain information on the elemental compositions of samples under investigation.

3.4. Photocatalytic activity tests

Photocatalytic activity of all the synthesized samples and P25 sample was investigated without the addition of any oxidative agent for the conversion of Ph-CH_2OH or PP-ol to the corresponding products under irradiation of UV (365 nm) produced by light emitting diodes (LEDs) (LEDMOD, Omicron, Germany). For the photocatalytic studies, 15 mg of the sample was suspended in the 15 mL of the substrate solution in the acetonitrile in the batch reactor (15 mL) at the temperature 30 °C which was stabilized using water-bath (ultrabath Julabo DB-5 (Corio CD-B5)). The batch photocatalytic setup is presented in S**cheme 3.1.**

Scheme 3.1. Schematic illustration for the utilized setup for the photocatalytic studies. (Represented from the open access article [123])

This suspension was kept homogenous using magnetic stirring. The reactor was covered with aluminum foil to block any possible external light irradiation. Prior to the light irradiation, the suspension was stirred for 1 h to establish the adsorption/desorption equilibration. After the 1 h of stabilization, the suspension was irradiated by the UV light. The sample before and after specific intervals of light irradiation was collected for the analysis, and immediately filtered by using a syringe filter of pore size of 0.20 µm. While the sonophotocatalytic experiments were performed by coupling the US (22 kHz with 30 µm amplitude) to the photocatalytic setup by replacing the magnetic stirring.

To study the effect of calcination on the photocatalytic activity of the selected samples (22kHz-3, MgSt and P25), these selected samples were calcined at 500 °C (with the ramp of 10 °C/min) under static air for 5 h, and the photocatalytic activity was performed as above-mentioned protocol. The reusability of the selected samples (22kHz-3, MgSt and P25) was studied for the investigation of catalytic activity for multiple runs of experiments of these samples for photocatalytic conversion of PP-ol to the corresponding products. After the first and the proceeding runs of the photocatalytic experiment, the decanting of the PP-ol solution, was washed with the water multiple times and then dried at 90 °C for 16 h. This dried sample was used for the next run of photocatalytic

experiment by taking the fresh PP-ol solution. This procedure was continued up to the fifth run of photocatalytic studies.

A series of photocatalytic experiments were performed using various substrates such as 2- PP-one, Ph-OCHO, Ph-OH to understand the potential pathway for the formation of the products from the catalytic conversion of PP-ol.

To identify the major active species which are responsible for the catalytic cleavage of C_α-C_β bond of the PP-ol solution, a series of photocatalytic experiments were performed by the addition of various scavengers such as KI as h^+ scavenger, BQ as super oxide anionic radicals ($O_2^{\bullet-}$) scavenger, t-BtOH as OH radicals and $AgNO_3$ as electrons (e^-) scavenger. The concentration of the scavenger substance per initial concentration of PP-ol substrate was kept equimolar (1:1).

The collected samples from the catalytic studies were analyzed by using the gas chromatograph (GC) (Shimadzu GC-2010) equipped with a FID and the capillary column (Zebron ZB-5MS, Phenomenex USA) of film thickness of 0.5 μm, diameter of 0.25 mm and length of 30 m. He was used as carrier gas. The volume of injected sample was 1 μL and the split ratio was 8:1.

The analysis of samples collected from the photocatalytic experiment of partial selective oxidation of mono-aromatic substrate was performed by maintaining the temperature of the column at 50 °C for 3 min, and increasing up to 300 °C with the ramp of 9 °C/min holding this temperature for 2 min.

The conversion of the monoaromatic substrate such as Ph-CH_2OH, yield and selectivity of the obtained products, and the aromatic balance of the reaction was calculated by the following equations (Eq.):

$$\text{Conversion of substrate } (\%) = \left[\frac{Ci - Cr}{Ci}\right] * 100 \qquad \text{(eq. 3.1)}$$

$$\text{Yield of product } (\%) = \left[\frac{Cp}{Ci}\right] * 100 \qquad \text{(eq. 3.2)}$$

$$\text{Selectivity toward product } (\%) = \left[\frac{Cp}{Ci - Cr}\right] * 100 \qquad \text{(eq. 3.3)}$$

$$\text{Aromatic Balance (\%)} = \left[\frac{Cr+Cp}{Ci}\right] * 100 \qquad \text{(eq. 3.4)}$$

Where Ci is the initial concentration of substrate in mM, while Cr is the concentration of substrate at the specific interval of reaction time, whereas Cp are the concentrations of the product such as Ph-CHO at a selected specific time interval of each photocatalytic reaction [118,124].

To analyze the samples collected from the catalytic conversion of lignin-inspired model diaromatic molecule (PP-ol), the temperature of the column of GC was initially maintained at 40 °C for 3 min and then increased up to 280 °C with the ramp of 10 °C/min, and then increased up to 300 °C with the ramp of 20 °C and hold this final temperature for 5 min.

The following equations were used to calculate the catalytic conversion of substrate, such as PP-ol, , yield of each corresponding product, and aromatic balance of the reaction [125].

$$\text{Conversion of } PP-ol\ (\%) = \left[\frac{\text{Moles of reacted substrate } (PP-ol)}{\text{Moles of initial added substrate } (PP-ol)}\right] * 100 \qquad \text{(eq. 3.5)}$$

$$\text{Yield of } Ph-CHO(\%) = \left[\frac{\text{Moles of formed } Ph-CHO}{\text{Moles of initial added substrate } (PP-ol)}\right] * 100 \qquad \text{(eq. 3.6)}$$

$$\text{Yield of } Ph-OCHO\ (\%) = \left[\frac{\text{Moles of formed } Ph-OCHO}{\text{Moles of initial added substrate } (PP-ol)}\right] * 100 \qquad \text{(eq. 3.7)}$$

$$\text{Yield of } Ph-OH\ (\%) = \left[\frac{\text{Moles of formed } Ph-OH}{\text{Moles of initial added substrate } (PP-ol)}\right] * 100 \qquad \text{(eq. 3.8)}$$

$$\text{Yield of } PP-one(\%) = \left[\frac{\text{Moles of formed } PP-one}{\text{Moles of initial added substrate } (PP-ol)}\right] * 100 \qquad \text{(eq. 3.9)}$$

Aromatic balance (%) =

$$\left[\frac{\begin{array}{c}2\ (\text{Moles of reacted substrate } PP-ol)+\text{Moles of } Ph-CHO \\ +\ \text{Moles of } Ph-ol \\ +\text{Moles of } Ph-OCHO+2(\text{Moles of } pp-one)\end{array}}{2\{\text{Moles of initial added substrate}(PP-ol)\}}\right]*100$$

(eq. 3.10)

4. Chapter 4: Results and discussion

This chapter includes the research work published in Catalysis Communications [123], Ultrasonic Sonochemistry [126] and the research work submitted to the ACS Sustainable Chemistry and Engineering.

4.1. Synthesis of titania samples using ultrasonication at different amplitudes of 22 kHz

Sonochemistry utilizes US to tune the synthesis process for the preparation of nanomaterials by enhancing the reaction rate due to cavitation phenomena [127]. When US wave passes through the liquid, it generates microbubbles, leading to imploding and collapsing, giving rise to acoustic cavitation, high-speed velocity and shock waves. The use of low-frequency US leads to the physical effect of US due to the production of large-size cavitation bubbles, intensifying the mixing effect, better mass transfer and deagglomeration [128]. The amplitude of the ultrasonic waves refers to the strength of the ultrasonic waves, which is represented by the height of the ultrasonic waves. The use of US with the optimized amplitude of the US during the synthesis of nanomaterials leads to altering the physicochemical features as well as catalytic performance. In this chapter, the effects of the different amplitudes (10, 30, 50, 70 and 90 µm) of low frequency (22 kHz) US for the synthesis of TiO_2-based nanomaterials on the physicochemical properties and the photocatalytic performance for the additive-free partial selective oxidation of Ph-CH_2OH to Ph-CHO were presented.

4.1.1. Characterization of 22 kHz US-assisted synthesized samples

XRD method was used to study the crystallographic properties of US-assisted synthesized samples by using different amplitudes of 22 kHz, without US assistance synthesized sample and commercial P25 sample. The XRD patterns of crystallographic structure refinement are presented in **Figure 4.1,** whereas crystalline sizes were calculated based on the Scherer approach and are presented in **Table 4.1**. Anatase and rutile phases were observed for the P25 sample, which was in good agreement with the published literature [129,130]. Whereas all the synthesized samples showed the presence of a predominantly amorphous phase. However, some low-intense peaks appear at 2θ of 25, 45 and 63°, which correspond to the presence of anatase phase [118,131].

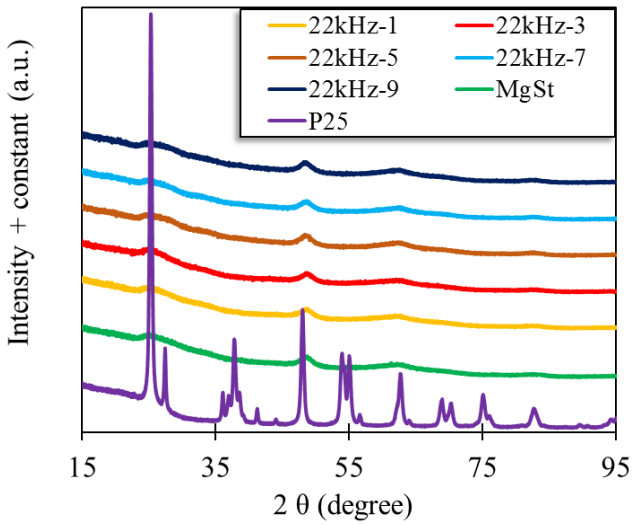

Figure 4.1: XRD patterns of TiO_2 samples synthesized by the US of 22 kHz. (Based on the results of the article submitted to ACS Sustainable Chemistry and Engineering)

Table 4.1. Calculation of crystallite size of TiO_2 samples synthesized by the US of 22kHz, MgSt and P25 samples by the Scherer method. (Based on the results of the article submitted to ACS Sustainable Chemistry and Engineering)

Sample	Dcr Anatase (011) [nm]	Dcr Rutile (110) [nm]
22kHz-1	-	-
22kHz-3	3.1	-
22kHz-5	-	-
22kHz-7	-	-
22kHz-9	-	-
MgSt	-	-
P25	17.3	22.3

The N_2 sorption technique was adopted to explore the textural features of the synthesized and commercial TiO_2 samples. The obtained outcomes are presented in **Table 4.2** and **Figure 4.2**. The utilization of low amplitude US for the synthesis of nanomaterials led to a sample of high porosity compared to the sample synthesized using the high amplitude of US. The 22kHz-3 sample showed the highest specific surface area (319 m^2/g) compared to all other US-assisted synthesized samples, MgSt sample and P25 sample. A similar trend was observed in the case of pore volume. The highest pore volume was presented by 22kHz-3 sample (0.34 cm^3/g) followed by 22kHz-1 sample (0.19 cm^3/g) and 22kHz-7 sample (0.15 cm^3/g), whereas 22kHz-5, P25 and MgSt samples showed pore volume 0.14 cm^3/g, 0.14 cm^3/g and 0.13 cm^3/g, respectively.

Tables 4.2. Textural, surface pH and optical parameters of TiO_2 samples synthesized by the US of 22kHz and MgSt samples. (Based on the results of the article submitted to ACS Sustainable Chemistry and Engineering)

Index number	Material	Specific surface area (m^2/g)	Pore volume V_p (cm^3/g)	Estimated band gap (eV)	Surface pH
1	22kHz -1	155	0.19	3.45	8.2
2	22kHz-3	319	0.34	3.32	7.3
3	22kHz-5	108	0.14	3.49	8.4
4	22kHz-7	109	0.15	3.45	8.5
5	22kHz-9	82	0.12	3.44	8.6
6	MgSt	124	0.13	3.45	8.1
7	P25	46	0.14	3.21	6.3

The higher porosity of the low amplitude US-assisted synthesized samples and MgSt sample can be attributed to the presence of higher OH groups on the surface of samples [123,126], which are presented in later parts. The isotherms obtained from N_2 sorption measurements revealed that US-assisted synthesized samples by using low amplitudes such as 22kHz-1 and 22kHz-3 possessed the complex isotherms that revealed that these samples contained microporous and mesoporous features (**Figure 4.2a**). Whereas, US-assisted synthesized samples using high amplitudes such as 22kHz-5, 22kHz-7 and 22kHz-9 samples possessed isotherms more closely similar to type I (b) and type II isotherms [123,132]. These outcomes revealed that the microporous features are present in the 1.6-2 nm range, whereas mesoporous features are in the 2.5 - 9.5 nm range. The outcome of pore-size distribution is also supported the microporous and mesoporous features (**Figure 4.2b**).

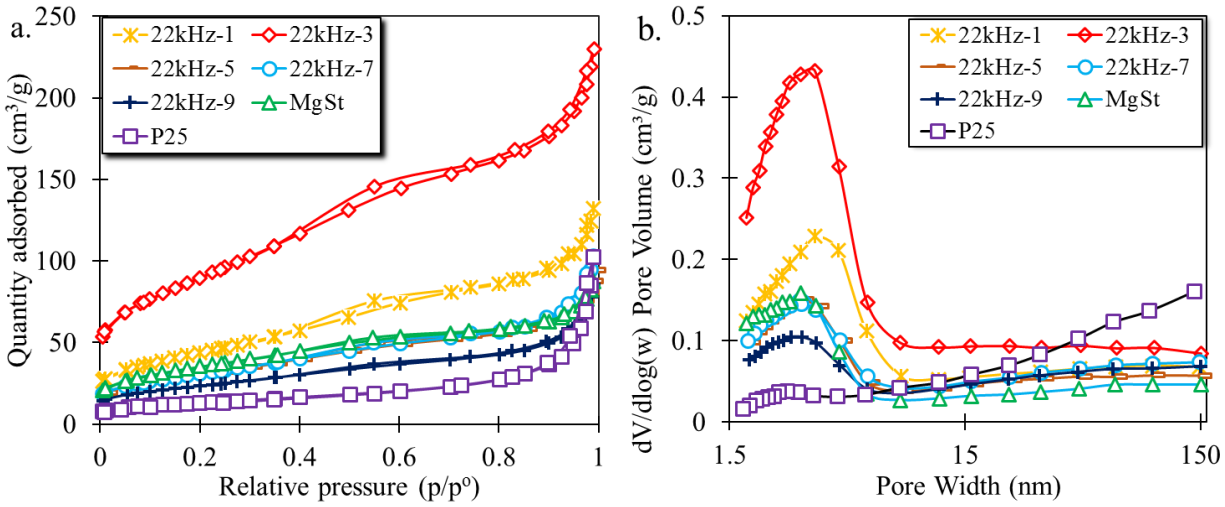

Figure 4.2. N_2 adsorption-desorption isotherms (a), and the pore size distribution (b) of TiO_2 samples synthesized by the US of 22 kHz, MgSt and P25 samples. (Based on the results of the article submitted to ACS Sustainable Chemistry and Engineering)

The weight loss of the commercial P25 sample and all the synthesized samples was estimated by the TGA. A low weight loss (≤ 2.5 %) was observed by P25 sample till the heating at 400 °C, whereas all the synthesized samples showed weight loss higher than 13 %, as described in **Figure 4.3a.** The higher weight loss shown by the synthesized samples suggested that these samples contained elevated amounts of OH radicals, which may be due to the low temperature (90 °C) of the drying step during the synthesis of these samples. Another factor is that these synthesized samples contain a more porous character compared to commercial P25 sample, and the porous

character can absorb higher water moieties [70]. P25 sample showed the least weight loss compared to all the synthesized samples, which is due to synthesis at a higher temperature during the pyrolysis, and this low weight loss suggested a comparatively lower amount of OH groups or water moieties than the synthesized samples. One of the key objectives of the research work was to avoid any energy-demanding step, such as calcination at a higher temperature, for the synthesis of these samples in order to adopt a greener synthesis approach. These pre-adsorbed water moieties might be helpful for the formation of the reactive oxygen species, which can facilitate the catalytic process.

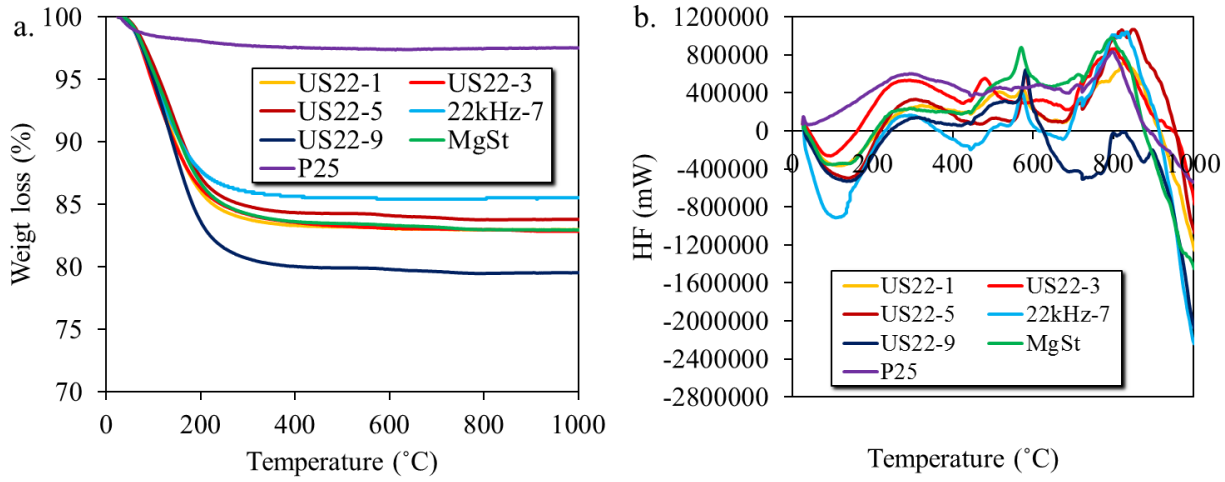

Figure 4.3. Thermograms (a), and differential scanning calorimetry (b) of TiO_2 samples synthesized by the US of 22kHz, MgSt and P25 samples. (Based on the results of the article submitted to ACS Sustainable Chemistry and Engineering)

The phase transformation upon continuous thermal exposure of all the samples from room temperature to 1000 °C was studied by differential scanning calorimetry (DSC). Different phase transformations for P25 and all the synthesized samples were observed with the gradually increased temperature (**Figure 4.3b**). The DSC measurement of all the synthesized samples up to 200 °C corresponds to the endothermic process based on the heat flow (HF), which might be due to the removal or evaporation of water contents [133]. Whereas, in the case of P25 sample, this endothermic process was not observed. The temperature ranges from 200 °C to 450 °C, and all the synthesized and P25 samples showed a different trend of DSC outcome corresponding to an exothermic process, which suggests the removal of other possible organic moieties from the

samples [134]. In the temperature range from 450 °C to 600 °C, the observed peaks suggested the transformation of the amorphous to anatase phase [135], whereas peaks appeared in the temperature range of 600 °C to 900 °C indicate the transformation of anatase to rutile phase [136].

TPD measurements of the selected samples, such as 22kHz-3, MgSt and P25 samples, was also performed, and the derived outcomes are presented in **Figure 4.4a-c**. The results of TPD measurements showed that the 22kHz-3 and MgSt samples showed higher amounts of water moieties on the surface of the samples than the P25, which are in good agreement with the thermal analysis. After the TPD measurement, the samples were used to study the TPO and the derived outcome is presented in **Figure 4.4d.** The results of TPO measurements showed that the 22kHz-3 and MgSt samples revealed the elution of carbon dioxide (CO_2), while in the case of P25 sample, no elution of CO_2 was observed, which indicates that these 22kHz-3 and MgSt samples contained the carbonaceous species on their surface.

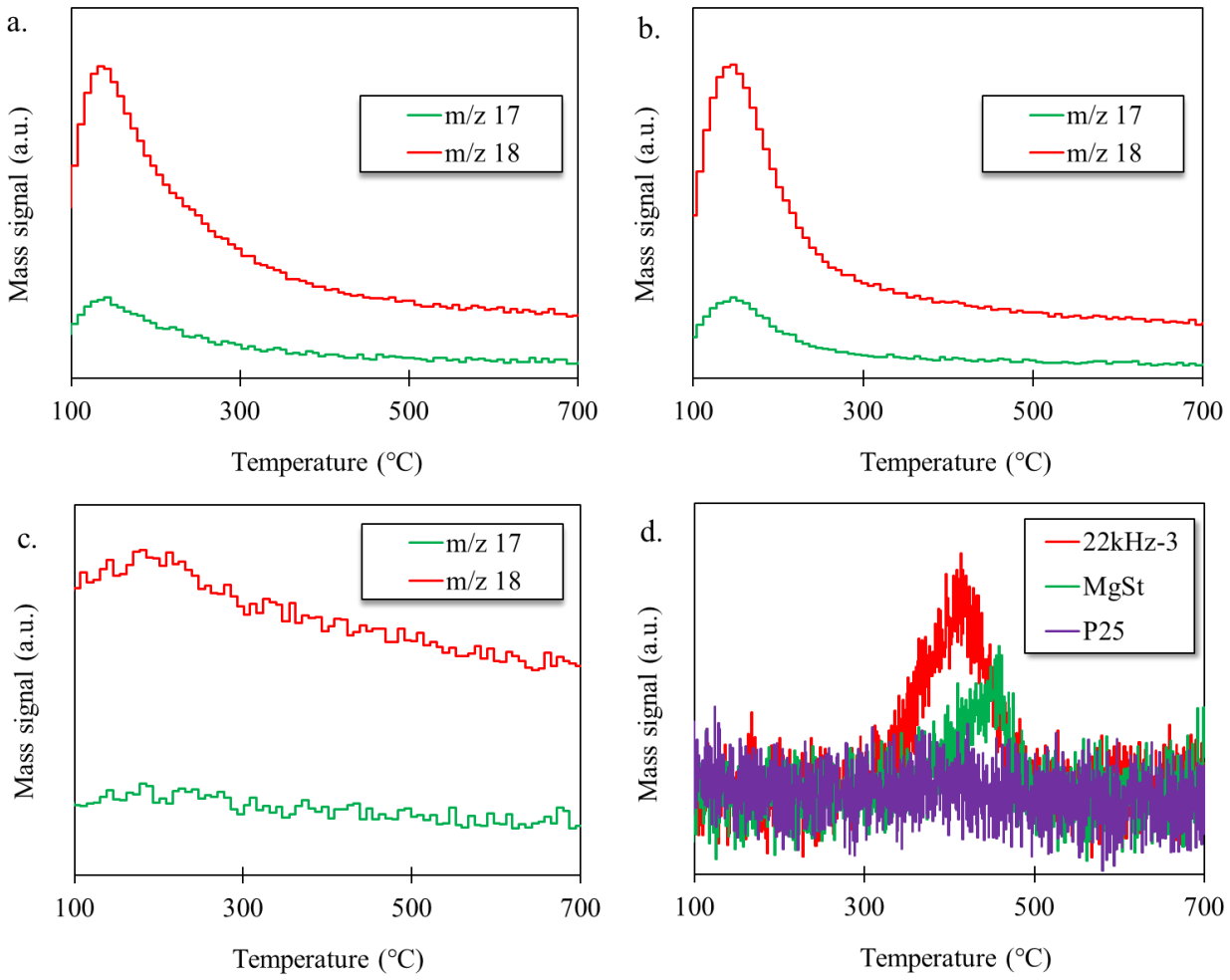

Figure 4.4. Temperature program desorption in range 1–100 m/z of 22kHz-3 (a), MgSt (b), P25 (c); temperature program oxidation of samples after temperature program desorption for m/z 44 (CO_2) samples after temperature program desorption. (Based on the results of the article submitted to ACS Sustainable Chemistry and Engineering)

The UV-Vis DRS technique was used to explore the optical properties of all the 22 kHz US-assisted synthesized MgSt and P25 samples in the range of 250–900 nm, and the derived outcomes are presented in **Figure 4.5**. All the synthesized samples showed absorption in less than 400 nm, while the P25 sample showed absorption in the broader ultraviolet-visible range and less than 450 nm (**Figure 4.5a**). These outcomes showed that photocatalytic experiments can be only possible under the irradiation of UV light.

The bandgaps of all these samples were estimated Tauc plots based on the Kubelka–Munk theory function [137], which revealed that P25 sample showed 3.2 eV, whereas all the synthesized samples showed higher bandgaps compared to P25 sample (**Figure 4.5b**). 22kHz-3 sample showed the lowest bandgap (3.32 eV) than all the synthesized samples.

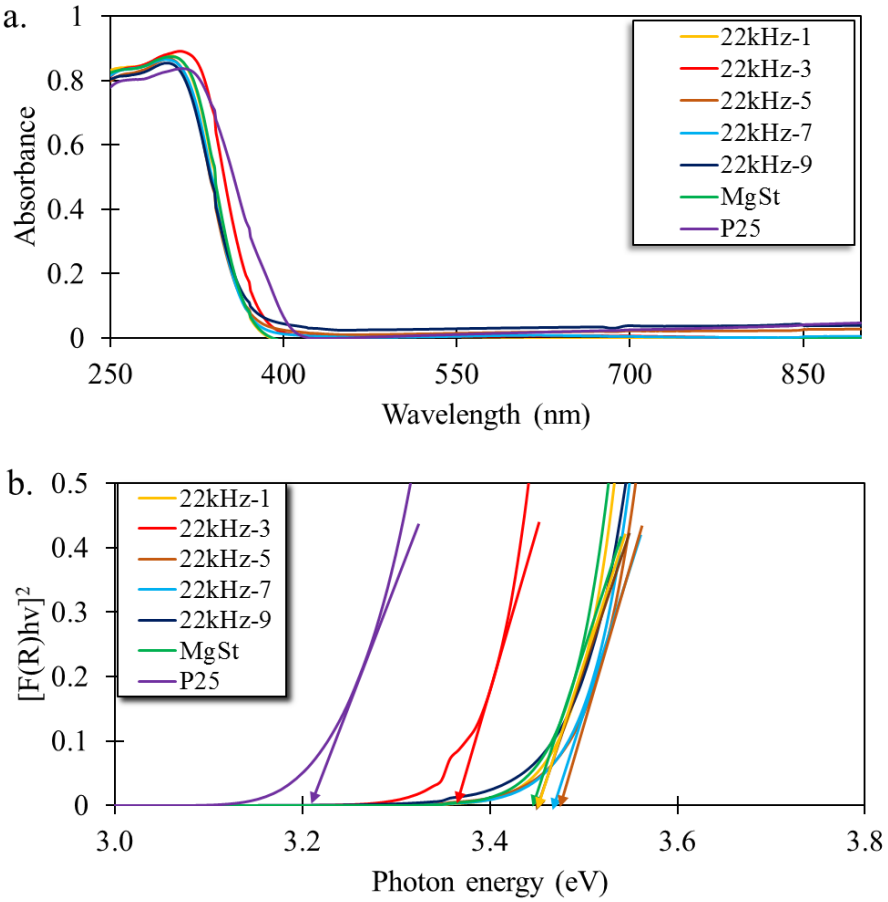

Figure 4.5. UV–Vis DRS spectra (a) Tauc plots (b) of TiO_2 samples synthesized by the US of 22kHz, MgSt and P25 samples. (Based on the results of the article submitted to ACS Sustainable Chemistry and Engineering)

The morphological features of US-assisted synthesized samples and MgSt sample were studied by TEM, and the TEM images are collected in **Figure 4.6.** The first outcome of the morphological studies was that the utilization of US for synthesizing TiO_2-based samples resulted in the formation of the 1-dimensional nanostructure, which resembles the appearance of nanorods compared to synthesized samples without the utilization of US. Another outcome is that the amplitude of the

utilized US is a crucial parameter in tuning the obtained nanostructures. The increasing utilized amplitude led to an increasing trend in the length of the formed nanorods-like structure. The sample synthesized using a low amplitude of US such as 22kHz-3 sample, showed a nanorods like structure in the length range of 15-45 nm, whereas the samples synthesized by using a high amplitude of US such as 22kHz-9 sample showed the nanorods in the length range of 30-70 nm. Furthermore, the arrangement of these nanorods-like structures results in the formation of the cobweb structure. While the sample synthesized without the irradiation of US showed a totally different morphology, as it showed the formation of spherical shape nanoparticles of size 2-10 nm.

XPS technique was used to study the surface chemistry of all the US-assisted synthesized samples along with MgSt and P25 samples. The observed atomic percentages of O 1s, C 1s, Ti 2p and Na 2p for these samples were presented in **Table 4.3**, while the high-resolution deconvolutions spectra were presented in **Figure 4.7-8**. The outcome of XPS studies revealed that the three peaks that appear at 284.5-284.9 eV, 286.1-286.9 eV and 288.5–289.9 eV were obtained from the high-resolution deconvolution spectra of C 1s, indicating the adventitious carbon C-C, epoxide C-O-C and carboxyl (O-C=O) functional groups, respectively [138,139]. While two peaks in the range of 529.9-531.1 eV and 531.5-532.2 eV were observed from the high energy core resolution deconvolutions spectra of O 1s, indicating the presence of bridging oxygen (Ti-O-Ti) of the metallic oxide and surface OH groups, respectively for all the herein studies samples [138,140]. In the case of high-resolution deconvolutions spectra of Ti 2p, two doublet peaks at 459.18 eV and 464.88 eV, which correspond to Ti 2p 3/2 and Ti 2p 1/2, respectively for all the samples [140,141]. An additional peak at 31.53 eV was observed for all the herein studies samples except the P25 sample, which showed the presence of sodium on the surface. The sodium was observed only in the case of the synthesized samples, which may be due to the aqueous sodium hydroxide solution utilization during the synthesis step.

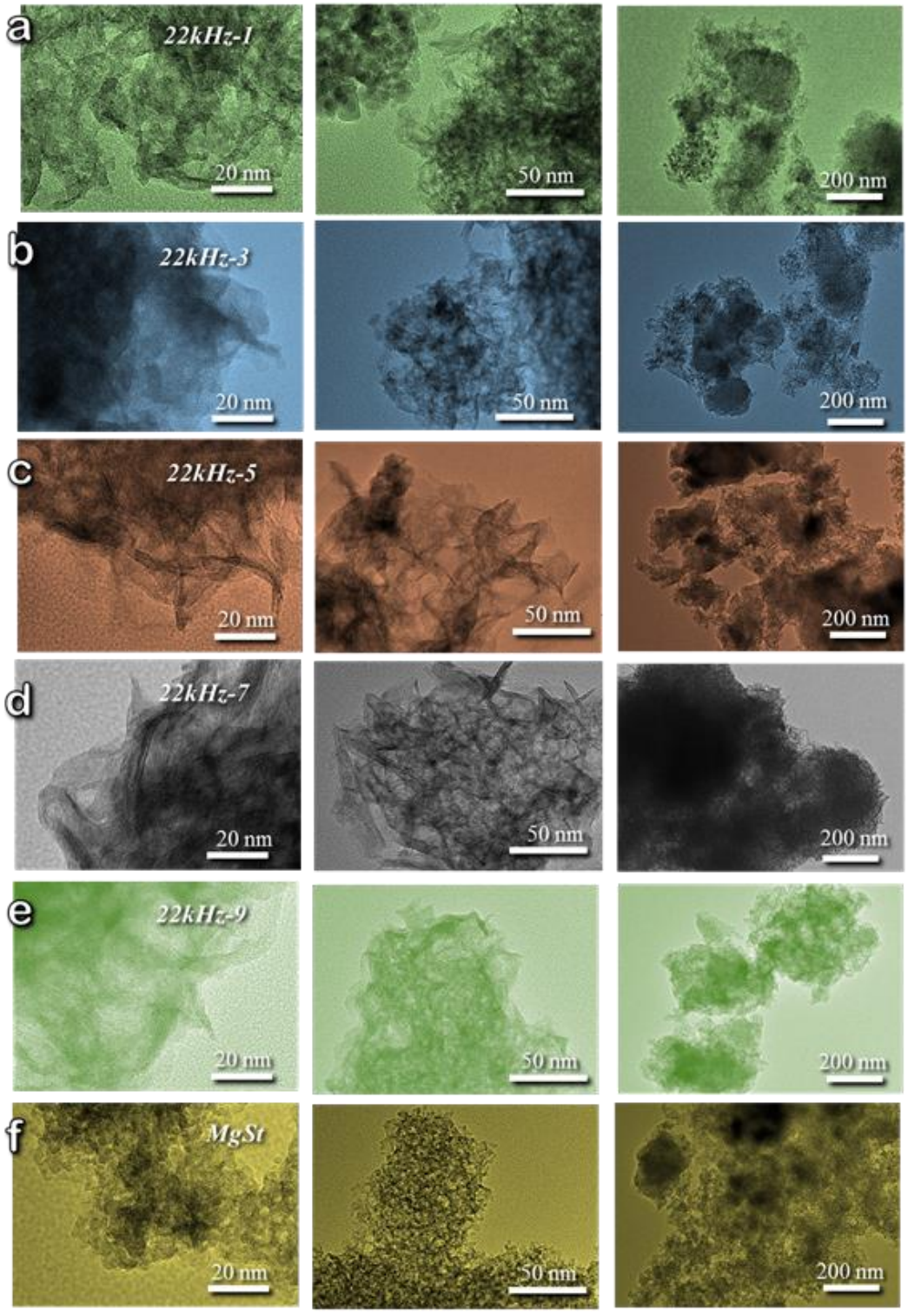

Figure 4.6. TEM images of TiO_2 samples synthesized by the US of 22kHz and MgSt sample. (Based on the results of the article submitted to ACS Sustainable Chemistry and Engineering)

Table 4.3. The atomic percentages of O1s, C 1s, Ti 2p and Na 2p for synthesized and commercial P25 samples. (Based on the results of the article submitted to ACS Sustainable Chemistry and Engineering)

Sample	C 1s (C-C) 284.8 eV	C1s (C-O-C) 286.17 eV	C 1s (COOH/ COOR) 289.58 eV	O1s (Ti-O-Ti) 530.72 eV	O1s (C=O) 531.99 eV	Ti 2p 3/2 459.18 eV	Ti 2p 1/2 464.88 eV	Na 2p 31.53 eV
22kHz-1	2.26	0.72	0.7	54.8	7.6	16.72	8.35	8.85
22kHz-3	2.32	0.8	0.65	59.06	5.99	17.91	8.95	4.32
22kHz-5	3.34	0.45	0.67	55.63	4.15	16.24	8.11	11.41
22kHz-7	2	0.29	0.54	57.7	4.43	16.55	8.27	10.22
22kHz-9	2.53	0.43	0.67	56.5	4.14	16.04	8.02	11.67
MgSt	2.66	0.45	0.85	57.75	4.08	16.26	8.12	9.83
P25	8.76	1.08	1.18	58.84	4.38	17.18	8.58	---

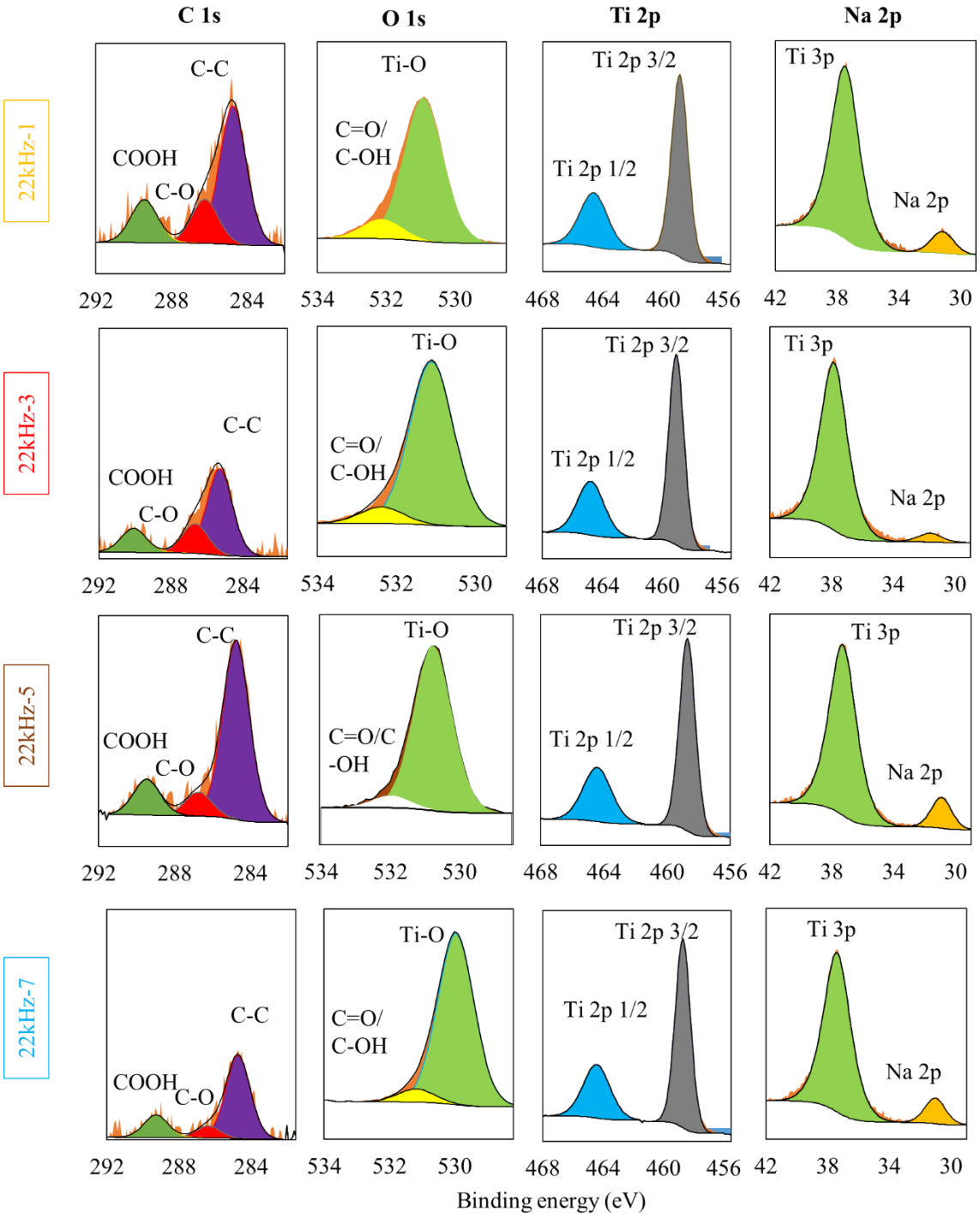

Figure 4.7. High-resolution core energy spectra for the 22kHz-1, 22kHz-3, 22kHz-5 and 22kHz-7 samples. (Based on the results of the article submitted to ACS Sustainable Chemistry and Engineering)

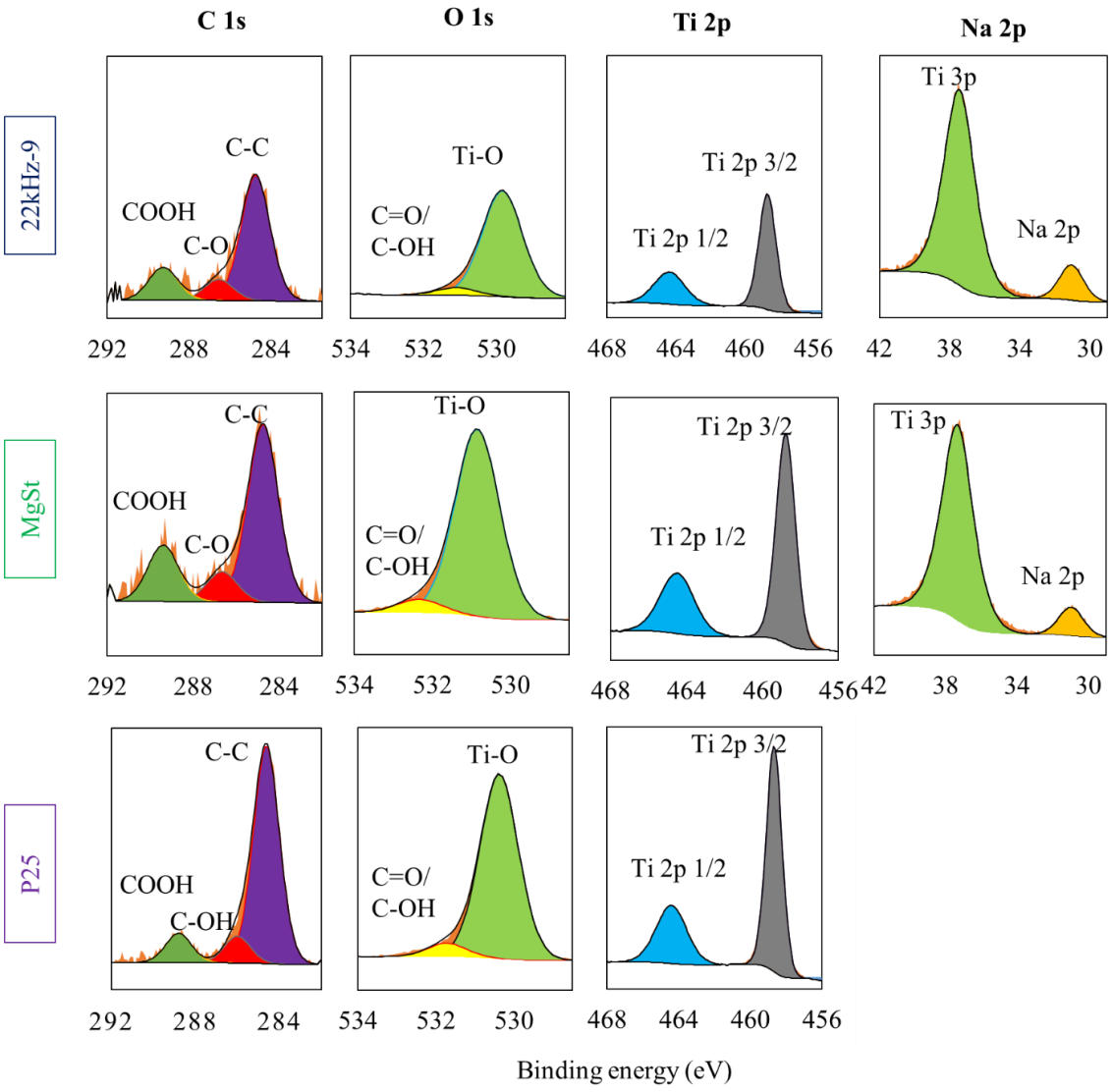

Figure 4.8. High-resolution core energy spectra for the 22kHz-9, MgSt and P25 samples. (Based on the results of the article submitted to ACS Sustainable Chemistry and Engineering)

4.1.2. Photocatalytic studies of 22 kHz of US-assisted synthesized samples for partial selective oxidation of Ph-CH_2OH to Ph-CHO

The additive-free photocatalytic activity of 22 kHz US-assisted synthesized samples along with MgSt and P25 samples were studied for the selective oxidation of Ph-CH_2OH to Ph-CHO. The commercial P25 sample is well-known photocatalyst for the higher conversion of organic pollutant compounds, but this conversion was found to be very unselective to the targeted products, leading to the mineralization of the organic compounds [125,142]. For the synthesis of high-value

compounds, the selectivity and the yield of the targeted products are the key parameters to be obtained. The results of the photocatalytic activity of P25 sample showed higher and faster conversion of Ph-CH_2OH as compared to the synthesized samples, but the yield and selectivity toward the Ph-CHO were observed lowered [123,126]. After 6 h of UV light irradiation, P25 sample showed 95.5 % conversion of Ph-CH_2OH to 34.9 % yield of Ph-CHO with 36.5 % selectivity toward Ph-CHO and 38.3 % aromatic balance **(Figure 4.9)**. One of the key objectives of this doctoral thesis is the synthesized TiO_2-based sample, which revealed the higher selective conversion of aromatic alcohol to the corresponding aldehyde. US-assisted synthesized TiO_2-based catalysts using different amplitudes revealed a wide-ranging deviation of photocatalytic partial selective oxidation results. The samples synthesized using low amplitudes of 22 kHz US showed higher photocatalytic selective oxidation of Ph-CH_2OH to Ph-CHO than the samples synthesized using high amplitudes of 22 kHz US. The 22kHz-3 sample observed the higher and faster conversion of Ph-CH_2OH among all the synthesized samples, which showed 75.5 % conversion of Ph-CH_2OH after 6 h of UV light irradiation to the 67.1 % yield of Ph-CHO with 88.8 % selectivity and 92.1 % aromatic balance. Whereas the second higher photocatalytic results were shown by the 22kHz-1 sample, which showed 51.7 % conversion of Ph-CH_2OH to the 50.1 % yield of Ph-CHO with 96.8 % selectivity and 98.3 % aromatic balance after 6 h of UV light irradiation. Whereas the samples synthesized using high amplitudes of 22 kHz US showed the lower conversion of Ph-CH_2OH to Ph-CHO. While, the MgSt sample which prepared under silent conditions without US assistance showed lower photocatalytic performance than sample prepared with the low amplitudes of 22 kHz US. MgSt sample showed 30.5 % conversion of Ph-CH_2OH to the 29.6 % yield of Ph-CHO with 96.8 % selectivity and 98.5 % aromatic balance after 6 h of UV light irradiation.

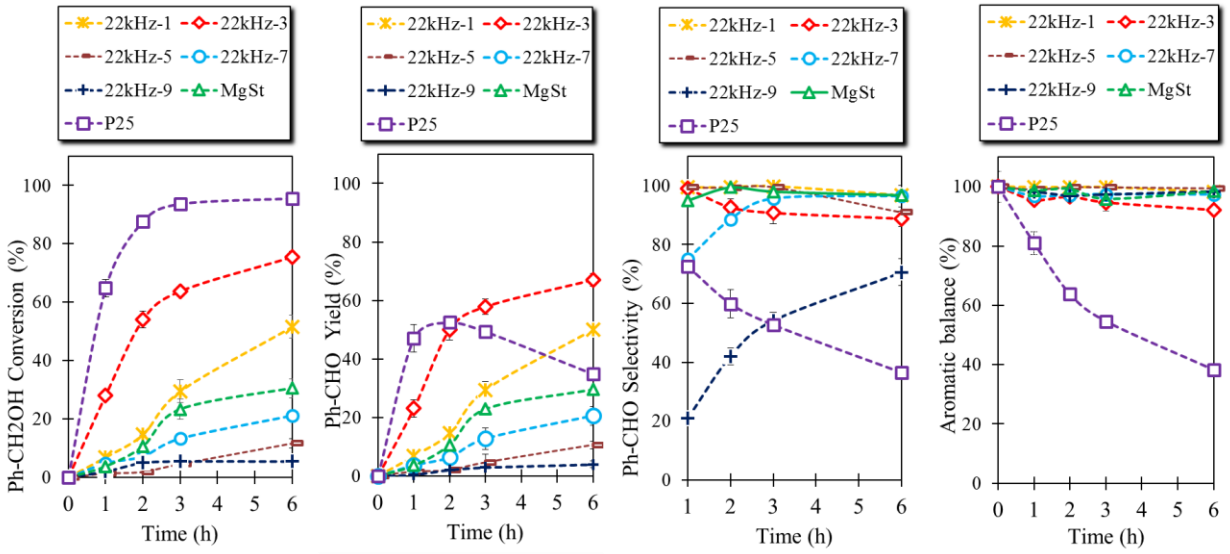

Figure 4.9. Photocatalytic activity of TiO_2 samples synthesized by the US of 22 kHz, MgSt and P25 samples. (Based on the results of the article submitted to ACS Sustainable Chemistry and Engineering)

The discussion of these obtained results from the commercial P25, which showed higher and faster conversion of Ph-CH_2OH compared to all the synthesized samples with US assistance (22 kHz with different amplitudes) and without US assistance. The increasing trend in the conversion of Ph-CH_2OH was observed, but with a decreasing trend in the selectivity toward the Ph-CHO with the increase in the duration of light irradiation, resulting in the lowering of aromatic balance. The used analytics, such as GC column, are dedicated to analysing the aromatic compounds, and no other aromatic compound, such as benzoic acid was detected.

Due to many possible factors, the higher catalytic selective conversion of lignin-inspired model molecule by using 22kHz-3 samples to the targeted products such as Ph-CHO. The US-assisted synthesised nanomaterials possessed the most favourable textural properties, such as higher specific surface area and pore size distribution of nanomaterials. The enhanced textural properties, as well as the morphology of the US-assisted sample, especially the observation of interlayer spacing, is also a crucial aspect that helps improve the absorption of the lignin-inspired model compounds and enhances the light penetration inside the samples. Another, the surface heterogeneity of the US-assisted nanomaterials showed the existence of the basic medium, which confirms the blockage of acidic groups on the surface. The XPS analysis's surface composition of

the US-assisted samples also revealed the presence of sodium on the surface, which enhanced the surface's basicity. The higher oxygen species corresponding to C=O on the surface of 22kHz-3 sample, as described by XPS analysis, also suggested that the C=O functional group may lead to the photosensitizer effect, which improved the light penetration [143]. As XRD analysis described, the 22kHz-3 sample possessed a predominantly amorphous phase with a small-size anatase crystal phase, which also improved the catalytic activity compared to a well-defined crystal phase [144]. Also, elevated OH radicals formation revealed by the thermal analysis improves the catalytic activity [145].

4.1.3. Conclusions of section 4.1

The synthesis of novel catalysts by the green approach, such as US, avoids the energy-demanding step in order to prepare the proper catalysts for the targeted goal. The utilization of low-frequency US with lower amplitude led to the synthesis of nanostructure with the elevated specific surface area and pore size distribution compared to high amplitude US-assisted synthesized samples, non-US assisted synthesized samples and commercial P25 sample. All the TiO_2 samples showed a predominantly amorphous structure. The sample synthesized using 30 µm of 22 kHz US (22kHz-3) showed the highest yield of Ph-CHO from the photo-catalytic oxidation of Ph-CH_2OH without the addition of any oxidative reagent compared to all other US-assisted synthesized samples. Whereas the utilization of a higher amplitude of US of 22 kHz showed a lower yield of Ph-CHO. These results suggested that the optimization of the amplitude of the utilized frequency of US for the synthesis of the catalyst is ultimately important to tune the physiochemical properties as well as the photocatalytic selective oxidation performance.

4.2. Synthesis of TiO_2 samples with the assistance of US of 22, 40 and 80 kHz

As the 22kHz-3 sample showed higher photocatalytic selective oxidation of Ph-CH_2OH to the Ph-CHO, the 30 µm amplitude of 22 kHz was considered the optimized US amplitude for the nanomaterial's synthesis. More TiO_2-based samples were synthesized using 40 and 80 kHz US in the range of physical effect of US with 30 µm as well 70 µm in order to study the effect of higher amplitude of utilized US. All these synthesized samples were compared with the 22kHz-3 and 22kHz-7 samples as well as MgSt and P25 samples, in terms of characterization and the photocatalytic oxidation performance.

4.2.1. Characterization of TiO_2 samples synthesized with the assistance of US of 22, 40 and 80 kHz

The crystallographic nature of all the herein-studied samples was studied by the powder XRD. The obtained XRD patterns are collected in **Figure 4.10**. The first outcome from the XRD studies is that all the synthesized samples are predominately contained amorphous structures. However, the appearance of some peaks at the 2θ of 25, 47 and 63° corresponds to the presence of anatase characteristics.

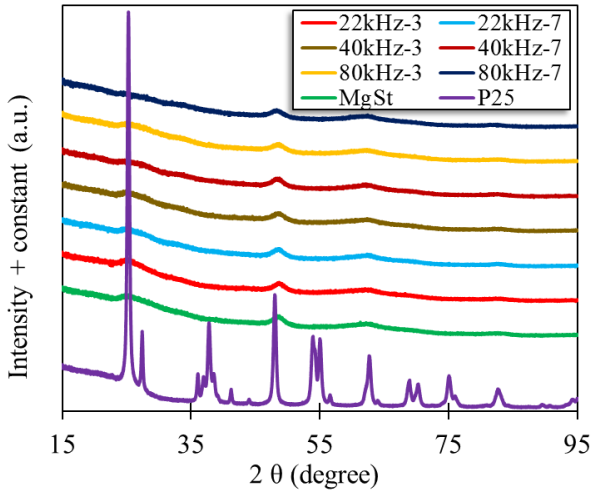

Figure 4.10. XRD patterns of TiO_2 samples synthesized by the US of 22, 40 and 80 kHz, MgSt and P25 samples. (Based on the results of the article submitted to ACS Sustainable Chemistry and Engineering and the published open-access article [126])

The textural properties of all the synthesized and P25 samples were studied by the N_2 sorption method, and the obtained outcomes are collected in **Figure 4.11** and **Table 4.4.** The key outcome is the utilization of a low amplitude of US during the synthesis step led to the formation of more porous samples compared to the utilized high amplitude of US. Another outcome is that the increment of the utilized frequency from low to high US with the same amplitude, either low or high, has a negative impact on the textural features of the synthesized samples. The sample synthesized using low amplitude (30 µm) of low frequency 22 kHz named 22kHz-3 showed the elevated textural properties such as specific surface area (319 m^2/g) and pore volume (0.34 cm^3/g), which was found more than two times of all the US assisted samples as well as MgSt sample.

The low amplitude of US-assisted synthesized samples, such as 40kHz-3 and 80kHz-3 showed a specific surface area of 141 and 131 m^2/g and pore volume 0.21 and 0.16 cm^3/g, respectively. Whereas the samples synthesized using higher amplitude (70 µm) of 22, 40 and 80 kHz showed a lower specific surface area and pore volume with a similar trend as observed in the case of low amplitude of US-assisted synthesized samples. Whereas, MgSt and P25 samples showed a specific surface area of 124 and 46 m^2/g and pore volume of 0.13 and 0.14 cm^3/g, respectively.

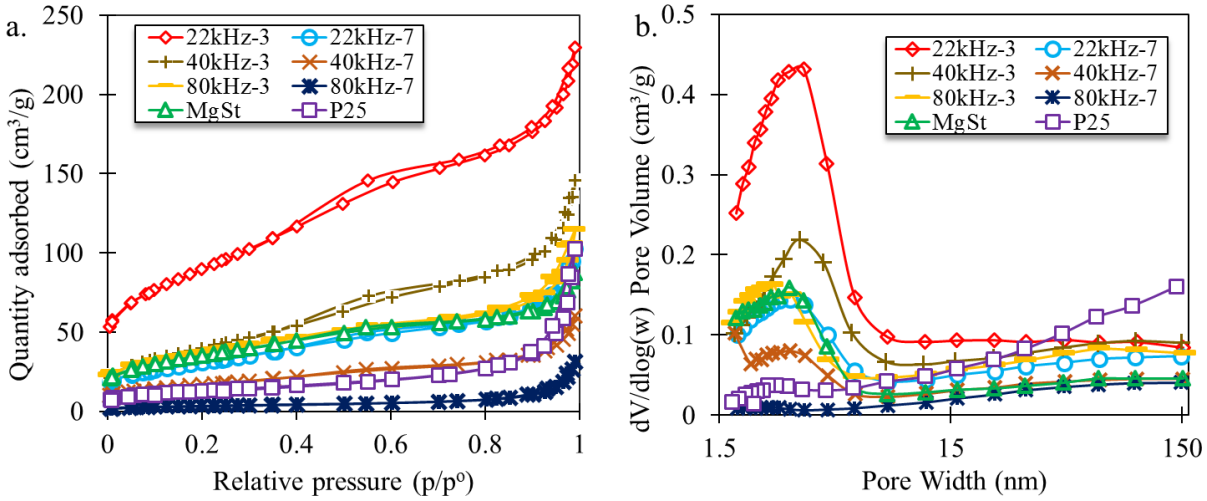

Figure 4.11. N_2 adsorption-desorption isotherms (a), and the pore size distribution (b) of TiO_2 samples synthesized by the US of 22, 40 and 80 kHz, MgSt and P25 samples. (Based on the results of the article submitted to ACS Sustainable Chemistry and Engineering and the published open-access article [126])

The obtained isotherms (**Figure 4.11a**) of the 22kHz-3 and 40kHz-3 samples showed a complex shape, which indicates that mesoporous and microporous properties are present. In the case of all other samples, the obtained isotherms are closed to type I(b) and II [132], indicating that these samples possessed the microspores feature in the range 1.6 to 2 nm and mesoporous in the range 2.5 to 9.5 nm, which can be observed in the pore size curve (**Figure 4.11b**). These results suggested that the optimization of the utilized frequency and amplitude during the synthesis is necessary for the synthesis of novel nanomaterials with tuned textural features.

Tables 4.4. Textural and optical parameters of titania samples synthesized by the US of 22, 40 and 80 kHz, MgSt and P25 samples. (Based on the results of the article submitted to ACS Sustainable Chemistry and Engineering and the published open-access article [126])

Index number	Material	Specific surface area (m^2/g)	Pore volume V_p (cm^3/g)	Estimated band gap (eV)	Surface pH
1	22kHz-3	319	0.34	3.32	7.3
2	22kHz-7	109	0.15	3.47	8.4
3	40kHz-3	141	0.21	3.44	7.9
4	40kHz-7	60	0.09	3.57	8.5
5	80kHz-3	131	0.16	3.52	8.3
6	80kHz-7	12	0.04	3.56	8.9
7	MgSt	124	0.13	3.45	8.1
8	P25	46	0.14	3.21	6.3

TGA of all the herein samples were investigated in order to study the loss in weight upon the increment of temperature. The P25 sample showed the least weight loss which was observed ~2.4 % up to 400 °C (**Figure 4.12a**). Whereas, all the synthesized samples showed higher weight loss with the same increment in temperature up to 400 °C. The samples 22kHz-7 and 40kHz-7 showed 13 % weight loss, while the samples 22kHz-3, 40kHz-3 and MgSt showed around 16 % weight loss. Whereas both samples synthesized with the assistance of 80 kHz US showed higher weight loss, 80kHz-3 showed 20 % weight loss, and 80kHz-7 sample showed 23 % weight loss till 400 °C, but 80kHz-7 sample also showed more weight loss 23 – 25.5 % in the range of 500 to 800 °C.

The higher weight loss shown by the synthesized samples suggested that these samples contained OH groups or water moieties.

DSC of all the herein samples was also performed in order to study the phase transformation of the samples. The different peaks of DSC studies were observed in the increment of temperature (**Figure 4.12b**). The appearance of the first peak was observed in the temperature range of 0-200 °C for the synthesized samples that correspond to the endothermic process and also suggested the removal of water [146,147]. But in the case of P25 sample, this peak was not observed. Another peak was observed in the temperature range of 200-450 °C for the synthesized and P25 samples, suggesting the exothermic process and removal of some possible organic residues from the samples [148,149]. The peak in the temperature range of 450-700 °C also showed exothermic and suggested the transformation of amorphous to anatase crystalline phase. Whereas the peak in the temperature range of 700-900 °C suggested the phase transformation of anatase to rutile [150].

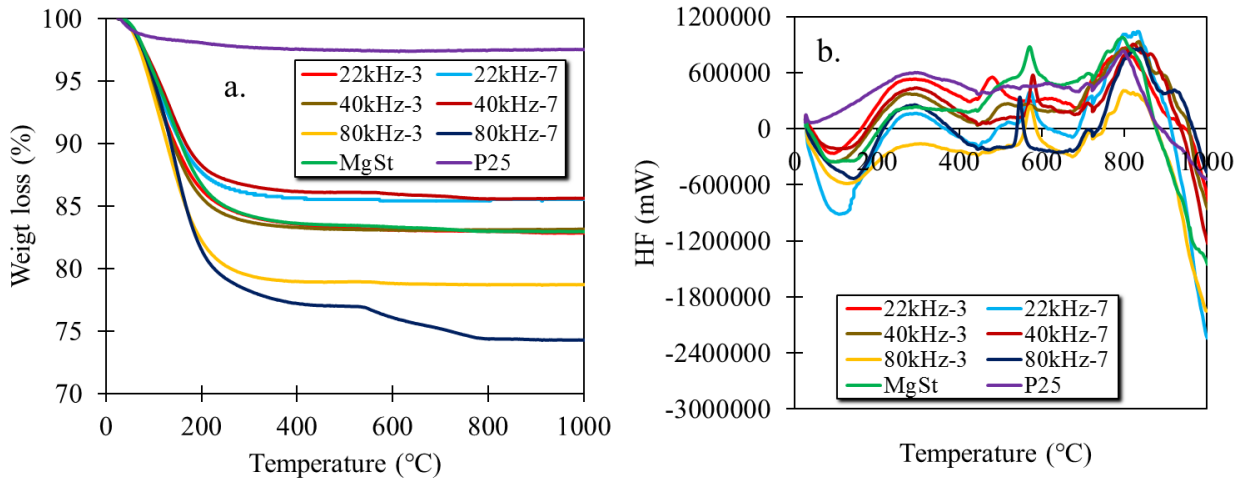

Figure 4.12. Thermograms (a), and differential scanning calorimetery (b) of TiO_2 samples synthesized by the US of 22, 40 and 80 kHz, MgSt and P25 samples. (Based on the results of the article submitted to ACS Sustainable Chemistry and Engineering and the published open-access article [126])

UV-Vis DRS of all the herein samples was performed in order to study the optical properties of the sample. The obtained absorption spectra were presented in **Figure 4.13a**, which suggested that all the synthesized samples showed light absorption in the range of 300-390 nm, whereas the P25

sample showed absorption in a slightly longer wavelength (370-410 nm). Tauc plots method based on the Kubelka–Munk function was utilized to estimate the bandgaps [153,154], and the bandgap was presented in **Table 4.4**.

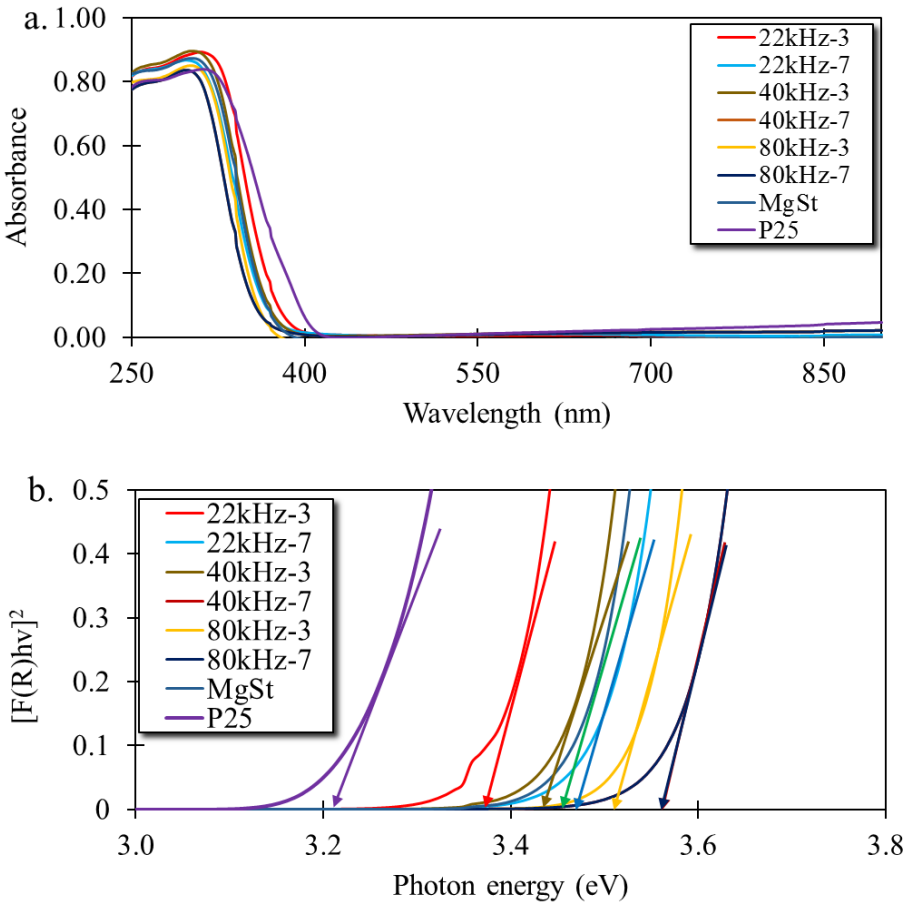

Figure 4.13. UV–Vis DRS spectra (a) Tauc plots (b) of TiO_2 samples synthesized by the US of 22, 40 and 80 kHz, MgSt and P25 samples. (Based on the results of the article submitted to ACS Sustainable Chemistry and Engineering and the published open-access article [126])

The P25 sample showed bandgaps of 3.21 eV, whereas all the synthesized samples showed slightly higher bandgap in the 3.32 to 3.58 eV range. The samples synthesized using the low amplitude (30 µm) of 22 kHz showed the lowest band gap amount among the synthesized samples (**Figure 4.13b**). Another outcome is that the utilization of low amplitude US, regardless of frequency, showed a lower bandgap compared to the high amplitude, which also supported the finding described in **Section 4.1** that the utilization of low amplitude led to a lower bandgap.

The altered textural and thermal properties of the herein-studied samples indicate that the utilization of US of different frequencies of low and high amplitude plays a key role in tuning the characteristics of the synthesized sample. The morphological feature of herein-studied samples was also investigated by TEM in order to examine the effect of US of different frequencies on the morphology of synthesized samples, and the obtained TEM images are presented in **Figure 4.14**. The first observed outcome is that all the US-assisted samples form a 1-dimensional nanostructure, which agrees with XRD results. The sample synthesized using a low amplitude of 22 kHz revealed the most distinguishing nanomaterials showing better morphology, which look like nanorods with a length in the range of 20-60 nm compared to the samples synthesized using a high amplitude (**Figure 4.14a,b**). The samples synthesized using the low and high amplitude of the 40 and 80 kHz frequencies did not show more specific morphology **(Figure 4.14c-f**). Another outcome from the TEM images is that the MgSt sample, which was synthesized without the assistance of US, showed the formation of spherical-shaped nanoparticles of small-sized (2-10 nm) instead of the formation of 1-dimensional nanomaterials (**Figure 4.6f)**.

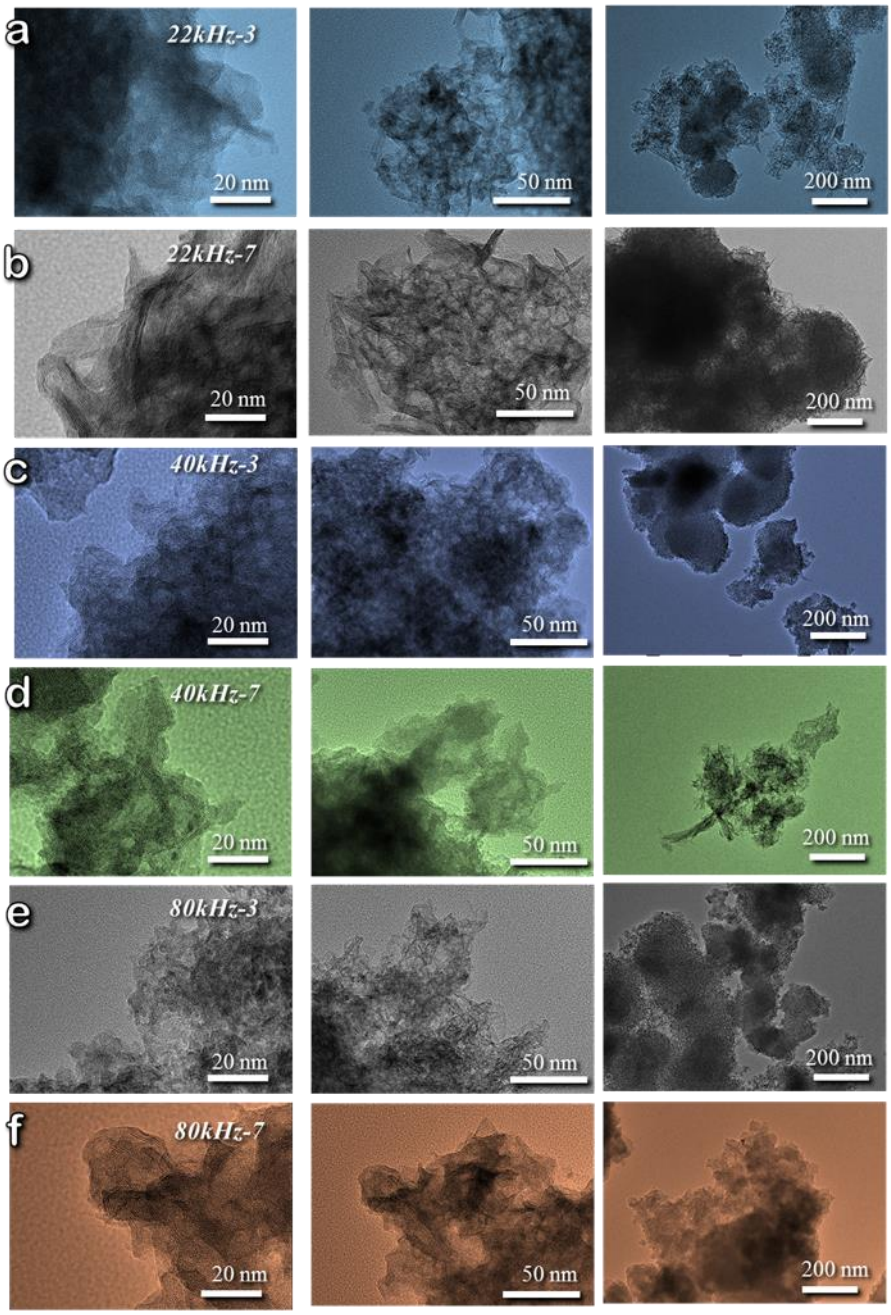

Figure 4.14. TEM images of TiO_2 samples synthesized by the 22, 40 and 80 kHz US. (Based on the results of the article submitted to ACS Sustainable Chemistry and Engineering and the published open-access article [126])

The XPS analysis studied the surface chemistry of all the herein samples. The obtained atomic percentages of O 1s, C 1s, Ti 2p and Na 2p from the high energy core level analysis are collected in **Table 4.5**, whereas the deconvoluted spectra are presented in **Figure 4.15-16.** The surface chemistry analysis revealed that all the synthesized samples showed the presence of sodium on the surface, which might be due to the adopted precipitated synthesis method. Whereas the commercial P25 sample did not show sodium on the surface. Ti 2p spectra were observed as a doublet (Ti 2p 3/2 and Ti 2p 1/2), as the corresponding peaks were separated by almost 5.7 eV, possibly due to spin-orbit coupling [151]. The position of Ti 2p 3/2 was observed at approximately 459.18 eV, which is also in good agreement with the reported titanium oxide (IV) [122,152,153]. The high-resolution deconvoluted spectra observed two peaks corresponding to O 1s. The first peak appeared in the range of 529.9-530.9 eV, indicating the Ti-O-Ti bridging oxygen. The second peak, which appears in the range of 531.2-532.1 eV represents the presence of adsorbed oxygen on the surface of samples in the form of OH groups [139,154]. Three peaks representing all the synthesized samples C 1s core energy levels were also observed. The first peak appears in the range of 284.6-284.9 eV, confirming the presence of C-C group on the surface. The second peak appeared in the 286.0-286.8 eV range, which corresponds to the C-O-C group. Whereas, the third peak appears in the 288.8-289.6 eV range, representing the C=O group [122,155].

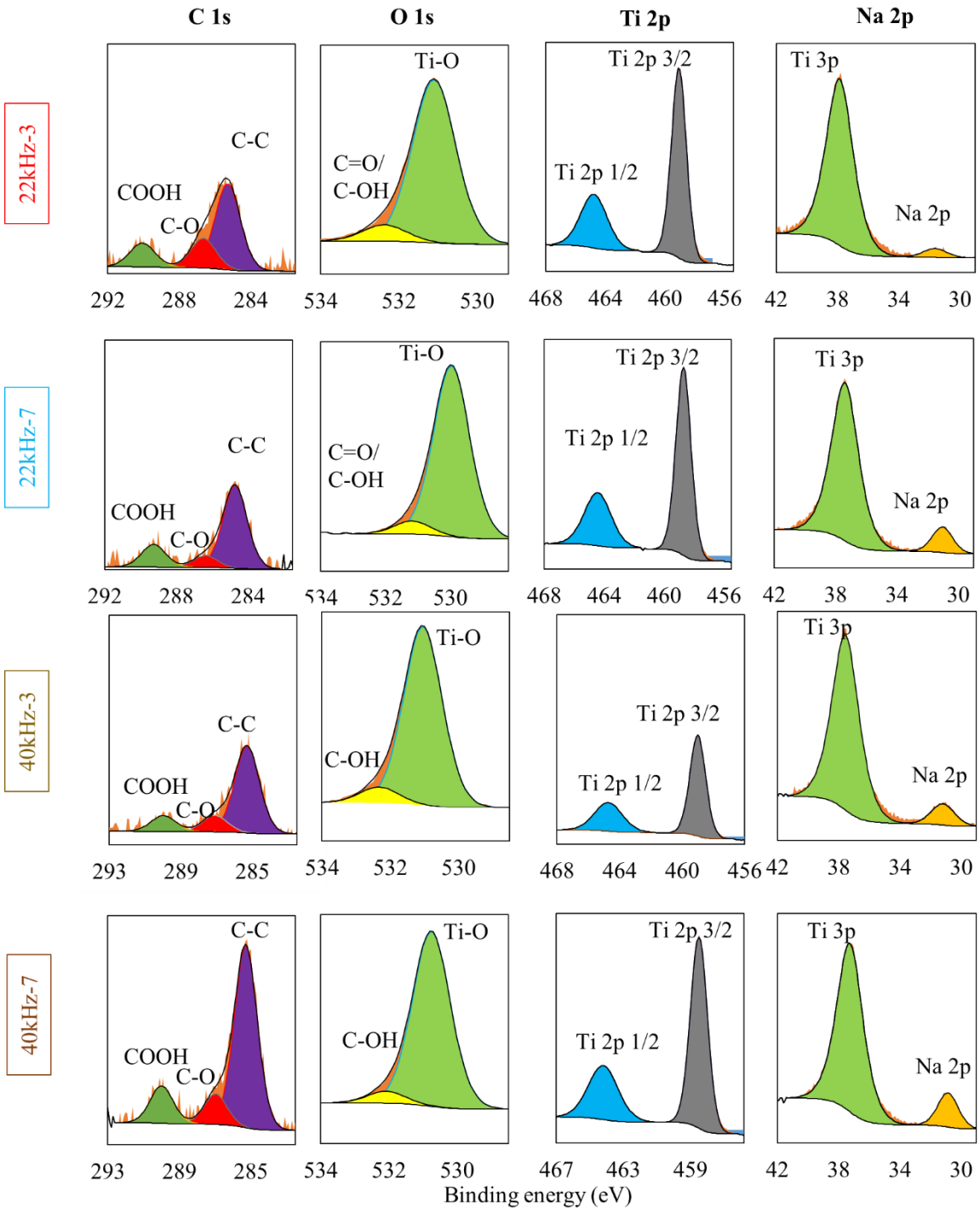

Figure 4.15. High resolution core energy spectra for the 22kHz-3, 22kHz-7, 40kHz-3 and 40kHz-7 samples. (Based on the results of the article submitted to ACS Sustainable Chemistry and Engineering and the published open-access article [126])

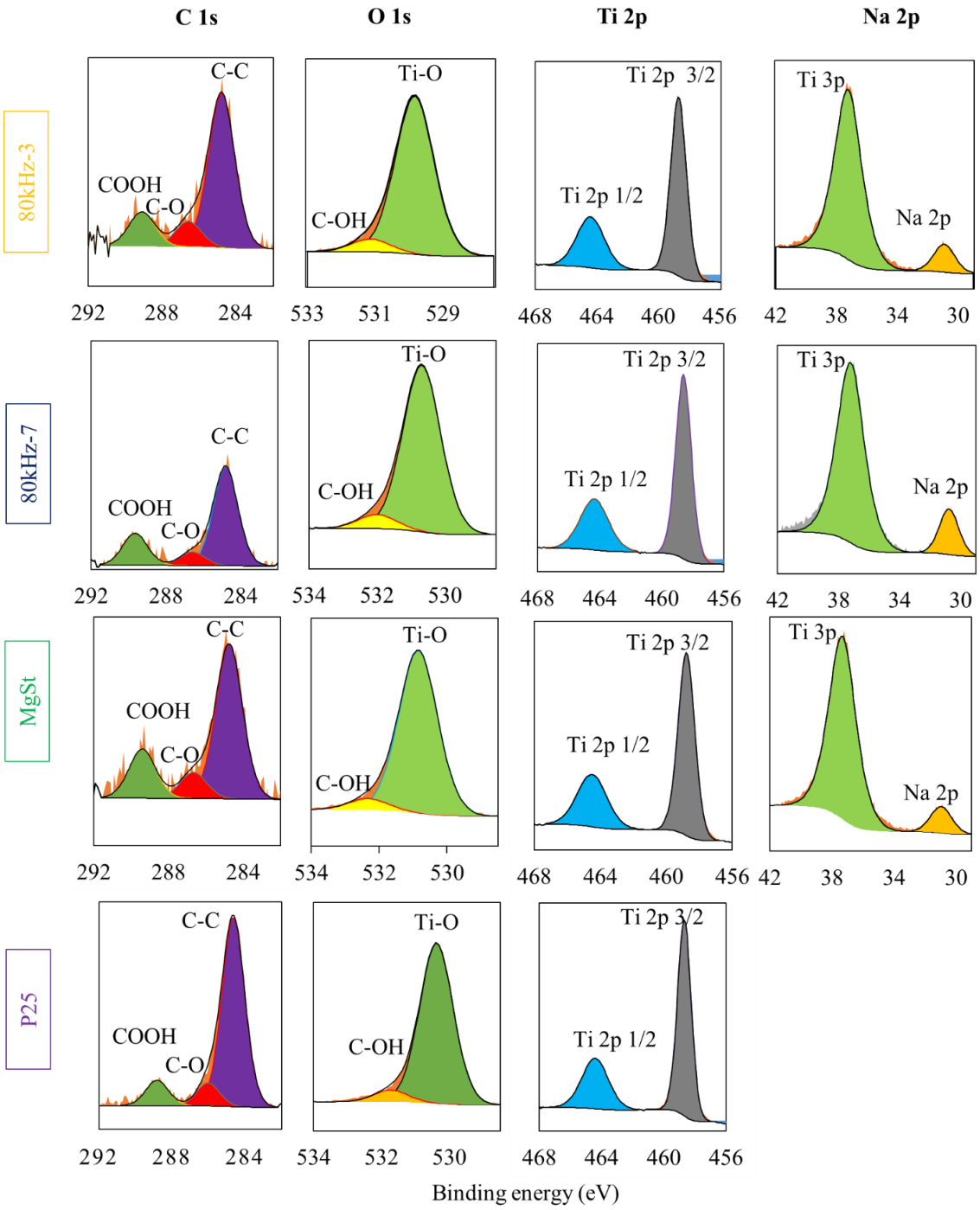

Figure 4.16. High resolution core energy spectra for the 80kHz-3, 80kHz-7, MgSt and P25 samples. (Based on the results of the article submitted to ACS Sustainable Chemistry and Engineering and the published open-access article [126])

Table 4.5. The atomic percentages of O1s, C 1s, Ti 2p and Na 2p for TiO_2 samples synthesized by the US of 22, 40 and 80 kHz, MgSt and P25 samples. (Based on the results of the article submitted in ACS Sustainable Chemistry and Engineering journal and the published open-access article [126])

	C 1s (C-C) 284.8 eV	C1s (C-O-C) 286.17 eV	C 1s (C=O) 289.58 eV	O1s (Ti-O-Ti) 530.72 eV	O1s (O-H) 531.99 eV	Ti 2p 3/2 459.18 eV	Ti 2p 1/2 464.88 eV	Na 2p 31.53 eV
22kHz-3	2.32	0.8	0.65	59.06	5.99	17.91	8.95	4.32
22kHz-7	2.00	0.29	0.54	57.7	4.43	16.55	8.27	10.22
40kHz-3	2.49	0.47	0.46	57.63	5.16	16.56	8.27	8.96
40kHz-7	3.87	0.64	0.8	54.97	3.72	15.57	7.78	12.65
80kHz-3	2.91	0.48	0.65	56.39	4.57	16.26	8.13	10.61
80kHz-7	3.97	0.54	1.29	52.86	4.43	15.17	7.58	14.16
MgSt	2.66	0.45	0.85	57.75	4.08	16.26	8.12	9.83
P25	8.76	1.08	1.18	58.84	4.38	17.18	8.58	---

4.2.2. Photocatalytic performance studies of 22, 40 and 80 kHz of US-assisted synthesized samples for partial selective oxidation of Ph-CH_2OH to Ph-CHO

All these synthesized samples and P25 sample, were studied for the photocatalytic partial selective oxidation of Ph-CH_2OH to Ph-CHO without the addition of any oxidizing agent. The P25 sample is well known for the conversion of the organic compound, but this conversion was unselective toward the products. The key goal was to design and synthesize the more active and selective TiO_2 catalyst, which showed higher yield and selectivity toward the formation of Ph-CHO from the Ph-CH_2OH.

The results of the photocatalytic activity of all the herein studies samples were presented in **Figure 4.17**. As the P25 sample showed the highest conversion (95.5 %) of Ph-CH_2OH after the 6 h of light irradiation with the yield (34.9 %) of Ph-CHO, and the selectivity toward the Ph-CHO was found 36.5 %. These results suggested that the P25 showed an unselective transformation of Ph-CH_2OH to Ph-CHO, and no other aromatic compound such as benzoic acid was detected.

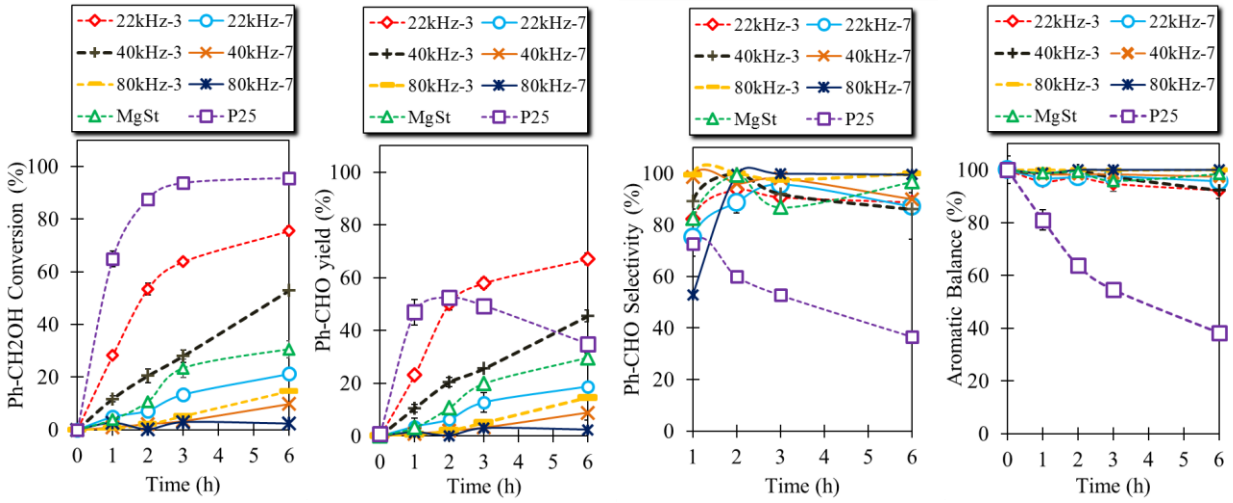

Figure 4.17. Photocatalytic activity of TiO_2 samples synthesized by the US of 22, 40 and 80 kHz, MgSt and P25 samples for partial selective oxidation of Ph-CH_2OH to Ph-CHO. (Based on the results of the article submitted to ACS Sustainable Chemistry and Engineering and the published open-access article [126])

The US-assisted synthesized samples showed a variation in the results of photocatalytic partial selective oxidization of Ph-CH_2OH to Ph-CHO. The first outcome is that the utilization of low amplitude independent of the frequency during the synthesis of TiO_2 samples led to the samples, which showed higher photocatalytic activity. Another outcome is that the increase in the utilized frequency from 22 to 80 kHz of the same amplitude results in the samples, which showed a decrease in the results of photocatalytic performance.

The sample (22kHz-3) synthesized using low frequency with low amplitude showed the highest conversion (75.5 %) of Ph-CH_2OH to the 67.1 % yield of Ph-CHO among all the US-assisted synthesized samples. Whereas the selectivity toward the Ph-CHO was found 88.8 % with a 92.1 % aromatic balance. The second-best photocatalytic performance was shown by the 40kHz-3 sample, which showed 52.9 % conversion of Ph-CH_2OH to 45.5 % yield of Ph-CHO with a selectivity of 86.1 % and an aromatic balance 92.3 %. The other US-assisted synthesized samples by using high amplitude (70 µm) of 22 and 40 kHz as well as both samples synthesized by using 80 kHz showed less than 22 % conversion of Ph-CH_2OH till the 6 h of light irradiation, while the yield of Ph-CHO was found less than 20 %. Whereas the MgSt sample showed less conversion (30.5 %) of Ph-CH_2OH to 29.6 % of Ph-CHO compared to the 22kHz-3 and 40kHz-3 samples. To sum up, the 22kHz-3 showed the highest photocatalytic partial selective oxidation of Ph-CH_2OH to Ph-CHO followed by 40kHz-3 sample.

All the discussed characterizations as well as the results of photocatalytic activity, showed that the designing and synthesis of proper catalyst is attributed to the different features which are tuning or altering the photocatalytic partial selective oxidation of the Ph-CH_2OH. All the above-presented results clearly stated that the optimization of the utilized amplitude as well as the frequency of US during the synthesis of the sample, led to an effective and flourishing approach for the designing of a proper catalyst. The utilization of US during synthesis was bimodel due to the occurrence of physical and chemical phenomena. The physical phenomena may lead to dispersion mixing and can also control crystal growth by using optimized amplitude. Whereas, the chemical phenomena may affect the chemical heterogeneity of the surface of the samples.

As described above, all the synthesized samples showed a surface pH in the range of basic medium due to using of strong base (sodium hydroxide), which leads to blockage of acidic surface sides.

The higher oxygen groups on the surface of 22kHz-3 sample compared to the synthesized and P25 samples shown by XPS measurement revealed that these oxygen groups might oxidize the organic residue to the potential carbonate or carboxylate groups, which may lead to act as a photosensitizer effect [143]. The photosensitizer effect enhances the absorption of light penetration [70,156]. 22kHz-3 sample showed one-dimensional nanostructure formation, which enhanced the light penetration. Moreover, the formation of the cage of nanostructures was observed, which also improved the absorption of the Ph-CH_2OH in the interior part of the sample, resulting in an increase in the contact area for this partial selective oxidation reaction. Another was the higher weight loss suggested by the thermal analysis, which revealed elevated OH radicals, improving the photo-oxidation performance [146]. The higher specific surface area (319 m^2/g) of 22kHz-3 sample predicted by the N_2 sorption and the formation of amorphous materials also enhances the photocatalytic partial selective oxidation process [144,157,158]. All these discussions suggested that the utilization of optimized amplitude and the frequency of US during the synthesis step altered physicochemical features and photo-oxidation performance.

4.2.3. Conclusions of section 4.2

The utilization of the US as a synthetic tool by altering the amplitude and the frequency led to the tuned physiochemical features. The low amplitude of low-frequency US-assisted synthesized samples revealed a higher specific surface area of 319 m^2/g (pore volume, 0.34 cm^3/g) and the formation of 1-dimensional nanostructures. Whereas the samples synthesized without US assistance showed a lower specific surface area of 124 m^2/g and the formation of spherical-shaped nanoparticles. The samples synthesized using the low amplitude of US frequency showed higher photocatalytic performance. Whereas samples which were synthesized by increasing the US frequency from 22 to 80 kHz with the same amplitude (30 µm), the photocatalytic oxidation performance was found in the decreasing trend. The sample synthesized using low amplitude (30 µm) of low frequency (22kHz-3) showed the best photocatalytic partial selective oxidation of Ph-CH_2OH to Ph-CHO compared to all other US-assisted synthesized samples followed by the samples synthesized using low amplitude of 40 kHz frequency (40kHz-3). Whereas, the samples synthesized using 80 kHz were found to be the least photo-catalytically active. So, these results showed that the utilization and optimization of amplitude and frequency of US during the synthesis

led to a novel catalyst with tuned physicochemical properties and enhanced selective photocatalytic performance.

4.3. Synthesis of TiO_2 samples by the US of 500 kHz

As discussed in sections 4.1 and 4.2, the utilization of 30 µm of 22 kHz frequency in the physical effect of US showed higher photocatalytic activity toward the partial selective oxidation of Ph-CH_2OH to Ph-CHO compared to other utilized amplitudes of corresponding frequency US. The change of frequency used for the synthesis revealed a wide deviation of physicochemical features and photocatalytic performance. The utilization of the higher frequency US, which impacts the chemical effect, is also necessary to study how this chemical effect of US alters the material synthesis, physicochemical properties and catalytic performance. For this purpose, two amplitudes (30 and 70 µm) of 500 kHz were used during the synthesis of TiO_2 samples by using the same procedure as for other US-assisted synthesized samples.

4.3.1. Characterization of TiO_2 samples by the US of 500 kHz

The powder XRD investigation of 500 kHz US-assisted synthesized samples was performed in order to study the crystallographic nature, and the obtained results are presented in **Figure 4.18**. The first outcome is that all the synthesized samples showed an amorphous structure. Some peaks appear at 25, 48 and 63˚ 2θ, suggesting that the anatase crystalline phase was also present [159,160]. Moreover, it is also possible that the formation of these small sizes anatase phases was initially formed due to oxidation reactions, which may act as substrates leading to the formation of an external amorphous or any other nano-layered crystalline phase [70,106,161].

The textural properties of the herein studied samples were investigated by the N_2-sorption method, and the obtained results are presented in **Table 4.6** and **Figure 4.19a,b**. The first derived outcome is that utilization of low amplitude of 500 kHz US irradiation results in the formation of porosity, while the utilization of high amplitude leads to comparatively non-porous materials. The sample 500kHz-3 revealed an elevated specific surface area (156 m^2/g), which was found to be around 25 % higher than the MgSt sample, more than 3 and 14 times compared to P25 and 500kHz-7 samples. The 500kHz-3 sample showed higher pore volumes (0.21 cm^3/g) compared to 500kHz-7, MgSt and P25 samples.

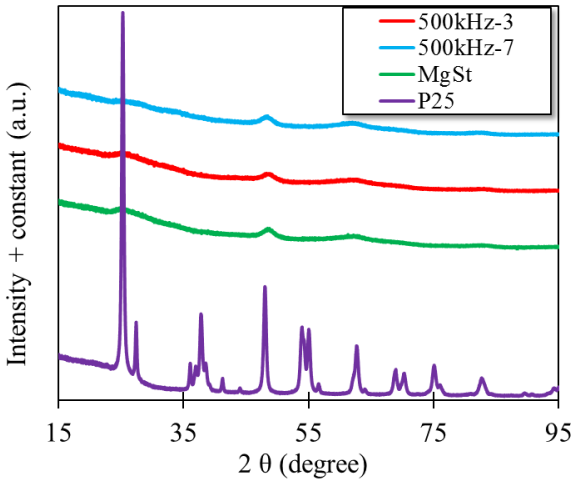

Figure 4.18. XRD of 500kHz-3, 500kHz-7, MgSt and P25 samples. (Based on the results published in open access article [123])

Table 4.6. Textural features, surface pH and optical properties of all the 500kHz-3, 500kHz-7, MgSt and P25 samples. (Based on the results published in open access article [123])

Index number	Material	Specific surface area (m^2/g)	Pore volume V_p (cm^3/g)	Estimated band gap (eV)	Surface pH
1	500kHz-3	156	0.21	3.53	7.7
2	500kHz-7	11	0.03	3.42	8.1
3	MgSt	124	0.13	3.47	8.1
4	P25	46	0.14	3.21	6.3

Based on the previous literature [70,162,163], the observed porosity of these samples can be linked to the interior aggregated spaces. The shape of these particles showed the main role in the arrangement of these particles in the space, as well as the size and volume of the formed cages or pores. As shown by the XRD analysis and the previous literature, it can be assumed that the high

porosity of 500kHz-3 and MgSt samples can be linked to the amorphous nature as well as the chemical heterogeneity of the surface of the material, which contained more OH groups which are discussed in the later part of this section. The isotherms of the synthesized samples (**Figure 4.19a)**, derived from the N_2 sorption measurements, were found closer to Type I(b) and (II) in shape according to IUPAC report [132], which is also in good agreement with the outcome of the pore size distribution (**Figure 4.19b)**. The pore size distribution showed that the 500kHz-3 and MgSt samples contained voids on a wide range of diameters, including wider micropores (1.7-2 nm), and narrow mesopores (2-8 nm). These results suggested that the existence of the pores can be linked to the extent and way of organization of the nanoparticles, with the 500kHz-3 sample having the lowest density of aggregation.

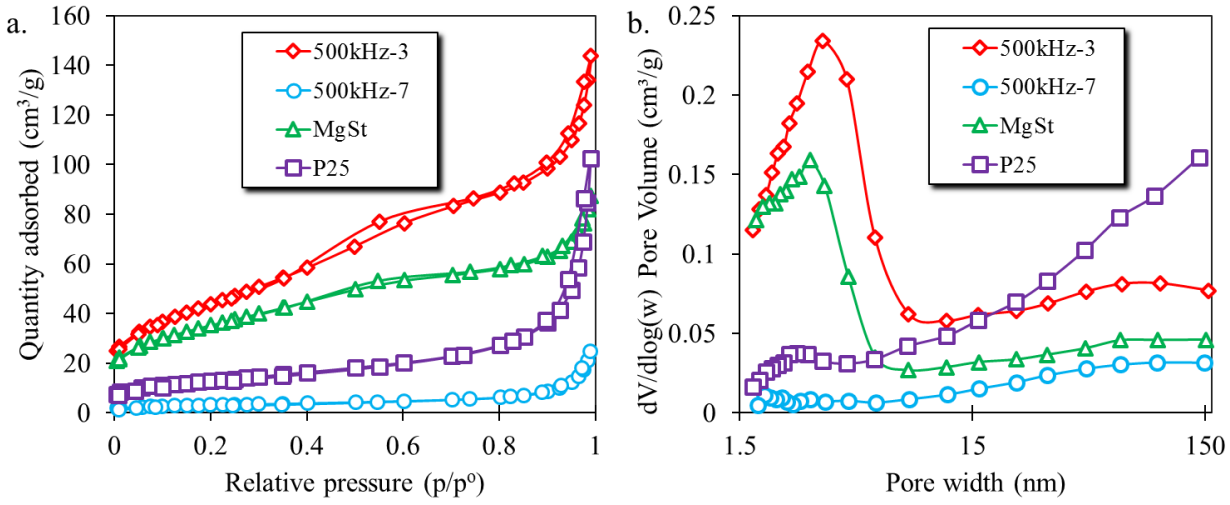

Figure 4.19. N_2 adsorption-desorption isotherms (a), and the pore size distribution (b) of 500kHz-3, 500kHz-7, MgSt and P25 samples. (Based on the results published in open access article [123])

The surface pH of all the herein-studied samples was measured in order to study the surface chemistry, which showed that P25 exhibited a weakly acidic pH, while all the synthesized samples showed basic pH (**Table 4.6**). This can be linked to the surface heterogeneity and the presence of OH groups on the samples, which can be further confirmed by thermal analysis and the XPS measurements. The thermal analysis (**Figure 4.20a**) showed that P25 sample revealed around the least weight loss 2.4 % till 400 °C, whereas all the synthesized samples showed more than 15% weight loss. This weight loss suggested that the utilization of 500 kHz US facilitates the oxolation reaction, which increases OH groups and the water moieties [70].

DSC analysis of 500kHz-3, 500kHz-7, MgSt and P25 samples showed the phase transformation of these samples. These samples, except P25 sample, showed an endothermic process up to 200 °C, indicating the removal of water moieties (**Figure 4.20b**) [133,146,147]. Whereas all these samples indicated the exothermic process in the temperature range from 200 to 450 °C, which indicated the removal of other possible organic residues from the samples [134,148,149]. In the range of temperature 450-700 °C, the transformation of amorphous to anatase crystalline phase was observed, while the transformation of anatase to rutile phase was observed in the temperature range of 700-900 °C [135,136,150].

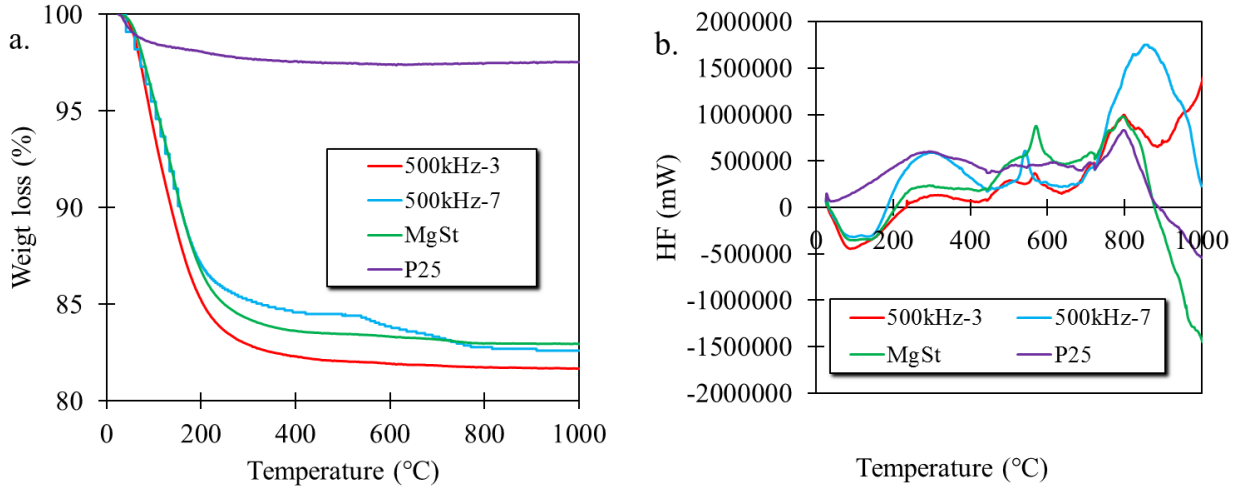

Figure 4.20. Thermographs (a), and differential scanning calorimetry (b) of 500kHz-3, 500kHz-7, MgSt and P25 samples. (Based on the results published in open access article [123])

The optical properties of all these samples were studied by using UV-Vis DRS approach. The absorption spectra revealed that all the samples except P25 sample showed absorption in the UV range, which suggested that the photocatalytic activity can be studied under UV light irradiation (**Figure 4.21a)**. The optical band gap was estimated by using Tauc plots based on Kubelka–Munk theory [164,165], and the derived outcome is presented in **Figure 4.21b** and **Table 4.6**. P25 samples showed a smaller bandgap (3.21 eV), while all the synthesized samples showed a larger bandgap.

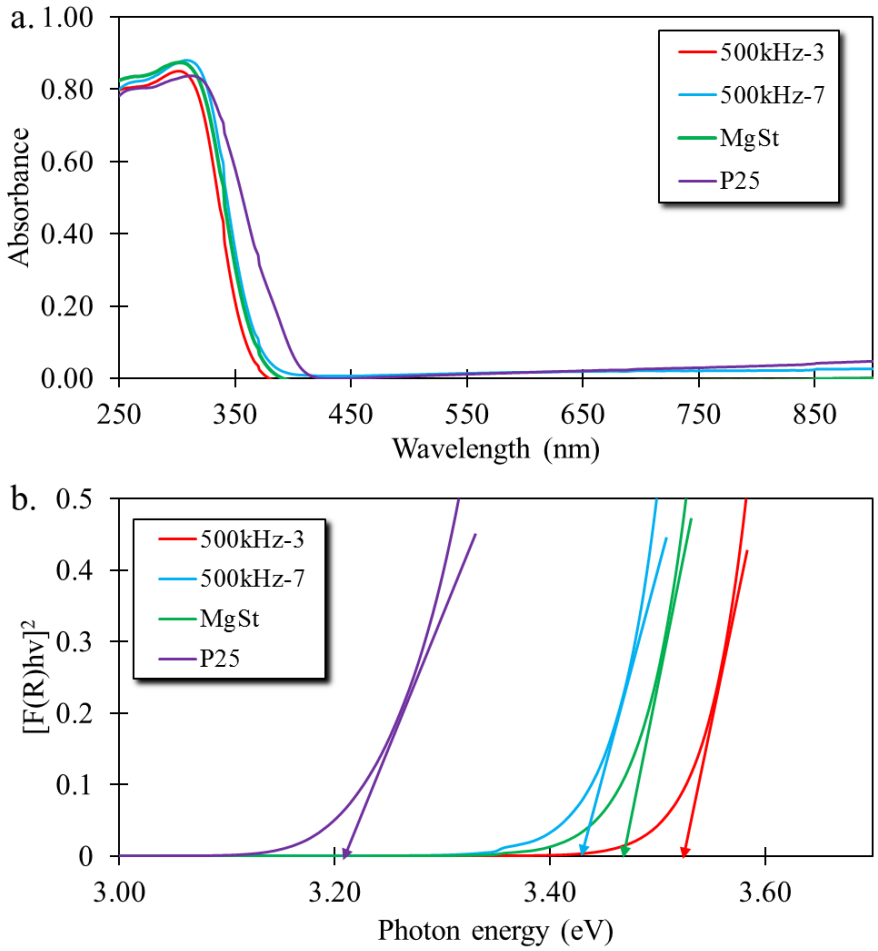

Figure 4.21. UV–Vis DRS spectra (a), Tauc plots (b) of 500kHz-3, 500kHz-7, MgSt and P25 samples. (Based on the results published in open access article [123])

As a significant difference was observed in the textural properties, the morphological features are also necessary to be investigated in order to study the effect of 500 kHz US on the morphology of the synthesized samples. The morphological features are studied by the TEM analysis, and the obtained images are presented in **Figure 4.22**. The TEM images showed that the 500kHz-3 sample showed the formation of a 1-dimensional nanostructure that looks like nanorods in the length of 10-30 nm (**Figure 4.22a)**. Moreover, these nanostructures form 3-D cobweb-like aggregates of size in the range of 100 to 300 nm. The sample synthesized by using a high amplitude of 500 kHz (500kHz-7) also showed the formation of one-dimensional nanostructures, but these nanostructures showed a condensed nature, and their aggregation was also observed in the bigger size (**Figure 4.22b)**. The observed morphology of the MgSt sample consists of spherically shaped

nanoparticles of 2 to 10 nm (**Figure 4.6f**). These results are in good agreement with the outcome from the textural features, which explained that the utilization of low amplitude led to a nanomaterials possessing higher textural properties. The inter-layer spacing was also estimated, which was found to be around 0.75 +/- 0.07 nm for both the US-assisted synthesized samples, which suggested that the interpolated water moieties or sodium ions existed but in a small portion, which is reported for the titanate-based nanotubes [166].

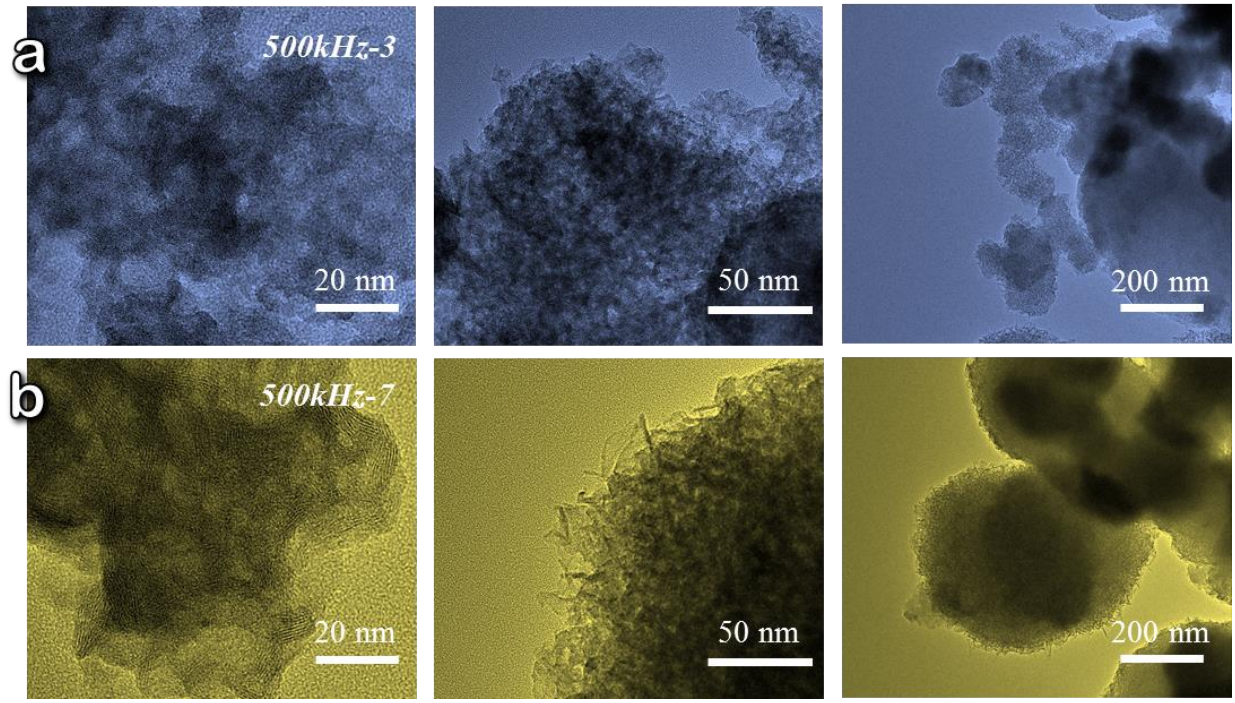

Figure 4.22. TEM images for 500kHz-3 sample (a), 500kHz-7 sample (b). (Based on the results published in open access article [123])

The morphological studies of 500kHz-3 and 500kHz-7 samples were also performed using HAADF-STEM techniques, and the obtained images are presented in **Figure 4.23a,b**. The first derived outcome is that the nanoclusters of the size in the range of 1 to 3 nm were observed on both studied samples. The density of these observed nanoclusters was found to be higher in 500kHz-3 compared to 500kHz-7 samples, which suggested that the observed nanoclusters are due to the potential chemical effect of 500 kHz US. Although it is not possible to study all these nanoclusters, some of them are clearly seen in the inset of **Figure 4.23a,b.**

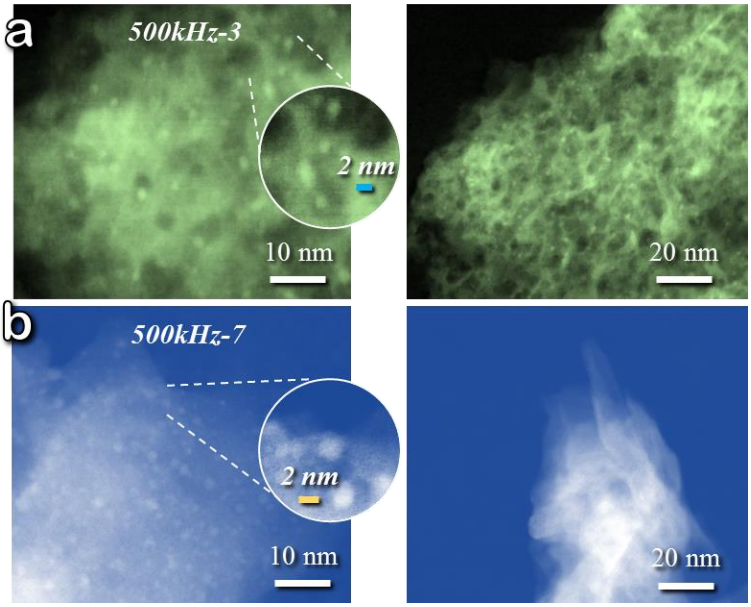

Figure 4.23. HAADF-STEM images of 500kHz-3 (a) and 500kHz-7 (b). (Based on the results published in open access article [123])

The XPS measurements studied the surface chemistry of all these herein studies samples, and the obtained results are presented in **Table 4.7** and **Figure 4.24a-d**. The first outcome is that the US-assisted synthesized samples showed a higher amount of sodium than the synthesized without US-assisted synthesized samples (MgSt), which can be linked to the titanium oxide layers, where the sodium can exist between these layers. The two contributions of Na 1S were observed in the 500kHz-3 sample, which suggested that the sodium existed in different chemical environments, as shown in **Figure 4.24a.** But, in the case of 500kHz-7 sample, only one contribution of Na 1S was observed, which suggested that the increasing amplitude of 500 kHz US led to the removal of the high energy environment of sodium. In the case of MgSt sample, one contribution of Na 1S was also observed. The high core energy level deconvulated spectra of Ti 2p of all the herein studied samples showed that the synthesized samples possessed a different environment compared to P25 sample as the maximum of Ti 2p was observed as shifted toward the low energy (**Figure 4.24b**). The observed outcome revealed that higher amount of oxygen compared to titanium was found in the US-assisted synthesized samples, which suggested that the higher amount of OH group or the water moieties are present in the layer of one-dimensional nanostructure (**Figure 4.24c**) [163,167]. Higher atomic percentages of carbon were observed for the US-assisted synthesized samples,

which suggests that carbon-containing functionalities are present in the sample that led to a positive effect on the photo-oxidation performance of TiO_2-based nanostructures (**Figure 4.24d**) [118,162].

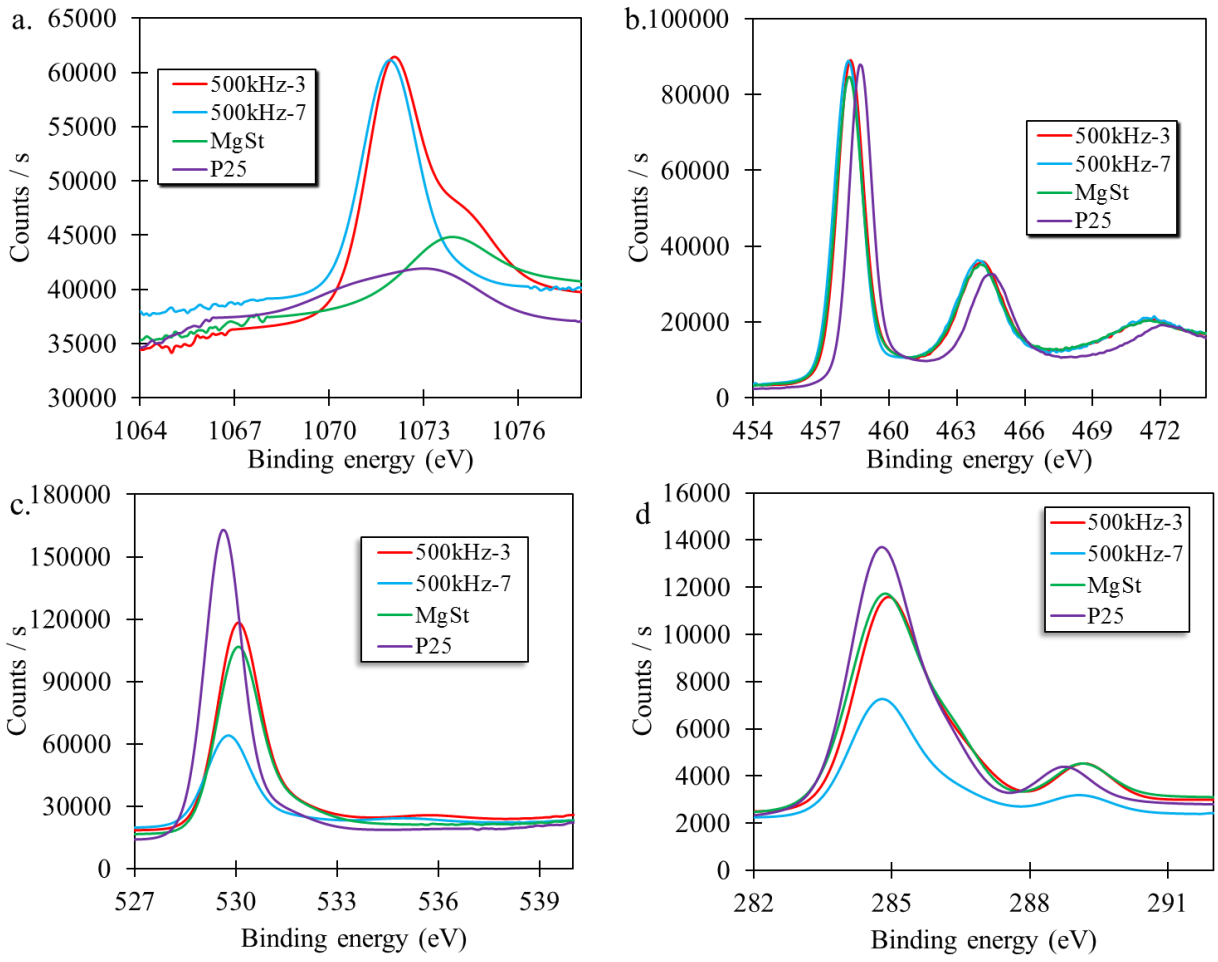

Figure 4.24. XPS high-resolution core energy level spectra of Na 1s (a), Ti 2p (b), O 1s (c) and C 1S (d) for the 500kHz-3, 500kHz-7, MgSt and P25 samples. (Based on the results published in open access article [123])

Table 4.7. The atomic percentages of O 1s, C 1s, Ti 2p and Na 2p for the 500kHz-3, 500kHz-7, MgSt and P25 samples.

	C 1s	C1s	C 1s	O1s	O1s	Ti 2p 3/2	Na 1s	
Sample	(C-C)	(C-O-C)	(COOH/ COOR)	(Ti-O-Ti)	(C=O)			
	284.8-286.0 eV	286.1-286.2 eV	288.8-289.28 eV	529.6-530.0 eV	531.0-531.1 eV	458.2-458.5 eV	1070.5-1072.2 eV	1073.1-1074.3 eV
500kHz-3	11.8	4.5	2.0	44.4	10.5	17.1	6.9	2.8
500kHz-7	12.8	5.1	2.4	38.1	13.2	15.3	12.6	0.5
MgSt	11.1	2.3	1.7	29.4	11.9	40.2	2.9	0.5
P25	9.5	1.8	1.6	37.4	4.9	42.7	0.8	1.3

4.3.2. Photocatalytic performance studies of 500 kHz of US assisted synthesized samples for partial selective oxidation of Ph-CH_2OH to Ph-CHO

The photocatalytic activity of all the herein samples was studied for the photocatalytic partial selective oxidation of Ph-CH_2OH to Ph-CHO without the addition of any oxidizing agent by using the same experimental conditions as used for the above-discussed samples. As P25 showed higher photocatalytic conversion (95.5 %) of Ph-CH_2OH, the yield of the Ph-CHO was found 34.9 %. No other aromatic compound such as benzoic acid, was detected by GC analysis, which suggested that the formed Ph-CHO was further unselective converted to any possible aliphatic compound (**Figure 4.25**). P25 sample is also well known and reported for the ability to the unselective transformation of organic compounds under UV light irradiation [168–170]. These results suggested that the P25 showed higher photocatalytic conversion, but this conversion was unselective toward the products.

The higher photocatalytic activity can be assigned to its nano-size particles as well as the composition of its crystallinity, which contains the two crystal phases such as anatase and rutile, in a well-defined order [171]. The selectivity toward the products is ultimately important due to lowering the formation of any side products, which need further purification steps for the realistic production process. The key target to synthesize novel nanomaterials, which showed higher selective transformation of the aromatic alcohol by targeting the final yield of produced aldehyde.

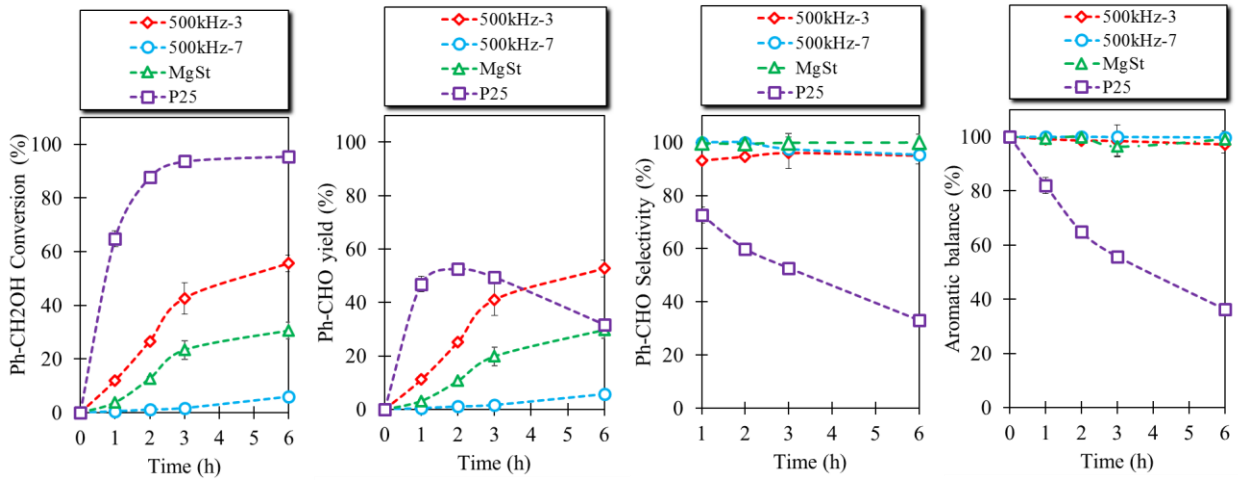

Figure 4.25. Photocatalytic activity of 500kHz-3, 500kHz-7, MgSt, and P25 samples for partial selective oxidation of Ph-CH_2OH to Ph-CHO. (Based on the results published in open access article [123])

The US-assisted synthesized samples showed a variation in the result of photocatalytic activity. 500kHz-3 sample exhibited an increasing trend of Ph-CH_2OH conversion with an increasing yield of Ph-CHO. After the 6 h of light irradiation, the 55.6 % conversion of Ph-CH_2OH was observed, and the yield of Ph-CHO was found 52.7 %, which was found 80 % higher as compared to the yield of Ph-CHO obtained in the case of P25. The selectivity and aromatic balance were found >95 %. So, these results showed that the 500kHz-3 sample was found to be a good catalyst, which showed the highest partial selective oxidation of Ph-CH_2OH to Ph-CHO. Whereas the sample synthesized by using the higher amplitude (70 µm) of the same 500 kHz US was found unreactive. The sample synthesized without US assisted sample (MgSt), showed lower conversion (30.5 %) of Ph-CH_2OH as compared to 500kHz-3 and P25 samples till the 6 h of light irradiation, but the yield of Ph-CHO was found 29.6 %, which was found slightly lower as compared to the obtained

yield of Ph-CHO in case of P25 after 6 h of light irradiation. But, in this case, the selectivity was found > 96 %, which is a more crucial aspect in order to avoid any further purification steps.

The photocatalytic activity results of US-assisted synthesized samples can be linked to several features, such as morphological properties. 500kHz-3 contained the cages of nanostructures, which can enhance the absorption of Ph-CH_2OH molecules toward the photo-reactive sides, such as the nanorods. The higher photo-catalytic activity of 500kHz-3 samples can also be linked to the formation of 1-dimension nanostructures such as nanorods and the presence of higher surface functional groups on the surface of the sample, as shown by the thermal analysis. Another, the formation of the nano-cluster on the nanostructure of 500kHz-3 sample, which also facilitates the light penetration spots, led to improvement in the photocatalytic activity [172,173]. Whereas the 500kHz-7 sample was found to be almost inactive, which may be due to the condensed or non-porous nature of the samples, resulting in the blockage of the diffusion of Ph-CH_2OH molecule in the inner part of the cage formed by the nanostructure of 500kHz-7 sample. The condensed nature of 500kHz-7 sample did not allow the higher penetration of light in the inner parts compared to the 500kHz-3 sample, which also lowered the photocatalytic performance. The presence of a higher amount of sodium on the surface of 500kHz-7 compared to 500kHz-3 sample results in the blockage of the photo-catalytic activity [174].

4.3.3. Conclusions of section 4.3

The US of the high frequency of 500 kHz, which lies in the chemical effect range of US with two different amplitudes, was used during the synthesis of the TiO_2 sample to study the effect of 500 kHz US on the physiochemical feature and photocatalytic performance. The derived outcome was that nanostructure with elevated textural, surface heterogeneity, and structural and morphological properties play an important role in the photocatalytic performance. Another observed outcome was that the utilization of 500 kHz US led to different multiphase titanium oxide nanorods like structure, which were decorated with nanoclusters. The use of a low amplitude of 500 kHz resulted in the formation of the sample with high porosity and the formation of the caged of formed 1-dimension nanorods like structure as compared to the sample synthesized by using high amplitude, which showed less porosity and dense morphology. Due to these altered features, the 500kHz-3 sample showed higher partial selective oxidation of Ph-CH_2OH to Ph-CHO, whereas 500kHz-7

sample was found unreactive. These results suggested that the utilization of different amplitude of high frequency 500 kHz of US leads to altering the physicochemical properties as well as photocatalytic performance.

4.4. Catalytic selective cleavage of C_α-C_β bond of lignin-based β-O-4 model compound

Among the US-assisted synthesized TiO_2 samples by 22, 40, 80 and 500 kHz frequency and different amplitudes, the 22kHz-3 sample showed the highest photocatalytic conversion of Ph-CH_2OH to the highest yield of Ph-CHO compared to all other US-assisted synthesized samples. Therefore, 22kHz-3 was selected among the US-assisted synthesized TiO_2 samples for the catalytic selective cleavage of C_α-C_β bond of lignin-based β-O-4 model compound along with MgSt and P25 catalysts. PP-ol is selected as a model diaromatic compound, which possesses β-O-4 linkage with the additional bonds such as C_α-C_β, C-O and C-OH and is the representative of the diaromatic model compound of lignin.

4.4.1. Photocatalytic conversion of PP-ol

It is very important to study the photocatalytic reaction's dependence on substrate concentrations and catalytic loading. Initially, commercial P25 was studied to optimize the concentrations of PP-ol and catalytic loading to get the best experimental conditions for the catalytic oxidation process. Firstly, the effect of various substrate concentrations ranging from 0.5 mM to 2.5 mM on photocatalytic activity was studied using 1g/L of catalyst loading of commercial P25 sample. The derived outcomes are presented in **Figure 4.26**.

The photocatalytic conversion of PP-ol was observed in the production of various compounds such as Ph-CHO, phenyl formate (Ph-OCHO), phenol (Ph-OH) and PP-one, which are in the good agreement with the reported literature by using other photo-catalysts [175,176]. Among these obtained products, the Ph-CHO has higher potential usage for different industrial applications and in the synthesis of high-value products compared to other obtained products. Therefore, the yield of Ph-CHO is the key targeted product to optimize the reaction’s parameters. The first outcome from the optimizations of different substrate concentrations is that conversion of low concentration of PP-ol was found to be higher compared to high concentration of PP-ol. But in the case of the target products, this scenario was observed in the opposite trend, a low concentration of PP-ol

showed a low yield of Ph-CHO, while a higher concentration showed a higher yield of Ph-CHO. Whereas, the yield of other products was found in varying amounts. The aromatic balance of these reactions was found to increase trend with the increasing concentration of PP-ol. A higher yield (25 %) of Ph-CHO was found by using the 1.5 mM concentration of Ph-CHO, and it also showed higher aromatic balance compared to a low concentration of PP-ol, indicating lower formation of any possible side products till the 6 h of light irradiation. So, 1.5 mM concentration of PP-ol was used for the optimization of catalytic loading.

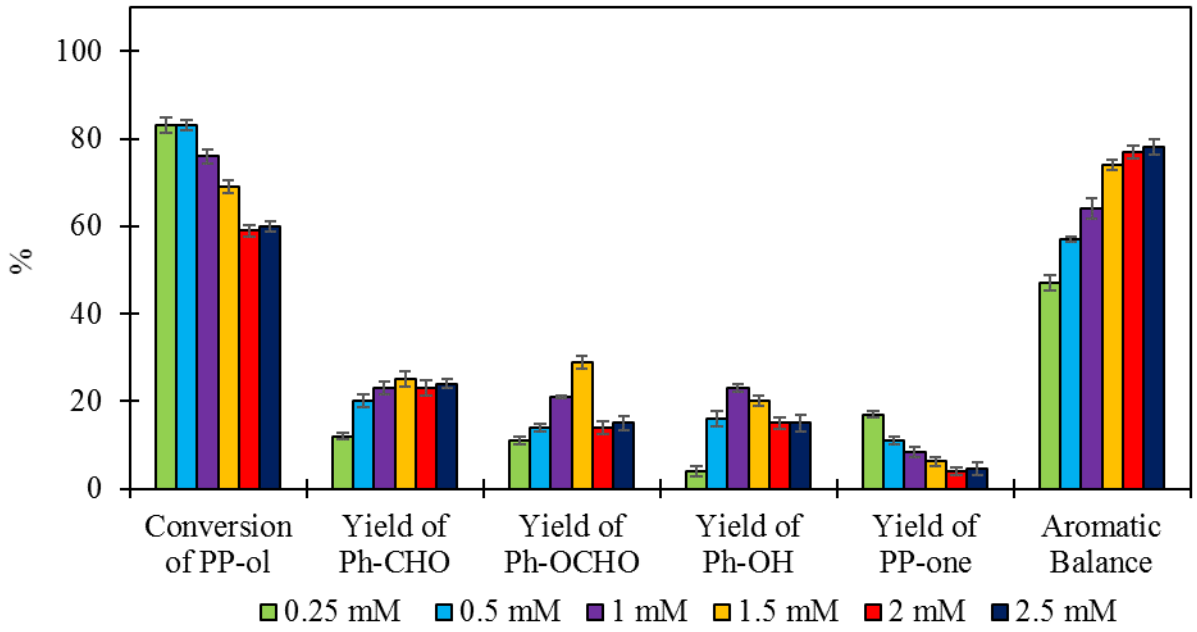

Figure 4.26. Optimization of different concentrations of PP-ol for the photocatalytic activity of P25. (Based on the results of the article submitted to ACS Sustainable Chemistry and Engineering)

Various catalytic loading in the range of 0.5 g/L to 4 g/L was optimized by using the 1.5 mM concentration of PP-ol. The obtained results are presented in **Figure 4.27**. Conversion of PP-ol was found in the opposite trend as compared to the results of the optimization of different concentrations of PP-ol. The conversion of PP-ol was found in the increasing trend with the increasing catalytic loading of P25 sample. 1 g/L catalytic loading of P25 showed a 69 % conversion of PP-ol with a 25 % yield of Ph-CHO and 74 % aromatic balance till the 6 h of light irradiation, which was found higher selective conversion compared to other catalytic loadings. Thus, 1 g/L was found to be the optimized catalytic loading.

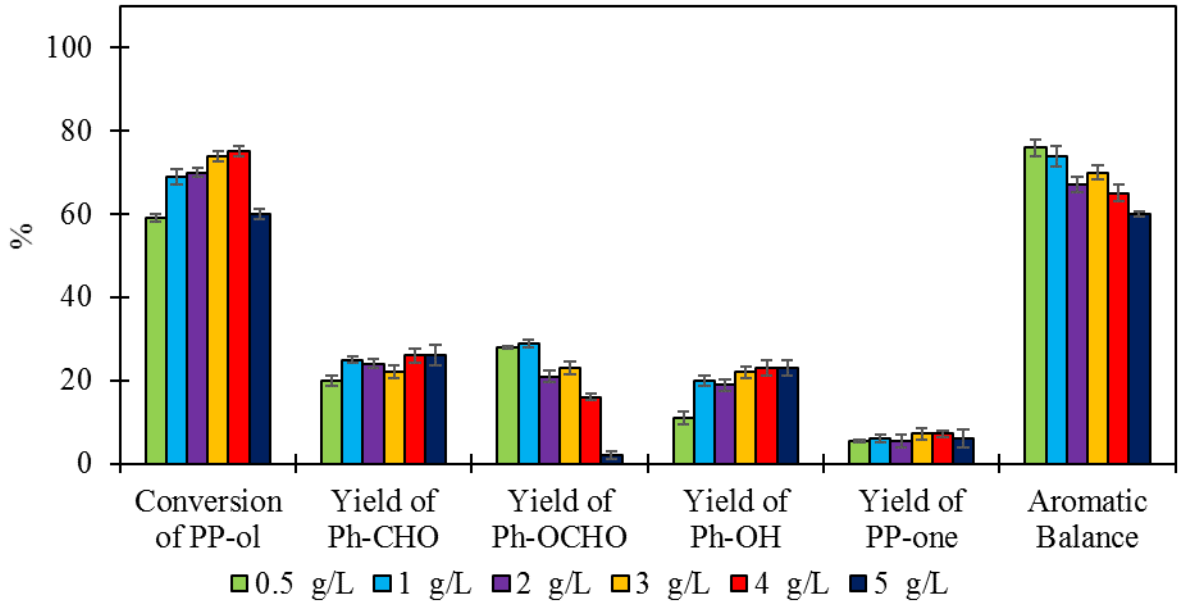

Figure 4.27. Optimization of different catalytic loading P25 of photocatalytic conversion of PP-ol to the corresponding products. (Based on the results of the article submitted to ACS Sustainable Chemistry and Engineering)

Using the optimized concentration (1.5 mM) of PP-ol substrate and catalyst loading (1 g/L), the photocatalytic performance of the synthesized 22kHz-3 and MgSt samples was studied and compared to the results of P25 sample. The P25 sample revealed the conversion of PP-ol (69.9 %) to the yield of different products such as Ph-CHO (24.9 %), Ph-OCHO (28.9 %), Ph-OH (20.5 %) and PP-one (6.2 %) with the 73.6 % aromatic balance, after the 6 h of light irradiation. While in case of the US-assisted synthesized 22kHz-3 sample showed a 57.2 % conversion of PP-ol to the yields of Ph-CHO (41.8 %), Ph-OCHO (19.5 %), Ph-OH (2.6 %) and PP-one (10.1 %), with the 84.9 % aromatic balance (**Figure 4.28**). Whereas the sample synthesized without US assistance, MgSt showed 35.8 % conversion of PP-ol, with 17.3 % yield of the targeted Ph-CHO product, which was found to be lower than 22kHz-3 and commercial P25. While the yield of other products such as Ph-OCHO, Ph-OH and PP-one was found 8.2, 1.7 and 4.5 %, respectively. The outcome of these results indicated that the utilization of US with optimized amplitude during the synthesis elevated the photocatalytic selective performance to obtain the targeted products comparing to MgSt sample which synthesized without US assistance, even the commercial P25 sample.

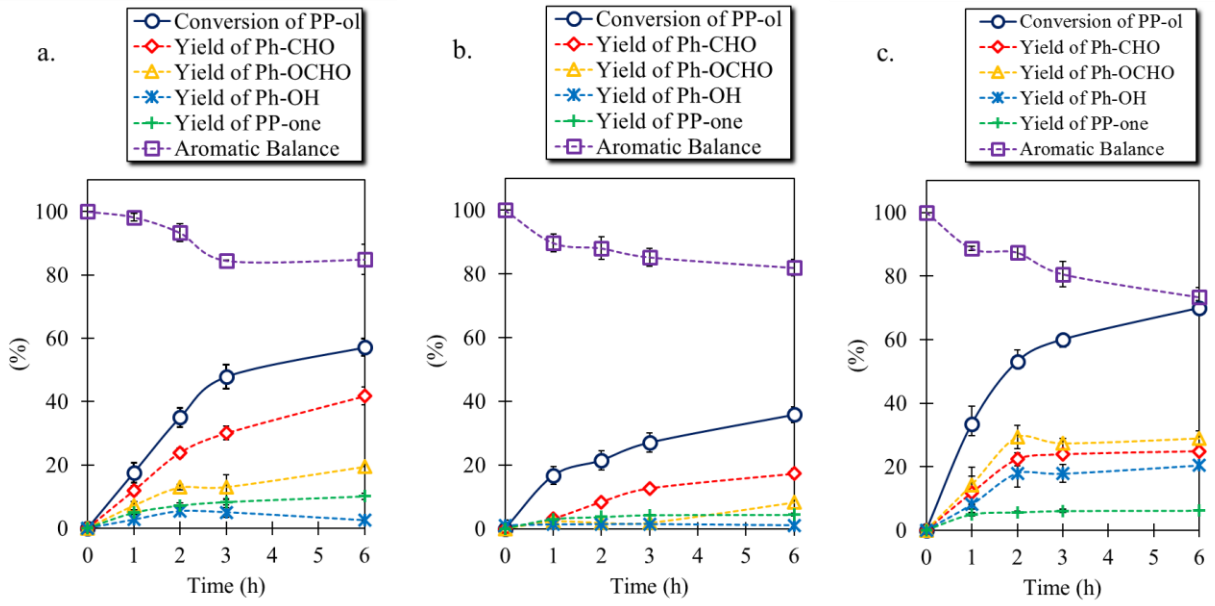

Figure 4.28. Photocatalytic conversion of PP-ol to the corresponding products by using commercial 22kHz-3 (a), MgSt (b) and P25 (c) samples. (Based on the results of the article submitted to ACS Sustainable Chemistry and Engineering)

4.4.2. Effect of calcination on the crystallinity and photocatalytic performance

One of the key aims of this thesis is to synthesize the catalyst by avoiding high-energy demanding steps, such as calcination, in order to be greener. To verify this task, the calcination of the best performing US-assisted sample, MgSt and P25 samples were calcined at 500 ºC for 5 h. The XRD method was used to study the crystalline nature, and the photocatalytic selective activity was studied for the conversion of Ph-CH_2OH to the corresponding products by the same reaction conditions. The outcome of the crystalline study was presented in **Figure 4.29**, **Table 4.8**, which showed that the increment in the anatase phase was observed in the 22kHz-3 calcined (22kHz-3 Cal.) sample compared to the without calcined sample. MgSt calcined sample also possessed the more prominent anatase phase as can be observed in **Table 4.8**. While in the case of P25 sample, the calcination did not significantly affect the crystalline nature.

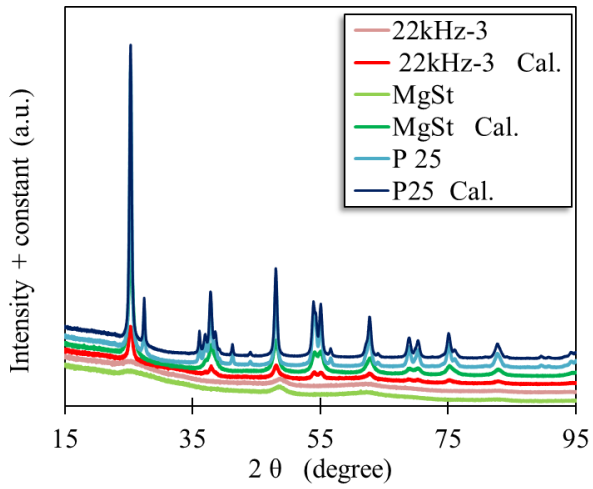

Figure 4.29. Effect of calcination on the crystallinity of the 22kHz-3, MgSt and P25 samples. (Based on the results of the article submitted to ACS Sustainable Chemistry and Engineering)

The outcome (**Figure 4.30**) of the photocatalytic selective conversion of PP-ol showed that the 22kHz-3 Cal. revealed a slightly higher conversion of PP-ol, but the yield of the targeted Ph-CHO product was found to be lower than the 22kHz-3 sample without calcination. MgSt calcined sample (MgSt Cal.) showed higher conversion of PP-ol as well as a higher yield of Ph-CHO as compared to MgSt sample without calcination, but the yield of Ph-CHO was still observed to be less than the yield obtained by 22kHz-3 and 22kHz-3 Cal. sample till the 6 h of light irradiation. While P25 calcined sample (P25 Cal.) showed significantly lower conversion of PP-ol and yield of all products except the yield of PP-one. These results exhibited that the adopted method for the US-assisted synthesized samples showed higher photocatalytic selective conversion of PP-ol to the corresponding products without using the high energy-demanding step of calcination during the synthesis of the sample.

Table 4.8. Calculated crystallite size of calcined samples by Scherer method. (Based on the results of the article submitted to ACS Sustainable Chemistry and Engineering)
(Calcination at 500 ˚C with ramp of 10 ˚C/min for 5 h)

Sample	Dcr Anatase (011) [nm]	Dcr Rutile (110) [nm]
22kHz-3	3.1	-
22kHz-3 Cal.	9.5	-
MgSt	-	-
MgSt Cal.	9.1	-
P25	17.3	22.3
P25 Cal.	17.4	22.5

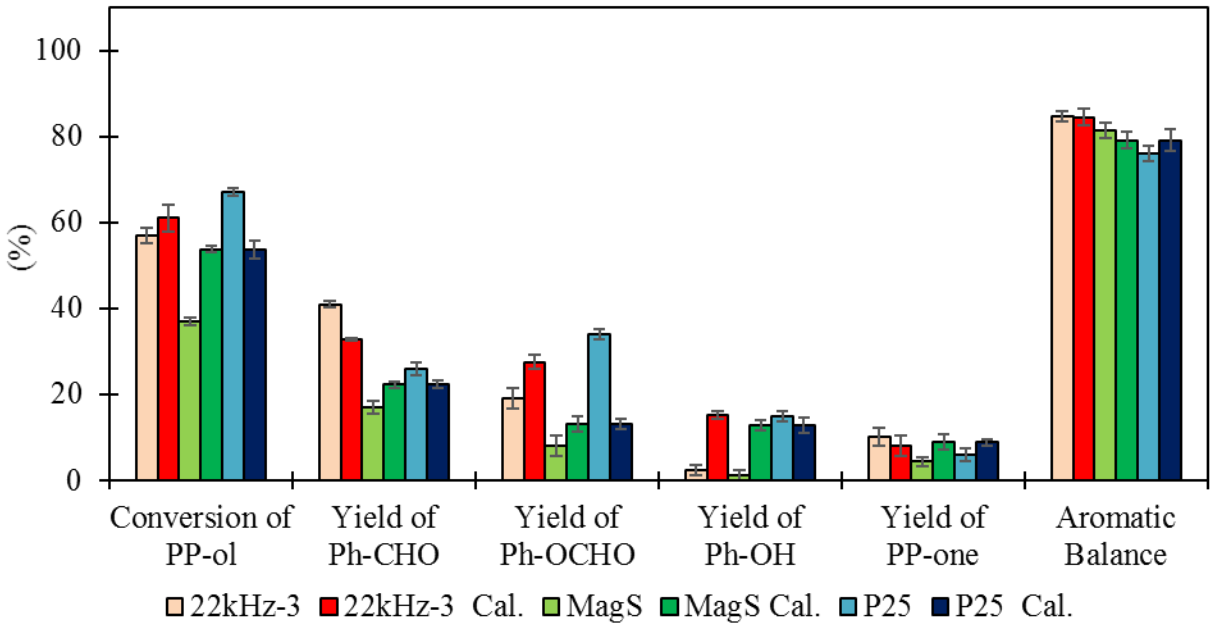

Figure 4.30. Effect of calcination on photocatalytic activity for converting PP-ol to the corresponding products using calcined and without calcined 22kHz-3, MgSt and P25 samples. (Based on the results of the article submitted to ACS Sustainable Chemistry and Engineering)

4.4.3. Reusability and stability studies

The designing and synthesis of the catalysts with key features such as stable, easy recoverable and reusable without affecting the catalytic efficiency for multiple experiments is the most important parameter for the solid catalyst. The stability and reusability of the 22kHz-3, MgSt and P25 samples were studied for the photocatalytic conversion of PP-ol to the corresponding products. US-assisted synthesized sample 22kHz-3 showed a similar conversion of PP-ol to a similar yield of the corresponding products after the fifth run of the photocatalytic experiment till the 6 h of light irradiation (**Figure 4.31**). Whereas the MgSt sample revealed a lower conversion of PP-ol and the yield of the products after the second run of photocatalytic experiments. P25 sample also showed a similar photocatalytic performance up to the fifth run. Thus, these results showed that the US-assisted synthesized 22kHz-3 sample can be reusable without losing the catalytic performance up to multiple runs.

The leaching of Ti metal from the catalyst during or after the photocatalytic experiments should be avoided to keep a stable catalyst and same photocatalytic performance. EDXRF of the filtered solution after the fifth run of photocatalytic reaction for 22kHz-3, MgSt and P25 samples were performed to study the Ti leaching after the photocatalytic experiments. The derived outcome is presented in **Figure 4.32**, a peak analogous to Ti metal was not observed. The appearance of peaks in EDXRF spectrum corresponds to Rh and Cu, which are coming from Rh lamp and finger prints of the spectrometer, respectively. These results showed that all the herein samples were stable and could be reused for multiple runs of photocatalytic experiments without leaching of Ti metal.

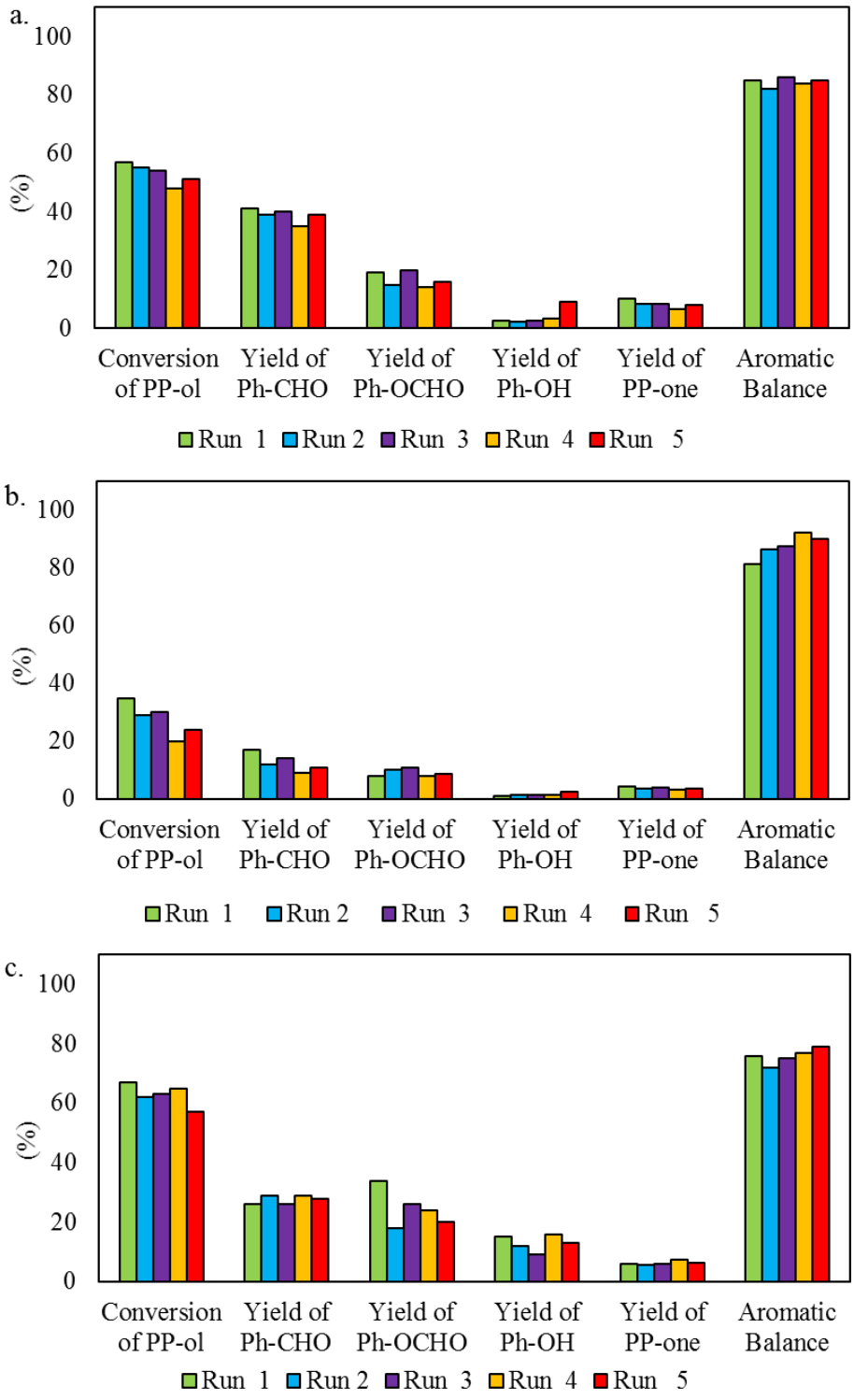

Figure 4.31. Reusability photocatalytic studies of 22kHz-3 (a), MgSt (b) and P25 (c) samples. (Based on the results of the article submitted to ACS Sustainable Chemistry and Engineering)

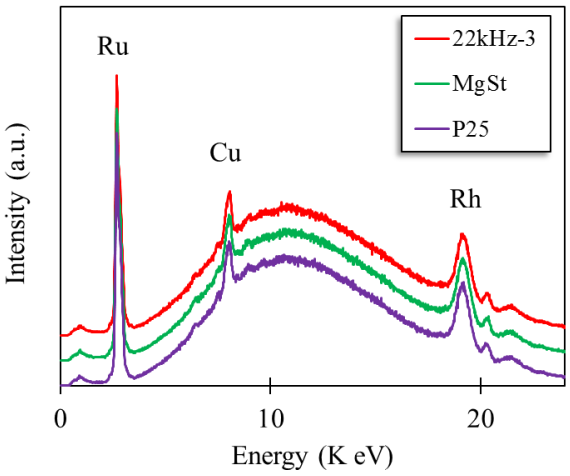

Figure 4.32. EDXRF spectra of the solution after the fifth run of photocatalytic experiments for the conversion of PP-ol substrate for 22kHz-3, MgSt and P25. (Based on the results of the article submitted to ACS Sustainable Chemistry and Engineering)

4.4.4. Sonophotocatalytic oxidation of PP-ol

The coupling of US with photocatalysis is called sonophotocatalysis and is broadly studied for the degradation of organic pollutant compounds [107,177,178], but it is not widely used for the selective oxidation of organic compounds, especially for the diaromatic phenolic compounds. So sonophotocatalytic studies of 22kHz-3, MgSt and P25 samples was explored by replacing the magnetic stirring with the US of 22 kHz, by taking advantage of the different physical effect. The derived outcome is presented in **Figure 4.33**.

The results of the sonophotocatalytic activity of 22kHz-3 sample showed a 45.8 % conversion of PP-ol, which is lower than the conversion (57.2 %) shown by photocatalytic process. Whereas, the yield (45.5 %) of the targeted Ph-CHO product was found to be higher than the yield (41.8 %). obtained from the photocatalytic activity till the 6 h of light irradiation. The key important observation was the increment in the aromatic balance, which was found 96 %, and is higher than the aromatic balance (84.8 %) found in photocatalytic activity. The results of the sonophotocatalytic activity of MgSt sample showed 23.2 % conversion of PP-ol, which is less than the conversion of PP-ol revealed by the photocatalytic test, whereas the yield of all the products was found to be almost the same in photocatalytic and sonophotocatalytic activity, which is also

leading to increasing the aromatic balance. P25 sample also 54.8 % conversion of PP-ol by sonophotocatalytic tests, which was also observed lower by the photocatalytic tests. But, the yield of the targeted Ph-CHO product was found to be the same, while the yield of the other products by sonophotocatalytic tests was found to be slightly lower than photocatalytic tests.

The outcome of the sonophotocatalysis showed that coupling of the US to the photocatalysis could increase the selective cleavage of the C_{α}-C_{β} bond during the sonophotocatlytic reaction, as the conversion of PP-ol was found lower, but interestingly, the yield of the targeted products i.e. Ph-CHO and also the yield of the oxidation product PP-one were found to be either the same or slightly higher than the yield obtained in case of photocatalysis, which led to higher selectivity toward the targeted products. Due to this, the aromatic balance was significantly elevated. This increment in the aromatic balance indicated the formation of any possible byproducts by hindering the side reaction, which may lead to non-selective conversion or mineralization of the aromatic compounds.

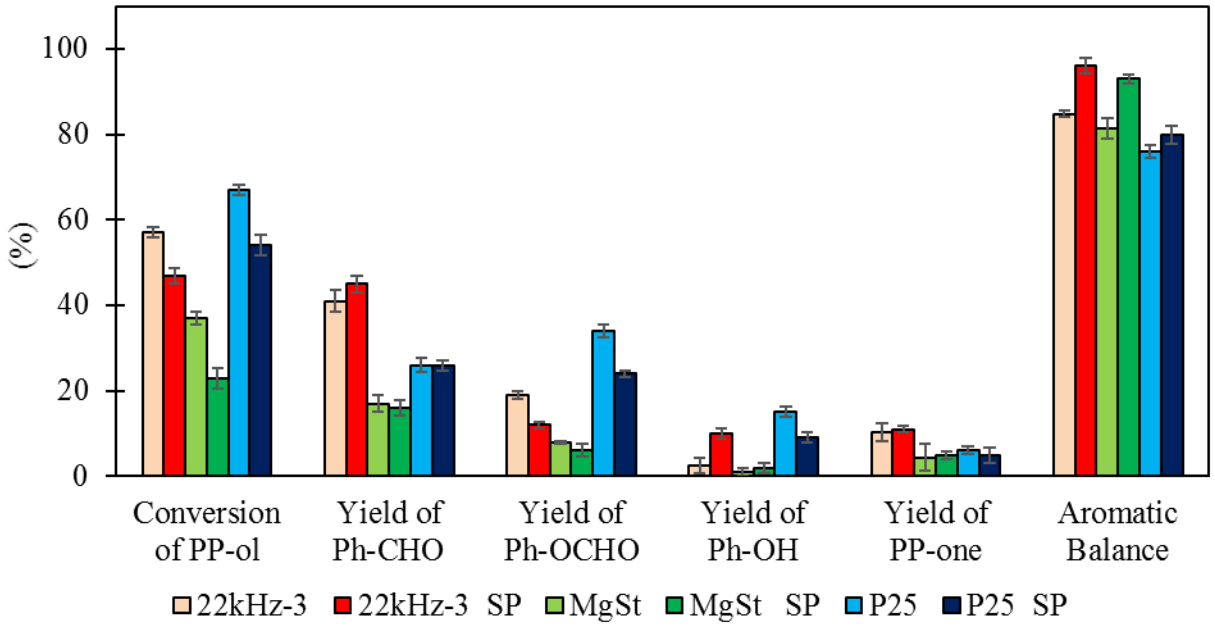

Figure 4.33. Sonophotocatalytic activity for the oxidation of PP-ol to the corresponding products by using 22kHz-3, MgSt, and P25 samples. (Parenthesis "SP indicated the results of sonophotocatalytic experiments) (Based on the results of the article submitted to ACS Sustainable Chemistry and Engineering)

This selective conversion and the elevated aromatic balance could be attributed to the potential physical effect of mixing and enhanced mass transfer produced by low frequency US. The particles of the catalysts can move in the horizontal direction during the magnetic mixing, which can lead to the aggregation of the catalyst in the suspension, resulting in a less reactive reaction. Whereas the particles of the catalyst can move in the vertical direction during the US, which results in the deaggregation of particles and availability of specific surface area resulting in increasing the selective transformation [109,179].

The aqueous solution of the different organic compounds, such as methylene blue, methyl orange, congo red, rhodamine and paracetamol etc., are subjected to the US can significantly degrade these compounds. The sonication of water results in the formation of OH radicals, which can degrade these organic compounds [5]. But acetonitrile was used as a reaction medium for the current sonophotocatalytic tests. Thus the sonocatalytic studies for all the herein studies samples were also performed without irradiation of light in order to study whether this sonophotocatalytic conversion of PP-ol was due to the US solely or due to coupling of US with the photocatalysis. The results of the sonocatalytic test were presented in **Figure 4.34a**, which showed that no conversion was observed. These results are supported by the literature. Such as, Matsuzawa *et al*. [179] also studied the commercial P25 sample for the sonocatalytic (US of 45 kHz with power 50 W) degradation of 2-dibenzothiophenes by using the acetonitrile as a reaction medium, and no conversion of 2-dibenzothiophenes was observed.

Some control experiments, such as photolysis, sonolysis and sonophotolysis for PP-ol solution in acetonitrile solvents, were also studied without the addition of catalyst samples. The results of all these control experiments (**Figure 4.34b**) revealed that the PP-ol substrate was found stable under light irradiation or US irradiation, and also the coupled light and US irradiation as there was no conversion of PP-ol was observed. This no conversion of PP-ol in acetonitrile under sonolysis, sonophotolysis and sonocatalytic conditions might be due to the non-aqueous reaction medium.

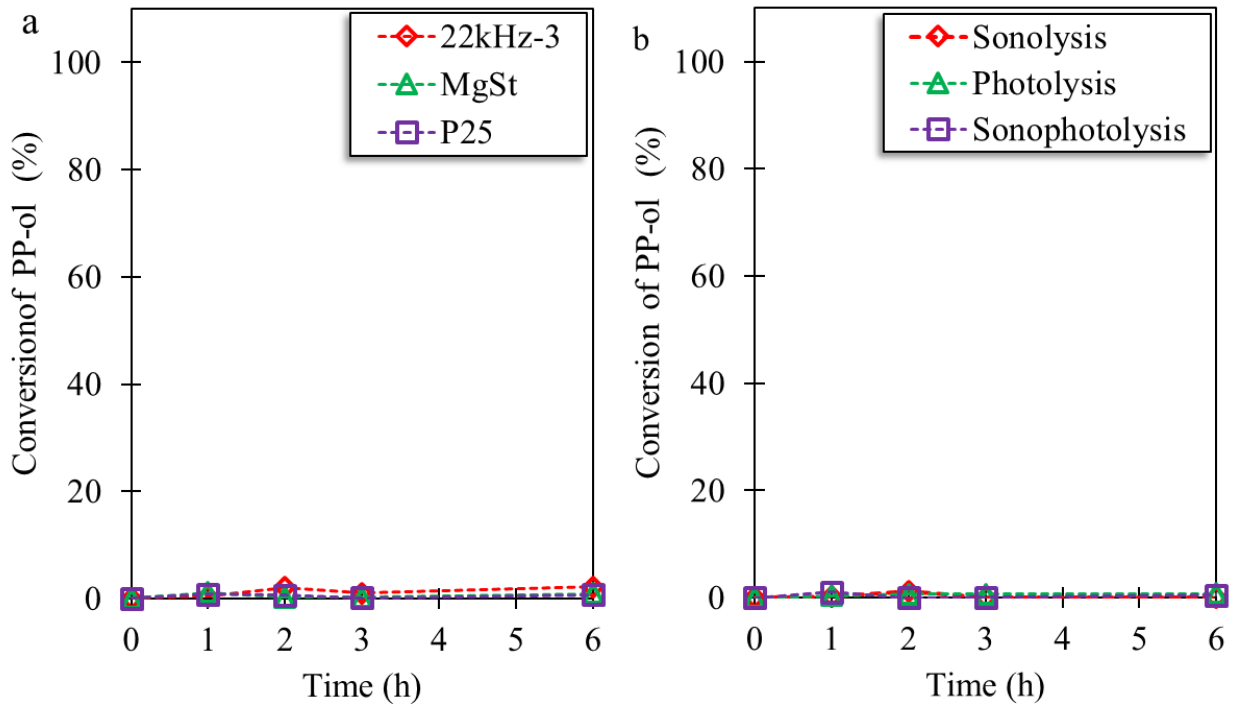

Figure 4.34. Sonocatalytic activity of 22kHz-3, MgSt, and P25 samples for the conversions of PP-ol (a), Control experiments for the sonolysis, photolysis and sonophotolysis (b). (Based on the results of the article submitted to ACS Sustainable Chemistry and Engineering)

4.4.5. Potential pathway studies

To study further insight into the potential origin of these products from the photocatalytic or sonophotocatalytic selective conversion of PP-ol, a series of various reactions using different substrates was studied to find the potential pathways of this reaction. The first possible way is that selective cleavage of β-O-4 can be proceeded by the cleavage of C_α-C_β and C_β-O bond between the two aromatic linkages of PP-ol compound, which can proceed to the formation of different compounds (**Scheme 4.1**). Another possible way is that the photocatalytic oxidation of PP-ol to PP-one and also the direct cleavage of C_α-C_β and C_β-O of PP-ol compound occurs, which leads to the production of Ph-OCHO and Ph-CHO [180–182]. These potential pathways were studied by a series of photocatalytic tests. The photocatalytic activity by using PP-one as a substrate showed that PP-one did not convert into the corresponding products (**Figure 4.35).**

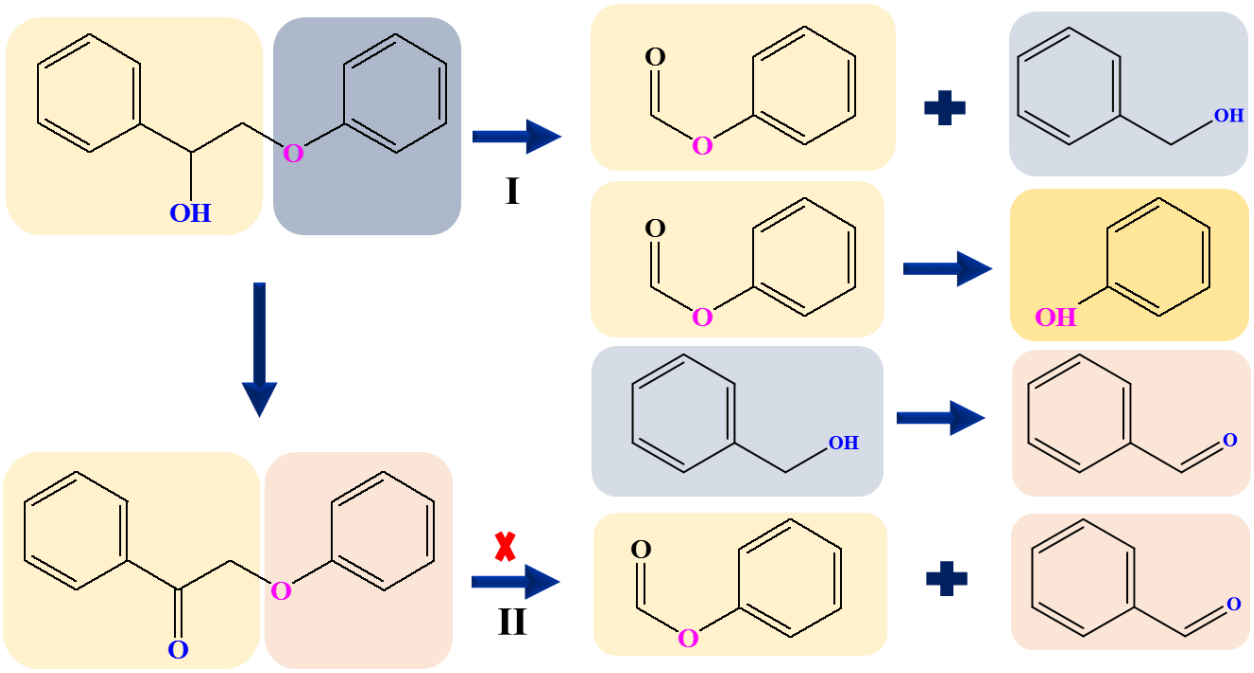

Scheme 4.1. Proposed potential pathway of the formation of various phenolic compounds by photocatalytic conversion of PP-ol. (Modified from the article submitted to ACS Sustainable Chemistry and Engineering)

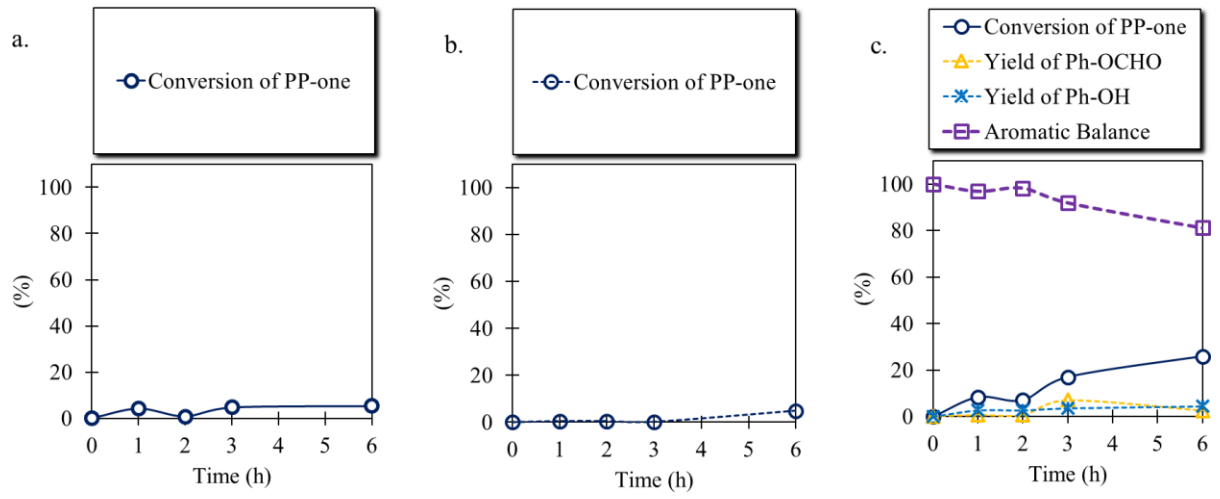

Figure 4.35. Photocatalytic conversion of PP-one by using samples 22kHz-3 (a), MgSt (b) and P25 (c). (Based on the results of the article submitted to ACS Sustainable Chemistry and Engineering)

Thus, these results suggested that PP-one is not an intermediate for the conversion of PP-ol to the corresponding products such as Ph-CHO, Ph-OCHO and Ph-OH. Whereas, photocatalytic studies using Ph-OCHO as a substrate showed that Ph-OCHO converted to Ph-OH (**Figure 4.36**). Additionally, styrallyl alcohol or acetophenone was not identified, which also supported that the selective cleavage of β-O-4 has proceeded via the breakage of C_α-C_β bond.

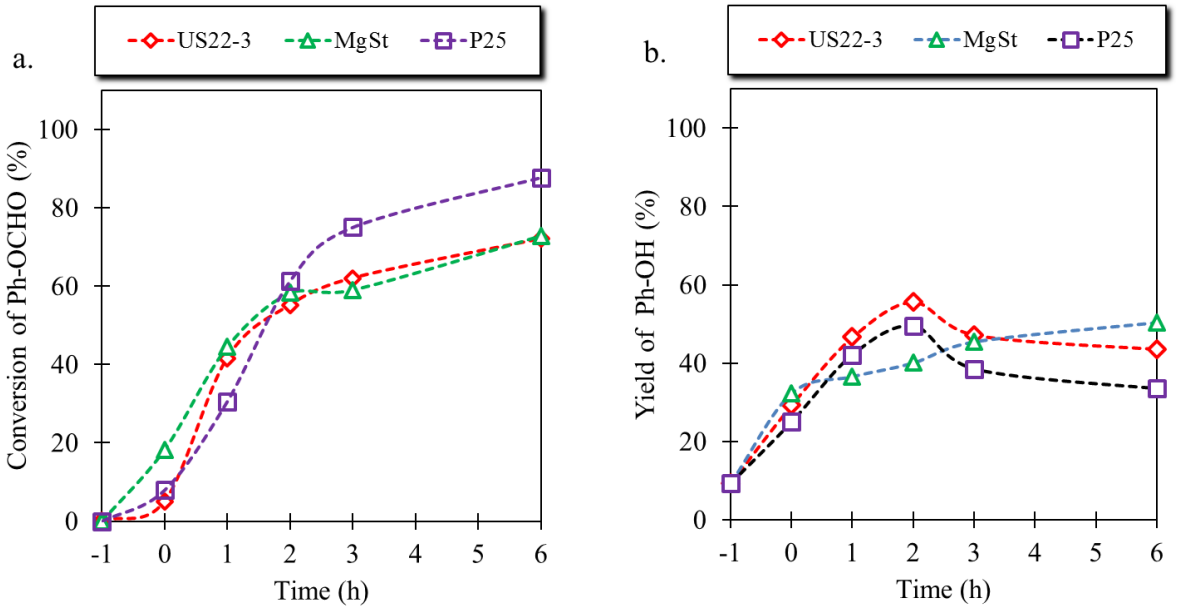

Figure 4.36. Photocatalytic activity of 22kHz-3, MgSt and P25 samples for the conversion of Ph-OCHO (a), yield of Ph-OH (b). (Based on the results of the article submitted to ACS Sustainable Chemistry and Engineering)

4.4.6. Photocatalytic studies of the plausible mechanism for the conversion of PP-ol to the corresponding products

The photocatalysis process is usually governed by active species such as e^-, h^+, OH and $O_2^{\bullet-}$ [183]. It is necessary to understand which active species is the key responsible for the photocatalytic conversion of the PP-ol to the corresponding products. Adding the corresponding scavenger is a good way to study the effect of these active species, and it is widely used in photocatalytic reactions [174,184]. For example, Liang et al., [185] proposed three potential mechanisms for the photocatalytic selective cleavage of C_α-C_β bond of the PP-ol molecule based on the photogenerated h^+ and the singlet oxygen. The scavenger tests were studied for the experimental confirmation of

the role of photogenerated h^+ and singlet oxygen on the photocatalytic conversion of the PP-ol solution. Another researcher, Han et al., [186], also studied the photocatalytic selective oxidation of PP-ol compound by using Ultrathin Metal/CdS, and they found that photogenerated h^+ are responsible for this reaction.

To understand the insight plausible mechanism of the PPol conversion to the corresponding products, a series of photocatalytic experiments were performed by the addition of the chemical scavengers such as $AgNO_3$, KI, t-BtOH and BQ as e^-, h^+, OH and $O_2^{\bullet-}$ scavenger, respectively. The equimolar ratio, such as 1:1 of concentration of the PP-ol and the respective scavenger was used for this study.

The obtained results (**Figure 4.37a,b**) revealed that the addition of KI inhibited the photoactivity of 22kHz-3 and P25 samples for the conversion of PP-ol, while the yield of all the corresponding products was decreased. The addition of $AgNO_3$, t-BtOH, and BQ scavenger did not affect the photoactivity of 22kHz-3 and P25 samples. In the case of 22kHz-3 sample, the yield of Ph-OH using BQ as a scavenger was observed to be higher as compared to the without using any scavenger, which can be potentially linked to the conversion of BQ to the Ph-OH formation on the surface of the sample. These scavengers' studies suggested that the photogenerated h^+ are the most reactive species for the photocatalytic selective cleavage of C_α-C_β bond of the PP-ol molecule using US-assisted synthesized 22kHz-3 sample and commercial P25 sample.

The obtained key products are Ph-CHO, PH-OCHO, Ph-OH and PP-one from the catalytic conversion of PP-ol for all the herein studies samples are the same. The same products suggested that the potential mechanism for the formation of these products is also the same. Therefore, a potential mechanism is proposed in **Scheme 4.2**. As from the scavenger studies, the photogenerated h^+ were found to be the major active species responsible for the transformation. So, at the first step, the C_α-C_β linkage of PP-ol was cleavaged by the attack of the photogenerated h^+ on the $C_{\beta,}$ resulting in the formation of diaromatic and hydrogen radicals. The hydrogen radical reacts with the dissolved molecular oxygen to form the hydrogen superoxide radical (•OOH), which further reacts with the diaromatic radical to form the intermediate complexes. The rearrangement of the intermolecular electron leads to the transfer of e^- from the OH group to the $C_{\alpha,}$ which further leads to the cleavage of the C_α-C_β and O-O bond of $C_{\beta,}$ which results in the

formation of the Ph-CHO and Ph-OCHO. Photocatalytic conversion of Ph-OCHO can lead to the formation of Ph-OH (**Figure 4.36).** A part of PP-ol was also directly oxidized to the PP-one by the photogenerated h^+.

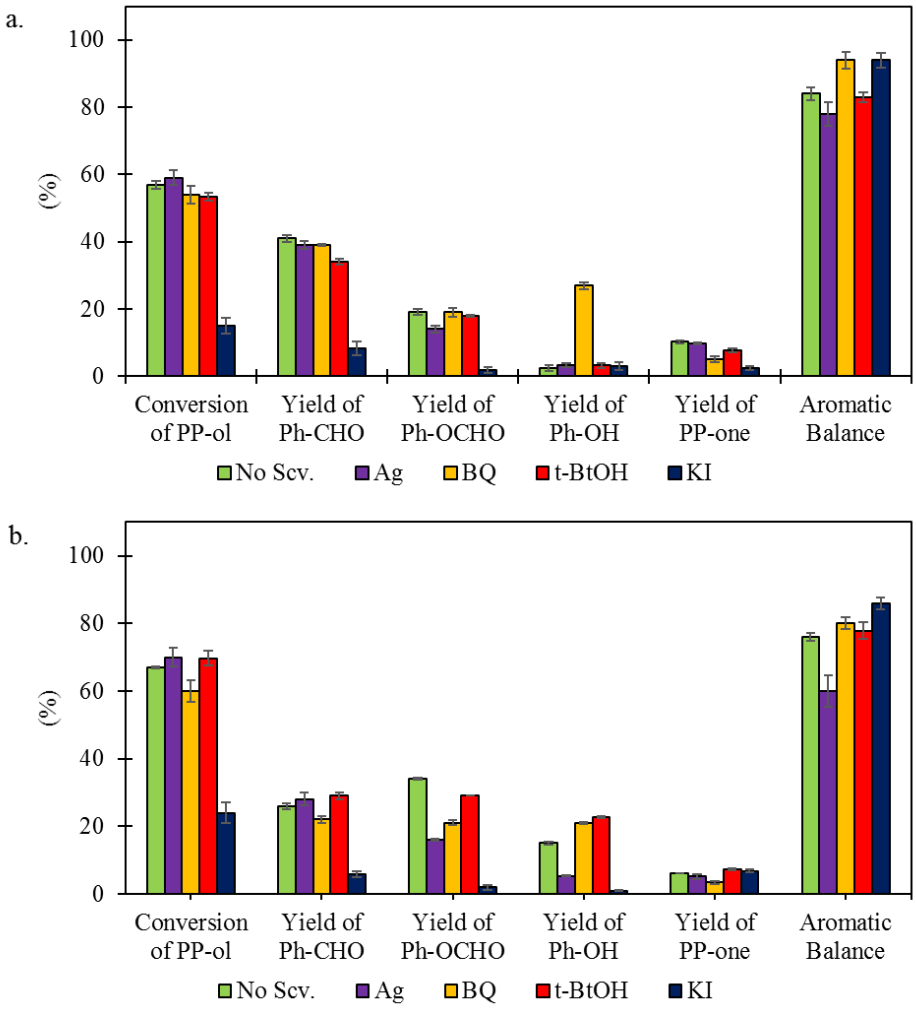

Figure 4.37: Photocatalytic study of 22kHz-3 and P25 samples by the addition of scavengers for various potential active species. (Based on the results of the article submitted to ACS Sustainable Chemistry and Engineering)

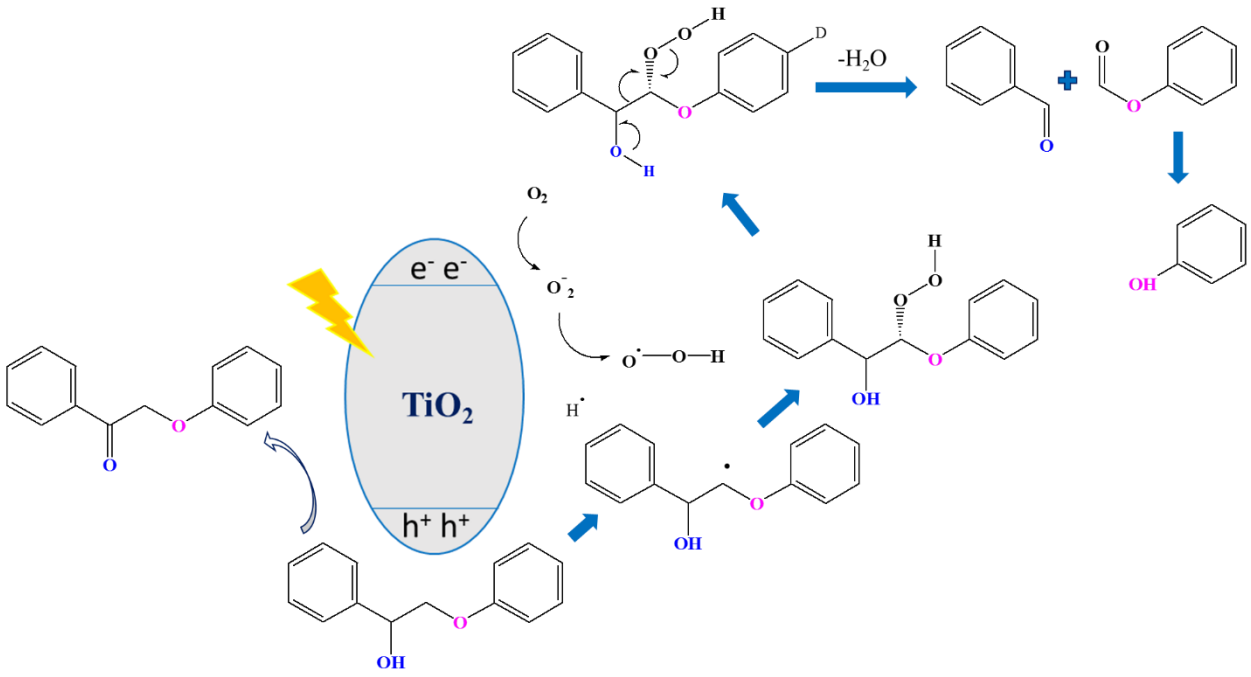

Scheme 4.2: Proposed potential mechanism for the catalytic cleavage of C_{α}-C_{β} bond of PP-ol. (Represented from the article submitted to ACS Sustainable Chemistry and Engineering)

The elevated selective photocatalytic conversion of PP-ol compound using 22kHz-3 sample to the corresponding high-value products is due to various factors. The surface heterogeneity of the 22kHz-3 sample revealed the presence of sodium presenting the basic medium, which can block the acidic groups of the surface of the sample. The higher amount of oxygen species such as C=O, may act as a photosensitizer effect, leading to enhanced penetration of light [143]. The higher amount of hydroxy radicals shown by thermal analysis also facilitates to enhance the catalytic activity [145]. The predominately amorphous phase shown by 22kHz-3 sample also improves the photocatalytic phase as compared to the crystalline sample [144].

The higher textural features, such as higher specific surface area and pore volume distribution as well as the morphology of nanomaterials, also lead to more adsorption of the substrate molecule, resulting in improved photocatalytic activity. The 22kHz-3 sample contained a higher specific surface area 319 m^2/g and pore volume 0.34 cm^3/g than MgSt and P25 samples and this sample also showed the 1-Dimentional nanostructures with the presence of the interlayer spacing, which also a crucial aspect to improve the absorption and enhance penetration of light resulting the higher selective conversion of PP-ol to the corresponding products.

4.4.7. Conclusions of section 4.4

The catalytic selective cleavage of C_α-C_β bond of β-O-4 linkage of lignin-inspired model molecules such as PP-ol was successfully proceeded by the novel synthesized TiO_2 samples to obtain the corresponding products. 22kHz-3 sample revealed a higher yield of the targeted products, such as Ph-CHO, compared to other herein samples. The selected samples were calcined at 500 °C for 5 h to study the effect of calcination on the crystal structure and the photocatalytic performance. The synthesized samples after calcination (22kHz-3 Cal. and MgSt Cal.) samples did not show the elevated yield of the targeted products by the catalytic selective cleavage of C_α-C_β bond of PP-ol, which suggested the elimination of the energy-demanding step during the synthesis of the novel US assisted samples. The coupling of the US with low amplitude to the photocatalytic system instead of magnetic stirring revealed the lowering of the substrate's conversion by keeping the similar yield of the targeted products, which enhanced the selectivity. The key derived results by the sonophotocatalytic studies were the significantly higher aromatic balance of 97 % by 22kHz-3 sample compared to the aromatic balance (84 %) observed by photocatalytic studies. The addition of scavengers for the various active species showed that the photogenerated h^+ are the main active species for the selective catalytic cleavage of the C_α-C_β bond of lignin-based model compounds. Considering all these aspects, a green, cost-effective, and avoiding the energy demanding steps such as using US to synthesize the novel TiO_2-based sample to elevate additive-free selective catalytic performance.

5. Chapter 5: Summary and future perspectives

In the thesis, all the results and the discussion presented that ultrasonication (US) can be used as a green-oriented approach for the synthesis of the nanomaterials by avoiding the energy-demanding approach, such as calcination steps. The major advantages of this utilized approach are that this approach is easy, fast and more economical, through which the formation of any possible side products can be avoided. The utilization of US of different frequencies as well as different amplitudes as the process intensification led to the formation of different nanostructures with elevated or tuned textural and surface heterogeneity features, which are very important for the catalytic process. The US-assisted synthesized photocatalysts by using different frequencies/amplitudes showed a wide deviation in the photocatalytic process, which revealed that the optimization of frequency, as well as the amplitude of utilized US, is a very crucial step to design and synthesize photo-catalyst that can result in the enhanced photocatalytic selective oxidation of lignin-based aromatic alcohols to the potential targeted product by avoiding the formation of any byproducts.

The main conclusions of the PhD thesis and the proposed hypothesis are as follows;

5.1. Outcome of hypothesis 1

The utilization of low-frequency US such as 22 kHz with different amplitudes, which possessed mostly the physical effect of US, results in the formation of novel photocatalysts with tuned physicochemical features. The first outcome was that the utilization of low amplitude of US, leads to more porous materials with elevated specific surface area and total pore volume. The highest textural properties (specific surface area 319 m^2/g and total pore volume (0.34 cm^3/g) and the surface heterogeneity were shown by the sample (22kHz-3), which was synthesized by using 30 µm of 22 kHz of US. The photo-catalysts synthesized using higher amplitudes such as 50, 70 and 90 µm lowered the textural properties. The 22kHz-3 photocatalyst revealed the highest conversion (75 %) of Ph-CH_2OH with 67 % yield of the Ph-CHO as compared to all other 22 kHz US-assisted synthesized samples under the UV light irradiation without the addition of any oxidizing agent. The obtained yield of Ph-CHO was found to be much higher than the sample synthesized without the assistance of US and the commercial P25 photo-catalyst. The physicochemical properties and the results of catalytic activity can be summarised as the proper designing and synthesis of the

nanomaterials for the selective catalytic oxidation of lignin-inspired model compounds is very important. Using US with the optimized amplitude (30 µm) during the synthesis of nanomaterials is considered a prosperous approach for designing a proper catalyst. The utilization of low frequency in the range of sonochemistry, such as 22 kHz, mostly led to the physical effect of US, which can improve the growth of nanostructure.

5.2. Outcome of hypothesis 2

The photocatalysts synthesized using 30 µm of the 22 kHz US showed the highest yield of Ph-CHO by the conversion of Ph-CH_2OH compared to other utilized amplitudes of 22 kHz US. The synthesis of more TiO_2-based catalysts was performed using the 30 µm of higher frequencies (40 and 80 kHz) in the range of physical effect of US. The derived conclusion was that increasing the frequency from 22 to 80 kHz showed a decreasing trend in the textural properties, as well as the higher amplitude of utilized US led to condensed morphology of the synthesized samples. The highest selective yield of Ph-CHO was by sample synthesized using 30 µm of 22 kHz followed by the 40 kHz and 80 kHz US. Also, 70 µm of 40 and 80 kHz US was also used for the synthesis of TiO_2 samples to explore the effect of higher amplitude on the synthesized TiO_2 samples. A similar trend of the photocatalytic performance was observed in the results of the photocatalytic activity of the samples synthesized using 30 µm. The physical phenomena may lead to dispersion mixing and can also control crystal growth by using optimized amplitude. Therefore, it was found by these studies that the optimization of the frequency of US during the synthesis step is ultimately important to design and synthesize the proper photocatalyst for the targeted application.

5.3. Outcome of hypothesis 3

The frequency in the range of 100 kHz to 2 MHz showed the chemical effect of US due to the formation of a large number of small cavitation bubbles. The photocatalysts synthesized by using the two different amplitudes (30 and 70 µm) of 500 kHz US during the synthesis steps led to the formation of different multiphase titanium oxide resembles to nanorods. The low amplitude of higher porous photocatalysts and the formation of the cage of the nanorods like structure result in enhancement of the adsorption of substrate molecule as compared to TiO_2 samples prepared by the high amplitude of 500 kHz. Some nanoclusters were also observed on the outer layers of both US-assisted synthesized samples, which may lead to improving the light penetration, and also the

surface compositions were also observed to be altered. The 500kHz-3 photocatalyst samples showed higher additive-free photocatalytic partial selective oxidation of Ph-CH_2OH to Ph-CHO as compared to silent conditions synthesized photocatalyst and P25 sample. Whereas 500kHz-7 did not show photocatalytic performance due to the condensed arrangement of the nanostructures. It was found that using different amplitudes of high-frequency US leads to altering the physiochemical properties and photocatalytic performance.

5.4. Outcome of hypothesis 4

The photo-catalysts (22kHz-3) synthesized using the low amplitude 30 µm of 22 kHz showed the highest photocatalytic conversion of Ph-CH_2OH to Ph-CHO as compared to all other herein studied TiO_2 samples. 22kHz-3 along non-US assisted synthesized MgSt sample and commercial P25 sample was also studied for the photocatalytic conversion of lignin-inspired model molecules such as PP-ol, and it was found that 22kHz-3 sample showed the highest yield of the products such as Ph-CHO, Ph-OCHO and PP-one with the higher aromatic balance compared to other herein studies samples. It was also hypothesized that the US-assisted synthesis approach led to more active and selective photocatalysts by avoiding the energy-demanding step due to the cavitation phenomenon. So, the herein-studied photocatalysts were calcinated at 500 °C for 5 h, followed by the study of photocatalytic performance. As it was found that the 22kHz-3 sample possessed more anatase phase after calcination, but the 22kHz-3 without calcination showed better photocatalytic selective activity compared to the calcined samples. Also, the reusability of the herein-studied samples was also explored up to the fifth runs of photocatalytic experiments. All the samples were found stable without losing the photocatalytic activity, and no leaching of Ti was observed after the fifth run by the EDXRF. The sonophotocatalytic studies showed that 22kHz-3 sample revealed the elevated sonophotocatalytic selective cleavage of C_α-C_β bond of PP-ol led to enhanced aromaticity of the reaction as compared to the photocatalytic studies. A series of photocatalytic experiments by the addition of scavengers found the photogenerated h^+ to be the main reactive species, which led to an understanding of the potential mechanism for the photocatalytic conversion of PP-ol to the corresponding products.

5.5. Future perspectives

The present research work was focused on novel synthesis of metal oxide-based nanomaterials, and specifically titanium oxide ones, using a "green" approach by taking advantage of sonochemistry that is economic and easy to be performed. The use of sonication after during the synthesis of nanomaterials after optimization of frequency and amplitude exhibited very interesting outcomes in terms of the final material's physiochemical features. The photocatalytic activity was also affected positively in the case of the selective conversion of lignin-based model compounds to the corresponding high-value phenolic compounds. However, there are ample opportunities for further research on improving and tuning the materials design protocol and transfer the obtained knowledge toward the design and synthesis of other metal oxides or mixed metal oxides. As well as composites utilizing low-energy sonication. In addition, further studies can be focused on improving the photocatalytic conversion of lignin derived/inspired aromatics using sunlight irradiation.

Furthermore, photocatalytic studies for the real lignin-based waste materials from the pulp and paper industries is also an interesting research task that can be explored. The photocatalytic and sonophotocatalytic studies in the current research work were carried out by establishing batch reactors and using the suspension of the catalyst in the targeted substrate solution. Further alternative strategies, such as catalyst's immobilization on desired substrates or coating the interior walls of microreactors in order to achieve continuous flow configurations can be explored in the future. The designing of the flow catalytic reactor for the flow photo(sono)catalytic can also be studied in future.

6. Bibliography

[1] C.W. Lahive, P.C.J. Kamer, C.S. Lancefield, P.J. Deuss, An Introduction to Model Compounds of Lignin Linking Motifs; Synthesis and Selection Considerations for Reactivity Studies, ChemSusChem. 13 (2020) 4238–4265. https://doi.org/10.1002/cssc.202000989.

[2] T. Ročnik, B. Likozar, E. Jasiukaitytė-Grojzdek, M. Grilc, Catalytic lignin valorisation by depolymerisation, hydrogenation, demethylation and hydrodeoxygenation: Mechanism, chemical reaction kinetics and transport phenomena, Chem. Eng. J. 448 (2022). https://doi.org/10.1016/j.cej.2022.137309.

[3] R. Rinaldi, R. Jastrzebski, M.T. Clough, J. Ralph, M. Kennema, P.C.A. Bruijnincx, B.M. Weckhuysen, Paving the Way for Lignin Valorisation: Recent Advances in Bioengineering, Biorefining and Catalysis, Angew. Chemie - Int. Ed. 55 (2016) 8164–8215. https://doi.org/10.1002/anie.201510351.

[4] C. Li, X. Zhao, A. Wang, G.W. Huber, T. Zhang, Catalytic Transformation of Lignin for the Production of Chemicals and Fuels, Chem. Rev. 115 (2015) 11559–11624. https://doi.org/10.1021/acs.chemrev.5b00155.

[5] Y. Pu, S. Cao, A.J. Ragauskas, Application of quantitative 31P NMR in biomass lignin and biofuel precursors characterization, Energy Environ. Sci. 4 (2011) 3154–3166. https://doi.org/10.1039/c1ee01201k.

[6] F. Wang, D. Ouyang, Z. Zhou, S.J. Page, D. Liu, X. Zhao, Lignocellulosic biomass as sustainable feedstock and materials for power generation and energy storage, J. Energy Chem. 57 (2021) 247–280. https://doi.org/10.1016/j.jechem.2020.08.060.

[7] M.M. Abu-Omar, K. Barta, G.T. Beckham, J.S. Luterbacher, J. Ralph, R. Rinaldi, Y. Román-Leshkov, J.S.M. Samec, B.F. Sels, F. Wang, Guidelines for performing lignin-first biorefining, Energy Environ. Sci. 14 (2021) 262–292. https://doi.org/10.1039/d0ee02870c.

[8] J. Ralph, C. Lapierre, W. Boerjan, Lignin structure and its engineering, Curr. Opin. Biotechnol. 56 (2019) 240–249. https://doi.org/10.1016/j.copbio.2019.02.019.

[9] D.S. Bajwa, G. Pourhashem, A.H. Ullah, S.G. Bajwa, A concise review of current lignin production, applications, products and their environment impact, Ind. Crops Prod. 139 (2019) 111526. https://doi.org/10.1016/j.indcrop.2019.111526.

[10] H. Luo, M.M. Abu-Omar, Chemicals From Lignin, in: Encycl. Sustain. Technol., 2017: pp. 573–585. https://doi.org/10.1016/B978-0-12-409548-9.10235-0.

[11] M. Chen, Y. Li, H. Liu, D. Zhang, Q.S. Shi, X.Q. Zhong, Y. Guo, X.B. Xie, High value valorization of lignin as environmental benign antimicrobial, Mater. Today Bio. 18 (2023) 100520. https://doi.org/10.1016/j.mtbio.2022.100520.

[12] W. Deng, Y. Feng, J. Fu, H. Guo, Y. Guo, B. Han, Z. Jiang, L. Kong, C. Li, H. Liu, P.T.T. Nguyen, P. Ren, F. Wang, S. Wang, Y. Wang, Y. Wang, S.S. Wong, K. Yan, N. Yan, X. Yang, Y. Zhang, Z. Zhang, X. Zeng, H. Zhou, Catalytic conversion of lignocellulosic biomass into chemicals and fuels, Green Energy Environ. 8 (2022) 10–114. https://doi.org/10.1016/j.gee.2022.07.003.

[13] M. Ullah, P. Liu, S. Xie, S. Sun, Recent Advancements and Challenges in Lignin Valorization: Green Routes towards Sustainable Bioproducts, Molecules. 27 (2022). https://doi.org/10.3390/molecules27186055.

[14] Y. Sheng, Y. Xu, Nuclear magnetic resonance analysis of ascorbic acid assisted lignocellulose decomposition in dilute acid pretreatment and its stimulation on enzymatic hydrolysis, Bioresour. Technol. 343 (2022) 126147. https://doi.org/10.1016/j.biortech.2021.126147.

[15] J. Novakovic, N. Kontogianni, E.M. Barampouti, S. Mai, K. Moustakas, D. Malamis, M. Loizidou, Towards upscaling the valorization of wheat straw residues: alkaline pretreatment using sodium hydroxide, enzymatic hydrolysis and biogas production, Environ. Sci. Pollut. Res. 28 (2021) 24486–24498. https://doi.org/10.1007/s11356-020-08905-y.

[16] N. Srivastava, R. Singh, M. Srivastava, A. Syed, D. Bahadur Pal, A.H. Bahkali, P.K. Mishra, V.K. Gupta, Impact of mixed lignocellulosic substrate and fungal consortia to enhance cellulase production and its application in NiFe2O4 nanoparticles mediated

enzymatic hydrolysis of wheat straw, Bioresour. Technol. 345 (2022) 126560. https://doi.org/10.1016/j.biortech.2021.126560.

[17] H. Zhang, L. Han, H. Dong, An insight to pretreatment, enzyme adsorption and enzymatic hydrolysis of lignocellulosic biomass: Experimental and modeling studies, Renew. Sustain. Energy Rev. 140 (2021) 110758. https://doi.org/10.1016/j.rser.2021.110758.

[18] M. Paul, N.K. Pandey, A. Banerjee, G.K. Shroti, P. Tomer, R.K. Gazara, H. Thatoi, T. Bhaskar, S. Hazra, D. Ghosh, An insight into omics analysis and metabolic pathway engineering of lignin-degrading enzymes for enhanced lignin valorization, Bioresour. Technol. (2023) 129045. https://doi.org/10.1016/j.biortech.2023.129045.

[19] A. Margellou, K.S. Triantafyllidis, Catalytic Transfer Hydrogenolysis Reactions for Lignin Valorization to Fuels and Chemicals, Catalysts. 9 (2019) 1–31. https://doi.org/10.3390/catal9010043.

[20] G. Zhu, X. Ouyang, L. Jiang, Y. Zhu, D. Jin, Y. Pang, X. Qiu, Effect of functional groups on hydrogenolysis of lignin model compounds, Fuel Process. Technol. 154 (2016) 132–138. https://doi.org/10.1016/j.fuproc.2016.08.023.

[21] K. Ye, Y. Liu, S. Wu, J. Zhuang, A review for lignin valorization: Challenges and perspectives in catalytic hydrogenolysis, Ind. Crops Prod. 172 (2021). https://doi.org/10.1016/j.indcrop.2021.114008.

[22] H. Wang, Y. Pu, A. Ragauskas, B. Yang, From lignin to valuable products–strategies, challenges, and prospects, Bioresour. Technol. 271 (2019) 449–461. https://doi.org/10.1016/j.biortech.2018.09.072.

[23] C. Xu, R.A.D. Arancon, J. Labidi, R. Luque, Lignin depolymerisation strategies: Towards valuable chemicals and fuels, Chem. Soc. Rev. 43 (2014) 7485–7500. https://doi.org/10.1039/c4cs00235k.

[24] S. Ryu, H.W. Lee, Y.M. Kim, J. Jae, S.C. Jung, J.M. Ha, Y.K. Park, Catalytic fast co-pyrolysis of organosolv lignin and polypropylene over in-situ red mud and ex-situ HZSM-5 in two-step catalytic micro reactor, Appl. Surf. Sci. 511 (2020) 145521.

https://doi.org/10.1016/j.apsusc.2020.145521.

[25] M.B. Figueirêdo, I. Hita, P.J. Deuss, R.H. Venderbosch, H.J. Heeres, Pyrolytic lignin: a promising biorefinery feedstock for the production of fuels and valuable chemicals, Green Chem. 24 (2022) 4680–4702. https://doi.org/10.1039/d2gc00302c.

[26] C.H. Lam, W. Deng, L. Lang, X. Jin, X. Hu, Y. Wang, Minireview on Bio-Oil Upgrading via Electrocatalytic Hydrogenation: Connecting Biofuel Production with Renewable Power, Energy and Fuels. 34 (2020) 7915–7928. https://doi.org/10.1021/acs.energyfuels.0c01380.

[27] W. Schutyser, T. Renders, S. Van Den Bosch, S.F. Koelewijn, G.T. Beckham, B.F. Sels, Chemicals from lignin: An interplay of lignocellulose fractionation, depolymerisation, and upgrading, Chem. Soc. Rev. 47 (2018) 852–908. https://doi.org/10.1039/c7cs00566k.

[28] O.Y. Abdelaziz, I. Clemmensen, S. Meier, C.A.E. Costa, A.E. Rodrigues, C.P. Hulteberg, A. Riisager, On the Oxidative Valorization of Lignin to High-Value Chemicals: A Critical Review of Opportunities and Challenges, ChemSusChem. 15 (2022). https://doi.org/10.1002/cssc.202201232.

[29] J. Zakzeski, P.C.A. Bruijnincx, A.L. Jongerius, B.M. Weckhuysen, The catalytic valorization of lignin for the production of renewable chemicals, Chem. Rev. 110 (2010) 3552–3599. https://doi.org/10.1021/cr900354u.

[30] H. Lange, S. Decina, C. Crestini, Oxidative upgrade of lignin - Recent routes reviewed, Eur. Polym. J. 49 (2013) 1151–1173. https://doi.org/10.1016/j.eurpolymj.2013.03.002.

[31] Z. Chen, Y. Wang, H. Cheng, H. Zhou, Integrated chemo- and biocatalytic processes: a new fashion toward renewable chemicals production from lignocellulosic biomass, J. Chem. Technol. Biotechnol. 98 (2023) 331–345. https://doi.org/10.1002/jctb.7241.

[32] R. Behling, S. Valange, G. Chatel, Heterogeneous catalytic oxidation for lignin valorization into valuable chemicals: What results? What limitations? What trends?, Green Chem. 18 (2016) 1839–1854. https://doi.org/10.1039/c5gc03061g.

[33] Fujishima Akira and Kenichi Honda., Electrochemical Photolysis of Water at a

Semiconductor Electrode, Nature. 238 (1972) 38–38.

[34] D.A.H. Hanaor, C.C. Sorrell, Review of the anatase to rutile phase transformation, J. Mater. Sci. 46 (2011) 855–874. https://doi.org/10.1007/s10853-010-5113-0.

[35] C. Byrne, R. Fagan, S. Hinder, D.E. McCormack, S.C. Pillai, New approach of modifying the anatase to rutile transition temperature in TiO2 photocatalysts, RSC Adv. 6 (2016) 95232–95238. https://doi.org/10.1039/c6ra19759k.

[36] A.L. Stepanov, X. Xiao, F. Ren, Implantation of titanium dioxide with transition metalions, Titan. Dioxide Appl. Synth. Toxic. (2013) 59–84.

[37] M.K. Singh, M.S. Mehata, Phase-dependent optical and photocatalytic performance of synthesized titanium dioxide (TiO2) nanoparticles, Optik (Stuttg). 193 (2019) 163011. https://doi.org/10.1016/j.ijleo.2019.163011.

[38] T. Luttrell, S. Halpegamage, J. Tao, A. Kramer, E. Sutter, M. Batzill, Why is anatase a better photocatalyst than rutile? - Model studies on epitaxial TiO2 films, Sci. Rep. 4 (2015) 1–8. https://doi.org/10.1038/srep04043.

[39] M. Xu, Y. Gao, E.M. Moreno, M. Kunst, M. Muhler, Y. Wang, H. Idriss, C. Wöll, Photocatalytic activity of bulk TiO2 anatase and rutile single crystals using infrared absorption spectroscopy, Phys. Rev. Lett. 106 (2011) 1–4. https://doi.org/10.1103/PhysRevLett.106.138302.

[40] K. Tanaka, M.F.V. Capule, T. Hisanaga, Effect of crystallinity of TiO2 on its photocatalytic action, Chem. Phys. Lett. 187 (1991) 73–76. https://doi.org/10.1016/0009-2614(91)90486-S.

[41] W.J. Yin, B. Wen, C. Zhou, A. Selloni, L.M. Liu, Excess electrons in reduced rutile and anatase TiO2, Surf. Sci. Rep. 73 (2018) 58–82. https://doi.org/10.1016/j.surfrep.2018.02.003.

[42] L. Hu, W., Li, L., Li, G., Tang, C., & Sun, High-quality brookite TiO2 flowers: synthesis, characterization, and dielectric performance, Cryst. Growth Des. 9 (2009) 3676–3682.

[43] H. Kominami, M. Kohno, Y. Kera, Synthesis of brookite-type titanium oxide nano-crystals in organic media, J. Mater. Chem. 10 (2000) 1151–1156. https://doi.org/10.1039/a908528i.

[44] A. Di Paola, M. Bellardita, L. Palmisano, Brookite, the least known TiO2 photocatalyst, in: Catalysts, 2013: pp. 36–73. https://doi.org/10.3390/catal3010036.

[45] T.A. Kandiel, A. Feldhoff, L. Robben, R. Dillert, D.W. Bahnemann, Tailored titanium dioxide nanomaterials: anatase nanoparticles and brookite nanorods as highly active photocatalysts, Chem. Mater. 22 (2010) 2050–2060. https://doi.org/10.1021/cm903472p.

[46] Z. Li, S. Cong, Y. Xu, Brookite vs anatase TiO2 in the photocatalytic activity for organic degradation in water, ACS Catal. 4 (2014) 3273–3280. https://doi.org/10.1021/cs500785z.

[47] M. Lal, P. Sharma, C. Ram, Synthesis and photocatalytic potential of Nd-doped TiO2 under UV and solar light irradiation using a sol-gel ultrasonication method, Results Mater. 15 (2022) 100308. https://doi.org/10.1016/j.rinma.2022.100308.

[48] S.H. Soytaş, O. Oğuz, Y.Z. Menceloğlu, Polymer Nanocomposites With Decorated Metal Oxides, in: Polym. Compos. with Funct. Nanoparticles Synth. Prop. Appl., 2018: pp. 287–323. https://doi.org/10.1016/B978-0-12-814064-2.00009-3.

[49] S. Mathew Simon, G. George, S. M S, P. V P, T. Anna Jose, P. Vasudevan, A.C. Saritha, P.R. Biju, C. Joseph, N. V. Unnikrishnan, Recent advancements in multifunctional applications of sol-gel derived polymer incorporated TiO2-ZrO2 composite coatings: A comprehensive review, Appl. Surf. Sci. Adv. 6 (2021) 100173. https://doi.org/10.1016/j.apsadv.2021.100173.

[50] F.E. Bortot Coelho, G. Magnacca, V. Boffa, V.M. Candelario, M. Luiten-Olieman, W. Zhang, From ultra to nanofiltration: A review on the fabrication of ZrO2 membranes, Ceram. Int. 49 (2023) 8683–8708. https://doi.org/10.1016/j.ceramint.2023.01.076.

[51] F. Ciesielczyk, M. Przybysz, J. Zdarta, A. Piasecki, D. Paukszta, T. Jesionowski, The sol-gel approach as a method of synthesis of xMgO·ySiO 2 powder with defined physicochemical properties including crystalline structure, J. Sol-Gel Sci. Technol. 71 (2014) 501–513. https://doi.org/10.1007/s10971-014-3398-1.

[52] T. Gupta, Samriti, J. Cho, J. Prakash, Hydrothermal synthesis of TiO2 nanorods: formation chemistry, growth mechanism, and tailoring of surface properties for photocatalytic activities, Mater. Today Chem. 20 (2021) 100428. https://doi.org/10.1016/j.mtchem.2021.100428.

[53] N. Liu, X. Chen, J. Zhang, J.W. Schwank, A review on TiO2-based nanotubes synthesized via hydrothermal method: Formation mechanism, structure modification, and photocatalytic applications, Catal. Today. 225 (2014) 34–51. https://doi.org/10.1016/j.cattod.2013.10.090.

[54] B. Gomathi Thanga Keerthana, T. Solaiyammal, S. Muniyappan, P. Murugakoothan, Hydrothermal synthesis and characterization of TiO2 nanostructures prepared using different solvents, Mater. Lett. 220 (2018) 20–23. https://doi.org/10.1016/j.matlet.2018.02.119.

[55] M.T. Munir, S.S. Mansouri, I.A. Udugama, S. Baroutian, K. V. Gernaey, B.R. Young, Resource recovery from organic solid waste using hydrothermal processing: Opportunities and challenges, Renew. Sustain. Energy Rev. 96 (2018) 64–75. https://doi.org/10.1016/j.rser.2018.07.039.

[56] R. Singaravelan, S. Bangaru Sudarsan Alwar, Electrochemical synthesis, characterisation and phytogenic properties of silver nanoparticles, Appl. Nanosci. 5 (2015) 983–991. https://doi.org/10.1007/s13204-014-0396-0.

[57] D. Eisenberg, H.S. Ahn, A.J. Bard, Enhanced photoelectrochemical water oxidation on bismuth vanadate by electrodeposition of amorphous titanium dioxide, J. Am. Chem. Soc. 136 (2014) 14011–14014. https://doi.org/10.1021/ja5082475.

[58] Y. Zhao, Y. Hu, Y. Li, H. Zhang, S. Zhang, L. Qu, G. Shi, L. Dai, Super-long aligned TiO2/carbon nanotube arrays, Nanotechnology. 21 (2010). https://doi.org/10.1088/0957-4484/21/50/505702.

[59] B. Endrődi, E. Kecsenovity, K. Rajeshwar, C. Janáky, One-Step Electrodeposition of Nanocrystalline TiO2 Films with Enhanced Photoelectrochemical Performance and Charge Storage, ACS Appl. Energy Mater. 1 (2018) 851–858.

https://doi.org/10.1021/acsaem.7b00289.

[60] D. Bijou, E. Wagner, W. Maudez, T. Cornier, M. Yettou, G. Benvenuti, S. Daniele, Study of titanium amino-alkoxide derivatives as TiO2 Chemical Beam Vapour Deposition precursor, Mater. Chem. Phys. 277 (2022). https://doi.org/10.1016/j.matchemphys.2021.125561.

[61] J. Carlsson, P.M. Martin, Chemical Vapor Deposition, in: Handb. Depos. Technol. Film. Coatings, Third Edit, 2010: pp. 314–363. https://doi.org/10.1016/B978-0-8155-2031-3.00007-7.

[62] G.L. Doll, B.A. Mensah, H. Mohseni, T.W. Scharf, Chemical Vapor Deposition and Atomic Layer Deposition of Coatings for Mechanical Applications, J. Therm. Spray Technol. 19 (2010) 510–516. https://doi.org/10.1007/s11666-009-9364-8.

[63] J. Wu, T. Zhang, Large-Scale Preparation of Ordered Titania Nanorods with Enhanced Photocatalytic Activity, Langmuir. (2005) 6995–7002.

[64] J. Wu, S. Hayakawa, K. Tsuru, A. Osaka, Porous titania ® lms prepared from interactions of titanium with hydrogen peroxide solution, Scr. Mater. 46. 46 (2002) 101–106.

[65] H.P. Hernández, A.P. Moreno, C.R.S. Castillo, Ecological Drawbacks of Nanomaterials Produced on an Industrial Scale : Collateral Effect on Human and Environmental Health, in: Water, Air, Soil Pollut., 2021. https://doi.org/10.1007/s11270-021-05370-2.

[66] J. Guo, J. Li, H. Kou, Advanced Ceramic Materials, in: Mod. Inorg. Synth. Chem., 2017: pp. 463–492. https://doi.org/10.1016/B978-0-444-63591-4.00017-3.

[67] B. Sinha, R.H. Müller, J.P. Möschwitzer, Bottom-up approaches for preparing drug nanocrystals: Formulations and factors affecting particle size, Int. J. Pharm. (2022). https://doi.org/10.1016/j.ijpharm.2013.01.019.

[68] S.M. Gupta, M. Tripathi, A review on the synthesis of TiO 2 nanoparticles by solution route, Cent. Eur. J. Chem. A. 10 (2012) 279–294. https://doi.org/10.2478/s11532-011-0155-y.

[69] M.A. Willard, L.K. Kurihara, E.E. Carpenter, S. Calvin, V.G. Harris, L.K. Kurihara, E.E. Carpenter, S. Calvin, V.G. Harris, M.A. Willard, L.K. Kurihara, E.E. Carpenter, S. Calvin, V.G. Harris, Chemically prepared magnetic nanoparticles, Int. Mater. Rev. ISSN. 49 (2013) 125–170. https://doi.org/10.1179/095066004225021882.

[70] D.A. Giannakoudakis, A. Qayyum, D. Łomot, M.O. Besenhard, D. Lisovytskiy, T.J. Bandosz, J.C. Colmenares, Boosting the Photoactivity of Grafted Titania: Ultrasound-Driven Synthesis of a Multi-Phase Heterogeneous Nano-Architected Photocatalyst, Adv. Funct. Mater. 31 (2021) 2007115. https://doi.org/10.1002/adfm.202007115.

[71] R.B.N. Baig, R.S. Varma, Alternative energy input: Mechanochemical, microwave and ultrasound-assisted organic synthesis, Chem. Soc. Rev. 41 (2012) 1559–1584. https://doi.org/10.1039/c1cs15204a.

[72] G. Chatel, J.C. Colmenares, Sonochemistry: from Basic Principles to Innovative Applications, Top. Curr. Chem. 375 (2017) 8. https://doi.org/10.1007/s41061-016-0096-1.

[73] Basak Savun-Hekimoglu, A Review on Sonochemistry and Its Environmental Applications, Acoustics. 2 (2020) 766–775.

[74] T.G. Mckenzie, F. Karimi, G.G.Q. Ashokkumar, Muthupandian, Ultrasound and Sonochemistry for Radical Polymerization : Sound Synthesis, Chem. Eur. J. 25 (2019) 5372–5388. https://doi.org/10.1002/chem.201803771.

[75] S. Price, J. Gareth , Suslick, Kenneth, Applications of ultrasound to materials chemistry., Annu. Rev. Mater. Sci. 29 (1999) 295–326.

[76] K.S. Suslick, The Chemical Effects of Ultrasound, Sci. Am. 260 (1989) 80–86. https://doi.org/10.1038/scientificamerican0289-80.

[77] J.C. Colmenares Q., Ultrasound and Photochemical Procedures for Nanocatalysts Preparation: Application in Photocatalytic Biomass Valorization, J. Nanosci. Nanotechnol. 13 (2013) 4787–4798.

[78] Z. Li, J. Dong, L. Wang, Y. Zhang, T. Zhuang, H. Wang, X. Cui, Z. Wang, A power-

triggered preparation strategy of nano-structured inorganics: Sonosynthesis, Nanoscale Adv. 3 (2021) 2423–2447. https://doi.org/10.1039/d1na00038a.

[79] T.G. McKenzie, F. Karimi, M. Ashokkumar, G.G. Qiao, Ultrasound and Sonochemistry for Radical Polymerization: Sound Synthesis, Chem. - A Eur. J. 25 (2019) 5372–5388. https://doi.org/10.1002/chem.201803771.

[80] P.N. Amaniampong, F. Jérôme, Catalysis under ultrasonic irradiation: a sound synergy, Curr. Opin. Green Sustain. Chem. 22 (2020) 7–12. https://doi.org/10.1016/j.cogsc.2019.11.002.

[81] G. Cravotto, P. Cintas, Harnessing mechanochemical effects with ultrasound-induced reactions, Chem. Sci. 3 (2012) 295–307. https://doi.org/10.1039/c1sc00740h.

[82] A. Brotchie, F. Grieser, M. Ashokkumar, Effect of power and frequency on bubble-size distributions in acoustic cavitation, Phys. Rev. Lett. 102 (2009) 1–4. https://doi.org/10.1103/PhysRevLett.102.084302.

[83] S. Merouani, O. Hamdaoui, Y. Rezgui, M. Guemini, Effects of ultrasound frequency and acoustic amplitude on the size of sonochemically active bubbles-Theoretical study, Ultrason. Sonochem. 20 (2013) 815–819. https://doi.org/10.1016/j.ultsonch.2012.10.015.

[84] L. Santos-Zea, M. Antunes-Ricardo, J.A. Gutierrez-Uribe, J. V. García-Pérez, J. Benedito, Effect of ultrasound transducer design on the acoustically-assisted supercritical fluid extraction of antioxidants from oregano, Ultrason. Sonochem. 47 (2018) 47–56. https://doi.org/10.1016/j.ultsonch.2018.04.019.

[85] Y. Son, M. Lim, M. Ashokkumar, J. Khim, Geometric optimization of sonoreactors for the enhancement of sonochemical activity, J. Phys. Chem. C. 115 (2011) 4096–4103. https://doi.org/10.1021/jp110319y.

[86] T.J. Mason, J.P. Lorimer, Applied Sonochemistry, Appl. Sonochemistry. (2002). https://doi.org/10.1002/352760054x.

[87] F. Chemat, N. Rombaut, A.G. Sicaire, A. Meullemiestre, A.S. Fabiano-Tixier, M. Abert-

Vian, Ultrasound assisted extraction of food and natural products. Mechanisms, techniques, combinations, protocols and applications. A review, Ultrason. Sonochem. 34 (2017) 540–560. https://doi.org/10.1016/j.ultsonch.2016.06.035.

[88] D.J. Flannigan, K.S. Suslick, Inertially confined plasma in an imploding bubble, Nat. Phys. 6 (2010) 598–601. https://doi.org/10.1038/nphys1701.

[89] D.G. Shchukin, H. Möhwald, Sonochemical nanosynthesis at the engineered interface of a cavitation microbubble, Phys. Chem. Chem. Phys. 8 (2006) 3496–3506. https://doi.org/10.1039/b606104d.

[90] M.A. Almessiere, Y. Slimani, U. Kurtan, S. Guner, M. Sertkol, S.E. Shirsath, S. Akhtar, A. Baykal, I. Ercan, Structural, magnetic, optical properties and cation distribution of nanosized Co0.7Zn0.3TmxFe2−xO4 ($0.0 \leq x \leq 0.04$) spinel ferrites synthesized by ultrasonic irradiation, Ultrason. Sonochem. 58 (2019) 104638. https://doi.org/10.1016/j.ultsonch.2019.104638.

[91] M.H. Entezari, P. Kruus, R. Otson, The effect of frequency on sonochemical reactions III: Dissociation of carbon disulfide, Ultrason. Sonochem. 4 (1997) 49–54. https://doi.org/10.1016/S1350-4177(96)00016-8.

[92] B.K. Kang, M.S. Kim, J.G. Park, Effect of dissolved gases in water on acoustic cavitation and bubble growth rate in 0.83 MHz megasonic of interest to wafer cleaning, Ultrason. Sonochem. 21 (2014) 1496–1503. https://doi.org/10.1016/j.ultsonch.2014.01.012.

[93] P. Huang, S. Zhao, H. Bachman, N. Nama, Z. Li, C. Chen, S. Yang, M. Wu, S.P. Zhang, T.J. Huang, Acoustofluidic Synthesis of Particulate Nanomaterials, Adv. Sci. 6 (2019) 1900913. https://doi.org/10.1002/advs.201900913.

[94] N. Pokhrel, P.K. Vabbina, N. Pala, Ultrasonics Sonochemistry Sonochemistry : Science and Engineering, Ultrason. Sonochem. 29 (2016) 104–128. https://doi.org/10.1016/j.ultsonch.2015.07.023.

[95] A. Tezel, S. Mitragotri, Interactions of Inertial Cavitation Bubbles with Stratum Corneum Lipid Bilayers during Low-Frequency Sonophoresis, Biophys. J. 85 (2003) 3502–3512.

https://doi.org/10.1016/S0006-3495(03)74770-5.

[96] W. Lauterborn, C. Ohl, Cavitation bubble dynamics Werner, Ultrason. Sonochemistry 4. 4 (1997) 65–75.

[97] K.S. Suslick, Sonochemistry, in: Forth Edit, New York, n.d.: pp. 516–541.

[98] L. Zhang, V. Belova, H. Wang, W. Dong, Controlled Cavitation at Nano/Microparticle Surfaces, Chem. Mater. 26 (2014) 2244–2248.

[99] H. Xu, B.W. Zeiger, K.S. Suslick, Chem Soc Rev, (2013) 2555–2567. https://doi.org/10.1039/c2cs35282f.

[100] N.R. Rightmire, T.P. Hanusa, Advances in organometallic synthesis with mechanochemical methods, 45 (2016) 2352–2362. https://doi.org/10.1039/c5dt03866a.

[101] D.A. Giannakoudakis, G. Chatel, J.C. Colmenares, Mechanochemical Forces as a Synthetic Tool for Zero- and One-Dimensional Titanium Oxide-Based Nano-photocatalysts, Top. Curr. Chem. 378 (2020) 2. https://doi.org/10.1007/s41061-019-0262-3.

[102] B. Jin, H. Bang, K.S. Suslick, Applications of Ultrasound to the Synthesis of Nanostructured Materials, Adv. Mater. 22 (2010) 1039–1059. https://doi.org/10.1002/adma.200904093.

[103] J.C. Yu, L. Zhang, J. Yu, Direct Sonochemical Preparation and Characterization of Highly Active Mesoporous TiO 2 with a Bicrystalline Framework, Chem. Mater. 14 (2002) 4647–4653.

[104] G. Cravotto, P. Cintas, Power ultrasound in organic synthesis : moving cavitational chemistry from academia to innovative and large-scale applications, Chem. Soc. Rev. 35 (2006) 180–196. https://doi.org/10.1039/b503848k.

[105] L.H. Thompson, L.K. Doraiswamy, Sonochemistry : Science and Engineering, Ind. Eng. Chem. Res. 38 (1999) 1215–1249.

[106] N. Ghows, M.H. Entezari, Ultrasound with low intensity assisted the synthesis of nanocrystalline TiO2 without calcination, Ultrason. Sonochem. 17 (2010) 878–883.

https://doi.org/10.1016/j.ultsonch.2010.03.010.

[107] P. Sathishkumar, R.V. Mangalaraja, S. Anandan, Review on the recent improvements in sonochemical and combined sonochemical oxidation processes - A powerful tool for destruction of environmental contaminants, Renew. Sustain. Energy Rev. 55 (2016) 426–454. https://doi.org/10.1016/j.rser.2015.10.139.

[108] C.G. Joseph, G. Li Puma, A. Bono, D. Krishnaiah, Sonophotocatalysis in advanced oxidation process: A short review, Ultrason. Sonochem. 16 (2009) 583–589. https://doi.org/10.1016/j.ultsonch.2009.02.002.

[109] D.A. Giannakoudakis, D. Łomot, J.C. Colmenares, When sonochemistry meets heterogeneous photocatalysis: designing a sonophotoreactor towards sustainable selective oxidation, Green Chem. 22 (2020) 4896–4905. https://doi.org/10.1039/d0gc00329h.

[110] G. Chatel, S. Valange, R. Behling, J.C. Colmenares, A Combined Approach using Sonochemistry and Photocatalysis: How to Apply Sonophotocatalysis for Biomass Conversion?, ChemCatChem. 9 (2017) 2615–2621. https://doi.org/10.1002/cctc.201700297.

[111] M. Hussein, A. Zuhairi, N. Fazliani, A comprehensive review on sonocatalytic , photocatalytic , and sonophotocatalytic processes for the degradation of antibiotics in water : Synergistic mechanism and degradation pathway, Chem. Eng. J. (2020) 127412. https://doi.org/10.1016/j.cej.2020.127412.

[112] S. Wang, Q. Gong, J. Liang, Sonophotocatalytic degradation of methyl orange by carbon nanotube/TiO2 in aqueous solutions, Ultrason. Sonochem. 16 (2009) 205–208. https://doi.org/10.1016/j.ultsonch.2008.08.002.

[113] R. Marotta, I. Di Somma, D. Spasiano, R. Andreozzi, V. Caprio, Selective oxidation of benzyl alcohol to benzaldehyde in water by TiO2/Cu(II)/UV solar system, Chem. Eng. J. 172 (2011) 243–249. https://doi.org/10.1016/j.cej.2011.05.097.

[114] C. Márquez-álvarez, G. Palmisano, L. Palmisano, F. Parrino, photocatalytic oxidation of aromatic alcohols to aldehydes in aqueous suspension of home prepared titanium dioxide 1.

Selectivity enhancement by aliphatic alcohols, Appl. Catal. A Gen. 349 (2008) 189–197.

[115] X. Lang, X. Chen, J. Zhao, Heterogeneous visible light photocatalysis for selective organic transformations, Chem. Soc. Rev. 43 (2014) 473–486. https://doi.org/10.1039/c3cs60188a.

[116] J. Kou, C. Lu, J. Wang, Y. Chen, Z. Xu, R.S. Varma, Selectivity Enhancement in Heterogeneous Photocatalytic Transformations, Chem. Rev. 117 (2017) 1445–1514. https://doi.org/10.1021/acs.chemrev.6b00396.

[117] B. Weng, M.Y. Qi, C. Han, Z.R. Tang, Y.J. Xu, Photocorrosion Inhibition of Semiconductor-Based Photocatalysts: Basic Principle, Current Development, and Future Perspective, ACS Catal. 9 (2019) 4642–4687. https://doi.org/10.1021/acscatal.9b00313.

[118] D.A. Giannakoudakis, A. Qayyum, D. Łomot, M.O. Besenhard, D. Lisovytskiy, T.J. Bandosz, J.C. Colmenares, Boosting the Photoactivity of Grafted Titania: Ultrasound-Driven Synthesis of a Multi-Phase Heterogeneous Nano-Architected Photocatalyst, Adv. Funct. Mater. 31 (2021) 1–7. https://doi.org/10.1002/adfm.202007115.

[119] M.I. Qadir, J.D. Scholten, J. Dupont, TiO2 nanomaterials: Highly active catalysts for the oxidation of hydrocarbons, J. Mol. Catal. A Chem. 383–384 (2014) 225–230. https://doi.org/10.1016/j.molcata.2013.12.012.

[120] R. Daghrir, P. Drogui, D. Robert, Modified TiO2 for environmental photocatalytic applications: A review, Ind. Eng. Chem. Res. 52 (2013) 3581–3599. https://doi.org/10.1021/ie303468t.

[121] X. Xiao, C. Zheng, M. Lu, L. Zhang, F. Liu, X. Zuo, J. Nan, Deficient Bi24O31Br10 as a highly efficient photocatalyst for selective oxidation of benzyl alcohol into benzaldehyde under blue LED irradiation, Appl. Catal. B Environ. 228 (2018) 142–151. https://doi.org/10.1016/j.apcatb.2018.01.076.

[122] D.A. Giannakoudakis, K. Vikrant, A.P. LaGrow, D. Lisovytskiy, K.H. Kim, T.J. Bandosz, J. Carlos Colmenares, Scrolled titanate nanosheet composites with reduced graphite oxide for photocatalytic and adsorptive removal of toxic vapors, Chem. Eng. J. 415 (2021) 128907. https://doi.org/10.1016/j.cej.2021.128907.

[123] A. Qayyum, D.A. Giannakoudakis, A.P. LaGrow, O. Bondarchuk, D. Łomot, J.C. Colmenares, High-frequency sonication for the synthesis of nanocluster-decorated titania nanorods: Making a better photocatalyst for the selective oxidation of monoaromatic alcohol, Catal. Commun. 163 (2022). https://doi.org/10.1016/j.catcom.2022.106406.

[124] C. Zheng, G. He, X. Xiao, M. Lu, H. Zhong, X. Zuo, J. Nan, Selective photocatalytic oxidation of benzyl alcohol into benzaldehyde with high selectivity and conversion ratio over Bi4O5Br2 nanoflakes under blue LED irradiation, Appl. Catal. B Environ. 205 (2017) 201–210. https://doi.org/10.1016/j.apcatb.2016.12.026.

[125] N. Luo, M. Wang, H. Li, J. Zhang, T. Hou, H. Chen, X. Zhang, J. Lu, F. Wang, Visible-Light-Driven Self-Hydrogen Transfer Hydrogenolysis of Lignin Models and Extracts into Phenolic Products, ACS Catal. 7 (2017) 4571–4580. https://doi.org/10.1021/acscatal.7b01043.

[126] A. Qayyum, D.A. Giannakoudakis, D. Łomot, R.F. Colmenares-Quintero, A.P. LaGrow, K. Nikiforow, D. Lisovytskiy, J.C. Colmenares, Tuning the physicochemical features of titanium oxide nanomaterials by ultrasound: Elevating photocatalytic selective partial oxidation of lignin-inspired aromatic alcohols, Ultrason. Sonochem. 94 (2023) 106306. https://doi.org/10.1016/j.ultsonch.2023.106306.

[127] A. Akbari-Fakhrabadi, P. Sathishkumar, K. Ramam, R. Palma, R. V. Mangalaraja, Low frequency ultrasound assisted synthesis of La0.6Sr0.4Co0.2Fe0.8O3-δ (LSCF) perovskite nanostructures, Powder Technol. 276 (2015) 200–203. https://doi.org/10.1016/j.powtec.2015.02.043.

[128] Z. Dong, A.P. Udepurkar, S. Kuhn, Synergistic effects of the alternating application of low and high frequency ultrasound for particle synthesis in microreactors, Ultrason. Sonochem. 60 (2020) 104800. https://doi.org/10.1016/j.ultsonch.2019.104800.

[129] T. Li, R. Tsyshevsky, M. McEntee, E.M. Durke, C. Karwacki, E.E. Rodriguez, M.M. Kuklja, Titania Nanomaterials for Sarin Decomposition: Understanding Fundamentals, ACS Appl. Nano Mater. 5 (2022) 6659–6670. https://doi.org/10.1021/acsanm.2c00693.

[130] D.E. Lee, D. Jin Kim, V. Devthade, W.K. Jo, S. Tonda, Size-dependent selectivity and activity of highly dispersed sub-nanometer Pt clusters integrated with P25 for CO2 photoreduction into methane fuel, Appl. Surf. Sci. 584 (2022) 152532. https://doi.org/10.1016/j.apsusc.2022.152532.

[131] A.K. Keshari, P. Choudhary, V.K. Shukla, Precursor induced evolution in single anatase phase synthesis of TiO2 nanoparticles for water treatment and dye-sensitized solar cell, Phys. B Condens. Matter. 631 (2022) 413716. https://doi.org/10.1016/j.physb.2022.413716.

[132] M. Thommes, K. Kaneko, A. V. Neimark, J.P. Olivier, F. Rodriguez-Reinoso, J. Rouquerol, K.S.W. Sing, Physisorption of gases, with special reference to the evaluation of surface area and pore size distribution (IUPAC Technical Report), Pure Appl. Chem. 87 (2015) 1051–1069. https://doi.org/10.1515/pac-2014-1117.

[133] Z. Wan, Z. Li, W. Yi, A. Zhang, G. Li, S. Wang, International Journal of Biological Macromolecules Lignin and spent bleaching clay into mono-aromatic hydrocarbons by a cascade dual catalytic pyrolysis system : Critical role of spent bleaching clay, Int. J. Biol. Macromol. 236 (2023) 123879. https://doi.org/10.1016/j.ijbiomac.2023.123879.

[134] B. Toubal, K. Elkourd, R. Bouab, O. Abdelaziz, The impact of copper–cerium (Cu–Ce) addition on anatase-TiO2 nanostructured films for its inactivation of Escherichia coli and Staphylococcus aureus, J. Sol-Gel Sci. Technol. 103 (2022) 549–564. https://doi.org/10.1007/s10971-022-05763-7.

[135] S. Sharieff, S. Veluturla, N. Kottam, S.P. Smrithi, R. Singhvi, Esterification of levulinic acid to butyl levulinate over TiO2/WO3/SO42−: optimization and kinetic study, Biomass Convers. Biorefinery. (2023) 1–15. https://doi.org/10.1007/s13399-023-04016-z.

[136] T.R. Giraldi, J.A. Dias, C.M. Baggio, S.C. Maestrelli, J.A. Oliveira, Anatase-to-rutile transition in co-doped TiO2 pigments, J. Sol-Gel Sci. Technol. 83 (2017) 115–123. https://doi.org/10.1007/s10971-017-4379-y.

[137] P. Makuła, M. Pacia, W. Macyk, How To Correctly Determine the Band Gap Energy of

Modified Semiconductor Photocatalysts Based on UV-Vis Spectra, J. Phys. Chem. Lett. 9 (2018) 6814–6817. https://doi.org/10.1021/acs.jpclett.8b02892.

[138] F. He, B. Zhu, B. Cheng, J. Yu, W. Ho, W. Macyk, 2D/2D/0D TiO2/C3N4/Ti3C2 MXene composite S-scheme photocatalyst with enhanced CO2 reduction activity, Appl. Catal. B Environ. 272 (2020) 119006. https://doi.org/10.1016/j.apcatb.2020.119006.

[139] M. Chi, X. Sun, G. Lozano-Blanco, B.J. Tatarchuk, XPS and FTIR investigations of the transient photocatalytic decomposition of surface carbon contaminants from anatase TiO2 in UHV starved water/oxygen environments, Appl. Surf. Sci. 570 (2021) 151147. https://doi.org/10.1016/j.apsusc.2021.151147.

[140] L. Wang, B. Cheng, L. Zhang, J. Yu, In situ Irradiated XPS Investigation on S-Scheme TiO2@ZnIn2S4 Photocatalyst for Efficient Photocatalytic CO2 Reduction, Small. 17 (2021). https://doi.org/10.1002/smll.202103447.

[141] B. Kim, T. Kang, G. Lee, H. Jeon, The effect of an annealing process on atomic layer deposited TiO2 thin films, Nanotechnology. 33 (2022). https://doi.org/10.1088/1361-6528/ac2f28.

[142] G. Karthikeyan Thirunavukkarasu, J. Bacova, O. Monfort, E. Dworniczek, E. Paluch, M. Bilal Hanif, S. Rauf, M. Motlochova, J. Capek, K. Hensel, G. Plesch, G. Chodaczek, T. Rousar, M. Motola, Critical comparison of aerogel TiO2 and P25 nanopowders: Cytotoxic properties, photocatalytic activity and photoinduced antimicrobial/antibiofilm performance, Appl. Surf. Sci. 579 (2022) 152145. https://doi.org/10.1016/j.apsusc.2021.152145.

[143] P.W. Koh, M.H.M. Hatta, S.T. Ong, L. Yuliati, S.L. Lee, Photocatalytic degradation of photosensitizing and non-photosensitizing dyes over chromium doped titania photocatalysts under visible light, J. Photochem. Photobiol. A Chem. 332 (2017) 215–223. https://doi.org/10.1016/j.jphotochem.2016.08.027.

[144] D. Zywitzki, H. Jing, H. Tüysüz, C.K. Chan, High surface area, amorphous titania with reactive Ti3+ through a photo-assisted synthesis method for photocatalytic H2 generation, J. Mater. Chem. A. 5 (2017) 10957–10967. https://doi.org/10.1039/c7ta01614j.

[145] J. Du, Q. Wu, S. Zhong, X. Gu, J. Liu, H. Guo, W. Zhang, H. Peng, J. Zou, Effect of hydroxyl groups on hydrophilic and photocatalytic activities of rare earth doped titanium dioxide thin films, J. Rare Earths. 33 (2015) 148–153. https://doi.org/10.1016/S1002-0721(14)60395-1.

[146] H. Kominami, K. Oki, M. Kohno, S.I. Onoue, Y. Kera, B. Ohtani, Novel solvothermal synthesis of niobium(v) oxide powders and their photocatalytic activity in aqueous suspensions, J. Mater. Chem. 11 (2001) 604–609. https://doi.org/10.1039/b008745i.

[147] Z. Zhang, P.A. Maggard, Investigation of photocatalytically-active hydrated forms of amorphous titania, TiO2·nH2O, J. Photochem. Photobiol. A Chem. 186 (2007) 8–13. https://doi.org/10.1016/j.jphotochem.2006.07.004.

[148] M. Elrouby, M.M. Khalaf, Synthesis and characterization of titania nanoparticles and enhancement of photochemical, photoelectrochemical and electrochemical performance with zirconia nanoparticles, J. Phys. Chem. Solids. 122 (2018) 227–233. https://doi.org/10.1016/j.jpcs.2018.06.034.

[149] G.N. Shao, S.M. Imran, S.J. Jeon, M. Engole, N. Abbas, M. Salman Haider, S.J. Kang, H.T. Kim, Sol-gel synthesis of photoactive zirconia-titania from metal salts and investigation of their photocatalytic properties in the photodegradation of methylene blue, Powder Technol. 258 (2014) 99–109. https://doi.org/10.1016/j.powtec.2014.03.024.

[150] A. Tang, Y. Deng, J. Jin, H. Yang, ZnFe2O4 -TiO2 nanoparticles within mesoporous MCM-41, Sci. World J. 2012 (2012) 1–8. https://doi.org/10.1100/2012/480527.

[151] M.J. Jackman, A.G. Thomas, C. Muryn, Photoelectron spectroscopy study of stoichiometric and reduced anatase TiO2(101) surfaces: The effect of subsurface defects on water adsorption at near-ambient pressures, J. Phys. Chem. C. 119 (2015) 13682–13690. https://doi.org/10.1021/acs.jpcc.5b02732.

[152] D.A. Giannakoudakis, N. Farahmand, D. Łomot, K. Sobczak, T.J. Bandosz, J.C. Colmenares, Ultrasound-activated TiO2/GO-based bifunctional photoreactive adsorbents for detoxification of chemical warfare agent surrogate vapors, Chem. Eng. J. 395 (2020).

https://doi.org/10.1016/j.cej.2020.125099.

[153] X. Ping, Y. Zhang, Q. Zhao, Y. Lu, L. Hao, Flexible TiO2 nanograss array film decorated with oxygen vacancies introduced by facile chemical reduction and their photocatalytic activity, Environ. Technol. Innov. 25 (2022) 102185. https://doi.org/10.1016/j.eti.2021.102185.

[154] M.H.M. Ahmed, R.H. Temperton, J.N. O'Shea, An in situ exploration of subsurface defect migration to a liquid water-exposed rutile TiO2(110) surface by XPS, Surf. Interface Anal. 53 (2021) 1013–1019. https://doi.org/10.1002/sia.6906.

[155] S. Ida, S.J. Samuel Justin, P. Wilson, B. Neppolian, Visible light active black TiO2 nanostructures and its RGO based nanocomposite for enhanced hydrogen generation and electrochemical potency, Appl. Surf. Sci. Adv. 7 (2022) 100215. https://doi.org/10.1016/j.apsadv.2022.100215.

[156] C.O. Ania, M. Seredych, E. Rodríguez-Castellón, T.J. Bandosz, Visible light driven photoelectrochemical water splitting on metal free nanoporous carbon promoted by chromophoric functional groups, Carbon N. Y. 79 (2014) 432–441. https://doi.org/10.1016/j.carbon.2014.08.001.

[157] M. Benmami, K. Chhor, A. V. Kanaev, Supported nanometric titanium oxide sols as a new efficient photocatalyst, J. Phys. Chem. B. 109 (2005) 19766–19771. https://doi.org/10.1021/jp051396+.

[158] Y. Li, T. Sasaki, Y. Shimizu, N. Koshizaki, Hexagonal-close-packed, hierarchical amorphous TiO2 nanocolumn arrays: Transferability, enhanced photocatalytic activity, and superamphiphilicity without UV irradiation, J. Am. Chem. Soc. 130 (2008) 14755–14762. https://doi.org/10.1021/ja805077q.

[159] A. Medvids, P. Onufrijevs, J. Kaupužs, R. Eglitis, J. Padgurskas, A. Zunda, H. Mimura, I. Skadins, S. Varnagiris, Anatase or rutile TiO2 nanolayer formation on Ti substrates by laser radiation: Mechanical, photocatalytic and antibacterial properties, Opt. Laser Technol. 138 (2021). https://doi.org/10.1016/j.optlastec.2020.106898.

[160] L. Xiang, X. Liu, C. Yang, Q. Lei, J. Zhao, X. Zhao, Ultrafast synthesis of anatase TiO2 microspheres doped with rare-earth by one-step microwave method, Inorg. Chem. Commun. 127 (2021) 108532. https://doi.org/10.1016/j.inoche.2021.108532.

[161] J. Zhang, P. Sun, P. Jiang, Z. Guo, W. Liu, Q. Lu, W. Cao, The formation mechanism of TiO2 polymorphs under hydrothermal conditions based on the structural evolution of [Ti(OH)h(H2O)6-h]4-h monomers, J. Mater. Chem. C. 7 (2019) 5764–5771. https://doi.org/10.1039/c9tc00662a.

[162] D.A. Giannakoudakis, N. Farahmand, D. Łomot, K. Sobczak, T.J. Bandosz, J.C. Colmenares, Ultrasound-activated TiO2/GO-based bifunctional photoreactive adsorbents for detoxification of chemical warfare agent surrogate vapors, Chem. Eng. J. 395 (2020) 125099. https://doi.org/10.1016/j.cej.2020.125099.

[163] D.A. Giannakoudakis, K. Vikrant, A.P. LaGrow, D. Lisovytskiy, K.-H. Kim, T.J. Bandosz, J. Carlos Colmenares, Scrolled titanate nanosheet composites with reduced graphite oxide for photocatalytic and adsorptive removal of toxic vapors, Chem. Eng. J. 415 (2021) 128907. https://doi.org/10.1016/j.cej.2021.128907.

[164] S.S. Abdullahi, S. Güner, Y. Koseoglu, I. Murtala, B.I. Adamu, M.I. Abdulhamid, Sımpl e Method For The Determ ınatıon o f Band Gap of a Nanopowdered Sample Usıng Kubelka Munk Theory, J. Niger. Assoc. Math. Phys. 35 (2016) 241–246.

[165] J.F. Guayaquil-Sosa, B. Serrano-Rosales, P.J. Valadés-Pelayo, H. de Lasa, Photocatalytic hydrogen production using mesoporous TiO2 doped with Pt, Appl. Catal. B Environ. 211 (2017) 337–348. https://doi.org/10.1016/j.apcatb.2017.04.029.

[166] Á. Kukovecz, K. Kordás, J. Kiss, Z. Kónya, Atomic scale characterization and surface chemistry of metal modified titanate nanotubes and nanowires, Surf. Sci. Rep. 71 (2016) 473–546. https://doi.org/10.1016/j.surfrep.2016.06.001.

[167] B.D. Yao, Y.F. Chan, X.Y. Zhang, W.F. Zhang, Z.Y. Yang, N. Wang, Formation mechanism of TiO 2 nanotubes, Appl. Phys. Lett. 82 (2003) 281–283. https://doi.org/10.1063/1.1537518.

[168] P. Qiu, B. Park, J. Choi, B. Thokchom, A.B. Pandit, J. Khim, A review on heterogeneous sonocatalyst for treatment of organic pollutants in aqueous phase based on catalytic mechanism, Ultrason. Sonochem. 45 (2018) 29–49. https://doi.org/10.1016/j.ultsonch.2018.03.003.

[169] D. Monga, S. Basu, Enhanced photocatalytic degradation of industrial dye by g-C 3 N 4 /TiO 2 nanocomposite: Role of shape of TiO 2, Adv. Powder Technol. 30 (2019) 1089–1098. https://doi.org/10.1016/j.apt.2019.03.004.

[170] N.R.C. Fernandes MacHado, V.S. Santana, Influence of thermal treatment on the structure and photocatalytic activity of TiO2 P25, Catal. Today. 107–108 (2005) 595–601. https://doi.org/10.1016/j.cattod.2005.07.022.

[171] T. Ohno, K. Sarukawa, K. Tokieda, M. Matsumura, Morphology of a TiO2 photocatalyst (Degussa, P-25) consisting of anatase and rutile crystalline phases, J. Catal. 203 (2001) 82–86. https://doi.org/10.1006/jcat.2001.3316.

[172] T. Billo, F.Y. Fu, P. Raghunath, I. Shown, W.F. Chen, H.T. Lien, T.H. Shen, J.F. Lee, T.S. Chan, K.Y. Huang, C.I. Wu, M.C. Lin, J.S. Hwang, C.H. Lee, L.C. Chen, K.H. Chen, Ni-Nanocluster Modified Black TiO2 with Dual Active Sites for Selective Photocatalytic CO2 Reduction, Small. 14 (2018) 1–11. https://doi.org/10.1002/smll.201702928.

[173] D.A. Giannakoudakis, A. Qayyum, V. Nair, A. Khan, S.R. Pradhan, J. Prekodravac, K. Rekos, A.P. LaGrow, O. Bondarchuk, D. Łomot, K.S. Triantafyllidis, J.C. Colmenares, Ultrasound-assisted decoration of CuOx nanoclusters on TiO2 nanoparticles for additives free photocatalytic hydrogen production and biomass valorization by selective oxidation, Mol. Catal. (2021). https://doi.org/10.1016/j.mcat.2021.111664.

[174] D.A. Giannakoudakis, A. Qayyum, M. Barczak, R.F. Colmenares-Quintero, P. Borowski, K. Triantafyllidis, J.C. Colmenares, Mechanistic and kinetic studies of benzyl alcohol photocatalytic oxidation by nanostructured titanium (hydro)oxides: Do we know the entire story?, Appl. Catal. B Environ. 320 (2023). https://doi.org/10.1016/j.apcatb.2022.121939.

[175] H. Liu, H. Li, J. Lu, S. Zeng, M. Wang, N. Luo, S. Xu, F. Wang, Photocatalytic Cleavage

of C-C Bond in Lignin Models under Visible Light on Mesoporous Graphitic Carbon Nitride through π-π Stacking Interaction, ACS Catal. 8 (2018) 4761–4771. https://doi.org/10.1021/acscatal.8b00022.

[176] Y. Ma, Z. Du, J. Liu, F. Xia, J. Xu, Selective oxidative C-C bond cleavage of a lignin model compound in the presence of acetic acid with a vanadium catalyst, Green Chem. 17 (2015) 4968–4973. https://doi.org/10.1039/c5gc00645g.

[177] F. V. de Andrade, R. Augusti, G.M. de Lima, Ultrasound for the remediation of contaminated waters with persistent organic pollutants: A short review, Ultrason. Sonochem. 78 (2021) 105719. https://doi.org/10.1016/j.ultsonch.2021.105719.

[178] S. Anandan, V. Kumar Ponnusamy, M. Ashokkumar, A review on hybrid techniques for the degradation of organic pollutants in aqueous environment, Ultrason. Sonochem. 67 (2020) 105130. https://doi.org/10.1016/j.ultsonch.2020.105130.

[179] S. Matsuzawa, J. Tanaka, S. Sato, T. Ibusuki, Photocatalytic oxidation of dibenzothiophenes in acetonitrile using TiO2: Effect of hydrogen peroxide and ultrasound irradiation, J. Photochem. Photobiol. A Chem. 149 (2002) 183–189. https://doi.org/10.1016/S1010-6030(02)00004-7.

[180] W. Deng, H. Zhang, X. Wu, R. Li, Q. Zhang, Y. Wang, Oxidative conversion of lignin and lignin model compounds catalyzed by CeO2-supported Pd nanoparticles, Green Chem. 17 (2015) 5009–5018. https://doi.org/10.1039/c5gc01473e.

[181] Y. Ma, Z. Du, F. Xia, J. Ma, J. Gao, J. Xu, Mechanistic studies on the VO(acac)2-catalyzed oxidative cleavage of lignin model compounds in acetic acid, RSC Adv. 6 (2016) 110229–110234. https://doi.org/10.1039/c6ra23486k.

[182] L. Zhao, S. Shi, G. Zhu, M. Liu, J. Gao, J. Xu, Au-Pd alloy cooperates with covalent triazine frameworks for the catalytic oxidative cleavage of β-O-4 linkages, Green Chem. 21 (2019) 6707–6716. https://doi.org/10.1039/c9gc03081f.

[183] L. Zhao, B. Zhang, X. Xiao, F.L. Gu, R.Q. Zhang, Roles of the active species involved in the photocatalytic oxidation of benzyl alcohol into benzaldehyde on TiO2 under UV light:

Experimental and DFT studies, J. Mol. Catal. A Chem. (2016). https://doi.org/10.1016/j.molcata.2016.03.012.

[184] S. Higashimoto, N. Suetsugu, M. Azuma, H. Ohue, Y. Sakata, Efficient and selective oxidation of benzylic alcohol by O2 into corresponding aldehydes on a TiO2 photocatalyst under visible light irradiation: Effect of phenyl-ring substitution on the photocatalytic activity, J. Catal. 274 (2010) 76–83. https://doi.org/10.1016/j.jcat.2010.06.006.

[185] D. Liang, J. Wu, C. Xie, J. Wen, Y. Lyu, Z. Sofer, J. Zheng, S. Wang, Efficiently and selectively photocatalytic cleavage of C[sbnd]C bond by C3N4 nanosheets: Defect-enhanced engineering and rational reaction route, Appl. Catal. B Environ. 317 (2022) 121690. https://doi.org/10.1016/j.apcatb.2022.121690.

[186] G. Han, T. Yan, W. Zhang, Y.C. Zhang, D.Y. Lee, Z. Cao, Y. Sun, Highly Selective Photocatalytic Valorization of Lignin Model Compounds Using Ultrathin Metal/CdS, ACS Catal. 9 (2019) 11341–11349. https://doi.org/10.1021/acscatal.9b02842.